SURFACE PLASMON RESONANCE STUDY OF THE PURPLE GOLD ($AuAl_2$) INTERMETALLIC, pH-RESPONSIVE FLUORESCENCE GOLD NANOPARTICLES, AND GOLD NANOSPHERE ASSEMBLY

Panupon Samaimongkol

Dissertation submitted to the faculty of the Virginia Polytechnic Institute and State University in partial fulfillment of the requirements for the degree of

Doctor of Philosophy
In
Physics

Hans D. Robinson, Chair
Giti Khodaparast
Chenggang Tao
Webster Santos

June 22, 2018
Blacksburg, Virginia

Keywords: Surface plasmons (SPs), Localized surface plasmon resonances (LSPRs), Kretschmann configuration, Surface plasmon-enhanced fluorescence (PEF) spectroscopy, Self-Assembly, Nanoparticles

SURFACE PLASMON RESONANCE STUDY OF THE PURPLE GOLD ($AuAl_2$) INTERMETALLIC, pH-RESPONSIVE FLUORESCENCE GOLD NANOPARTICLES, AND GOLD NANOSPHERE ASSEMBLY

Panupon Samaimongkol

ABSTRACT
(academic)

In this dissertation, I have verified that the striking purple color of the intermetallic compound $AuAl_2$, also known as purple gold, originates from surface plasmons (SPs). This contrasts to a previous assumption that this color is due to an interband absorption transition. The existence of SPs was demonstrated by launching them in thin $AuAl_2$ films in the Kretschmann configuration, which enables us to measure the SP dispersion relation. I observed that the SP energy in thin films of purple gold is around 2.1 eV, comparable to previous work on the dielectric function of this material. Furthermore, SP sensing using $AuAl_2$ also shows the ability to measure the change in the refractive index of standard sucrose solution. $AuAl_2$ in nanoparticle form is also discussed in terms of plasmonic applications, where Mie scattering theory predicts that the particle bears nearly uniform absorption over the entire visible spectrum with an order magnitude higher absorption than efficient light-absorbing carbonaceous particle also known a carbon black. The second topic of this dissertation focuses on plasmon enhanced fluorescence in gold nanoparticles (Au NPs). Here, I investigated the distance-dependent fluorescence emission of rhodamine green 110 fluorophores from Au NPs with tunable spacers. These spacers consist of polyelectrolyte multilayers (PEMs) consisting of poly(allylamine hydrochloride) and poly(styrene sulfonate) assembled at pH 8.4. The distance between Au NPs and fluorophores was varied by changing the ambient pH from 3 to 10

and back, which causes the swelling and deswelling of PEM spacer. Maximum fluorescence intensity with 4.0-fold enhancement was observed with 7-layer coated Au NPs at ambient pH 10 referenced to pH 3. The last topic of this dissertation examines a novel approach to assemble nanoparticles, in particular dimers of gold nanospheres (NSs). 16 nm and 60 nm diameter NSs were connected using photocleavable molecules as linkers. I showed that the orientation of the dimers can be controlled with the polarization of UV illumination that cleaves the linkers, making dipolar patches. This type of assembly provides a simple method with potential applications in multiple contexts, such as biomedicine and nanorobotics.

SURFACE PLASMON RESONANCE STUDY OF THE PURPLE GOLD ($AuAl_2$) INTERMETALLIC, pH-RESPONSIVE FLUORESCENCE GOLD NANOPARTICLES, AND GOLD NANOSPHERE ASSEMBLY

Panupon Samaimongkol

ABSTRACT
(general audience)

This dissertation covers three related topics. The first is an investigation of the optical properties of the unusually colored purple gold, which is a blend of gold and aluminum with the chemical formula is $AuAl_2$. This compound is interesting in that the origin of this color is different from most other metals. In the case of gold, for example, the metal gold is yellow color by absorbing the blue component from white light, leaving behind yellow color reflected light. The blue light is absorbed by electrons that change their state from a lower energy to a higher one. In purple gold, the color results from a different phenomenon known as "surface plasmons." Surface plasmons are waves consisting of many electrons that move back and forth near an interface between a metal and an electrical insulator. The energy of surface plasmons in purple gold is low and corresponds to the purple color in this compound. Recently, published theoretical work supports the possibility of surface plasmons in purple gold. In this dissertation, I experimentally verify the presence of surface plasmons in purple gold. To launch surface plasmons, light was reflected off of a purple gold film deposited on the hypotenuse of a prism with varying angles of incidence. Surface plasmons can be observed by the sudden dimming of reflected light. From this, I was able to extract the surface plasmon dispersion relation, which is the relation between the inverse of the wavelength and the energy of the surface plasmons. In addition, I computed the light absorption properties of purple

.

gold when it is used in a nanoparticle form. The computational result showed that small purple gold nanoparticles absorb light very well, which may be useful in photothermal cancer therapy and solar steam generation.

The second dissertation topic comprises a study of fluorescent molecules. These are compounds that reemit light with a different and redder color than the color of the light that illuminates them. In this experiment, green fluorescent molecules were placed near the surface of gold nanoparticles to observe how the brightness of the light emission is affected by the distance between the molecule and the metal. The underlying mechanism is based on localized surface plasmon resonances in gold nanoparticles. Localized surface plasmon resonances are waves consisting of many electrons that oscillate inside the particle, and they only occur when light at certain frequency illuminate the particle. On the resonance, the particle also exhibits the brighter light around the particle's surface but the dimmer light away from the particle's surface. The light enhancement from the particle can change the light emission of the fluorescent molecules. If the fluorescent molecules were placed in the range of localized surface plasmon resonances, the light emission is increased owing to the brighter light from the particle. However, if the fluorescent molecules were placed further away from the range of localized surface plasmon resonances, the light emission is decreased owing to the dimmer light from the particle. The distance between the surface of gold nanoparticle and the fluorescent molecules was varied by wrapping the gold particles with ultra-thin films of different plastic polymers before attaching fluorescent molecules to the surface of the films. These polymer films have the property that they swell and shrink when the acidity and basicity of the solution of gold particles changes, which allows me to vary the distance between the gold particles and fluorescent molecules. The results showed that the observed light gets dimmer when the solution is more acidic. On the other hand, the brighter light is noticed when the solution is more basic, and this observation is repeatable many times. Moreover, my work differs from other published works

in that the particles with the polymer films are more robust and stable than the other particles. This allows more design flexibility and suggests applications in biomedical or environmental research where the particles can be used to locally measure properties, such as acidity in confined spacers such as living cells. It may be possible to use this technique for tumor cells in our body or toxic pollutants in the air or water.

The last dissertation topic involves assembling nanoparticles to build them into larger structures. In this experiment, I fabricated particle dimers that consisted of two gold nanospheres of different sizes. They were attached together by using small molecules that are sensitive to ultraviolet (UV) light, where these molecules allow small gold nanospheres to be attached to large gold nanospheres only in those locations on the large nanospheres that have been illuminated with a sufficient amount of UV light. To achieve this alignment, UV light with a linear polarization (a specific electric field direction) was used to select the area on the large nanospheres where the UV light was particularly intense and therefore able to break the molecules, leaving positively charged surface patches on the spheres. This results in the electrostatic attraction between the positive patches on the large gold nanospheres and the negatively charged small gold nanospheres. With this method, I was able to make dimers of nanospheres in a preferred alignment by changing the polarization of UV light. The experimental results showed a good yield of dipolar patches, which allows multifunctional nanostructures with applications in nanomedicine, optical sensing, nanoelectronics, etc.

Acknowledgements

Having pursued my Ph.D. degree, I would like to thank the following people who contributed in different ways to my research and my study at Virginia Tech. First, I would like to express my deepest and sincere gratitude to my research advisor, Dr. Hans Robinson, for his invaluable guidance, constant encouragement, and excellent caring. He provides me with the great opportunity to conduct research not only in the field of physics but also in fields such as chemistry, chemical engineering, and electrical engineering. Such a variety of research in multidisciplinary fields has broadened my intellectual horizon and established a solid foundation in a broad range of science and technology disciplines. Whenever I had trouble with my research, Dr. Robinson promptly responded to my questions and inquires as well as helped me–with his vision, experiences, and expertise– learn how to tackle unforeseen circumstances.

I would like to extend my cordial thanks to all my reading committee members. First, I am thankful to Dr. Giti Khodaparast for the accommodation of her optical apparatus and a confocal microscope. Moreover, she always greets me whenever we meet and strike up a personal conversation which gives a beneficial insight that is applicable to my research. I also acknowledge my gratitude to Dr. Chenggang Tao for his excellent instructions in solid state physics. My background knowledge in condensed matter physics has substantially expanded, and I first learned the term “plasmons” in his class. I am also grateful to Dr. Webster Santos for his advice on organic chemistry as well as his time and effort as a member of my doctoral committee in spite of his large workloads and responsibility. My project on nanoparticle assembly would not have been possible if synthesized and commercial chemicals from his laboratory had not been so generously provided to us.

I also extended a special thanks to Dr. Richey Davis for his generosity in giving me access to his dynamic light scattering instrument and most importantly the many valuable discussion I have had with him. He granted me access to his facilities without hesitation with which this work would not have been possible. For the work on fluorescence spectroscopy, I would like to express my appreciation to Dr. Craig Tollin for allowing me to gain access to the Academy of Integrated Science lab. In regards to the FESEM spectroscopy, I thank Stephen McCartney from the Nanoscale Characterization and Fabrication Lab (NCFL) for his training and granting of 24 hour access. I also would be remiss if I did not thank Christopher Winkler who deserves credit for training me in transmission electron microscopy (TEM).

I am indebted to the postdoctoral scholar Brenden Magill, who taught me several laboratory techniques and explained every detail of the experiments to me. I am very grateful to Erich See, Kirby Myers, and Jeong-Ah Lee for providing a friendly and cooperative atmosphere as well as a good companion at work. I further thank my undergraduate students Carter Vanhuss, Garrett Smith, Ryan Pederson, David Hastman, and Nick Ekanger, who worked tirelessly with much enthusiasm when we encountered experimental difficulties. I also appreciate the collaboration from Ashley Gates from Chemistry department for synthesizing the photocleavable molecules, Mingjun Zhou from Chemistry department for providing thermoresponsive polymers, and Siwen Wang from Chemical engineering department for carrying out the long-time experiment on the water splitting reaction project over the course of a year. They made my time more enjoyable and supplied a significant contribution to my research.

I would like to acknowledge the financial support from the Development and Promotion of Science and Technology Talents Project (Royal Government of Thailand scholarship) for providing me the opportunity to study abroad for five years. I was honored to be supported by the Tipsword Graduate

Scholarship during my second year. I was also funded by the Department of Physics at Virginia Tech and by the Institute for Critical Technology and Applied Science (ICTAS).

In addition to research work, my wider experiences of language and culture would not be fulfilled if I did not have my best friend Eddie Ball. He taught me to learn a variety of new skills, such as skiing, rock climbing, blowing leaves, etc. I would also like to thank his willingness to proof read countless pages full of peculiar terms (e.g. surface plasmons) and sophisticated mathematics in my dissertation. I would like to thank Ball's and Severson's families for the smiles, laughter, and wonderful memories of time spent at the beach, at Thanksgiving dinner, and other occasions. They have changed and shaped my life for the better. Thank you for being my home away from home and my second family.

Lastly, I would also like to emphasize the significance of my family in Thailand who constantly supports me in all my pursuits. They have been pillars of guidance and love in my life though they live on the other side of the world. I wish to thank my dad for letting me study anything I want to learn. I am grateful to my mom for the encouragement and giving me guidance in moments of confusion. I want to express my gratitude to my older sister. She always prepares everything and makes the arrangement for me every time I visit my home country. Thank you to everyone again. I would not be where I am today without your help, guidance, and unwavering support.

Table of Contents

List of Figures

Chapter 1 Introduction

1.1 Motivation and Literature review

The search for better materials that exhibit the desired properties for novel applications has long been governing significant attention. For example, semiconductors have been used as small-sized transistors in microelectronic industry for a few decades. These tiny transistors enhance the capability of information processing at higher speeds, which in turn contribute to the development in other scientific fields that require a large-scale computation. Nevertheless, the technology in the microelectronic industry still confronts several inevitable challenges when the size of an electronic switch (e.g. a MOSFET or a CMOS gate) has been scaled down from micrometer to nanometer size. These daunting issues include an increase in power dissipation density, gate current leakage due to the quantum tunneling effect, and the short channel effect [1-3]. Though optical components can also be used for fast information processing, their bulky size is not compatible with a portable platform high integration densities. Thanks to rapid progress in material science, plasmonic materials offer a path to overcome the limitations in optical information processing. Due to the efficient subwavelength confinement of localized surface plasmons (LSPs) in plasmonic material, electronic miniaturization beyond the diffraction limit is possible [4-6]. In addition, the presence of LSPs can be applied for improving the sensitivity of detection in biosensors and chemical sensors. Due to a large enhancement of the local electromagnetic (EM) field associated with LSPs, small changes in the local environment (e.g. a change in the concentration of analyte molecules) bring about a significant change in optical properties in certain metal nanostructures with applications in rapid monitoring and analysis [7-10] by way of a number of techniques including surface-enhanced Raman spectroscopy (SERS), surface-enhanced infrared spectroscopy (SEIRA), and second harmonic generation (SHG) [11-15]. New materials that possesses LSPs are therefore of considerable interest because of their potential for such applications,

while potentially providing simpler fabrication, better tunability, and superior properties compared to conventional materials such as gold and silver. In that vein, one of the topic of this dissertation is the investigation of the plasmonic properties of the intermetallic compound $AuAl_2$, which currently is mainly used in the jewelry industry due to its intense purple color. In chapter 2, I explore the use of this material for plasmonic applications.

The locally enhanced optical field induced by SPs and LSPs does not only improve the sensitivity of such well-known techniques as SERS, but it also plays an important role in the recent advancement in fluorescence spectroscopy. Drexhage et al. investigated the radiative and nonradiative rates of the emission intensity of a fluorescent dye near metallic and dielectric interfaces in 1974 [16]. After this early result, the effect of a metal nanostructure on the emission dynamics of fluorophores has been widely studied from both theoretical and experimental perspectives, opening a new field of research known as *plasmon-enhanced fluorescence* (PEF). The coupling between a LSP and a fluorophore in its vicinity determines the overall fluorescence intensity that may be either quenched or enhanced depending on many parameters, such as the size and shape of a plasmonic nanostructure, the spacing between two species, and the spectral properties of a nanostructure and a fluorescent molecule [17-19]. Of all these parameters, two important factors play a central role in fluorescence emission intensity. The first factor is the spectral overlap between the spectra, i.e., an absorption and emission, of respectively the LSPs and the fluorophores. The second factor is the distance between the surface of the plasmonic (usually metallic) nanostructure and the fluorophore where the Purcell effect is responsible for the principle of PEF [20]. Though metallic nanostructures do not possess a cavity like a conventional resonator, it nonetheless provides an enormous local density of optical states (LDOS), thereby increasing the characteristic emission rate of a fluorophore in its vicinity [21]. PEF enhancement can also be accomplished using a coupling between fluorophores and LSPs supported by a periodical plasmonic nanostructure, such as nanohole [22-24], nanorod [25], nanograting [26, 27] and nanoparticle array [28]. Similarly, nonperiodical but extended metallic nanostructures are also employed to obtain increases in excitation rate and a quantum yield [29-31]. For

example, Weitz et al. showed several orders of magnitude enhancement in the fluorescence intensity of Eu^{3+} ion on a silver island substrate in 1983 [31]. Significant enhancement has also been observed from copper island [32] and silver fractal nanostructures [33]. In addition, upconversion nanoparticles (UCNPs)–particles that absorb multiple lower-energy photons and emit a higher-energy photon–can be coupled to a metallic nanostructure in order to enhance the efficiency of the fluorescence upconversions. Feng et al. established a system composed of UCNPs coupled to gold nanorods of varying aspect ratios, and demonstrated a 22.6-fold intensity enhancement [34].

The distance between a metal nanostructure and a fluorophore can be precisely controlled by using an AFM, a thiol layer, or a polyelectrolyte film as a spacer [35-37]. A common positively charged polycation is poly(allylamine hydrochloride) (PAH), while a common negatively charged polyanion is poly(styrene sulfonate) (PSS). Due to its abundance of primary amines, PAH can be used as class of stimulus responsive polymer that swells and shrinks up to several hundred percent when ambient pH is varied [38, 39]. For polyelectrolyte multilayer (PEM) films consisting of PAH and PSS, the change in film thickness results from the change in the degree of ionization in PAH as it is a weak electrolyte. This occurs when films are assembled at pH comparable to or higher than the pKa of PAH (8.8) [40, 41]. This results in film containing excess amines [42]. As ambient pH is increased, the amine groups lose their charges, repel counter ions and become hydrophobic, making the film shrink. As ambient pH is decreased, on the other hand, amine groups regain their charges and attract counter ions and water molecules, making the film swell [43, 44]. This property enables the film thickness to be tuned with pH, and it is repeatable for multiple cycles [45]. Other similar PEM films have also been observed to change in thickness under ambient pH variation [39, 45, 46]. Most of the literature reports on PEF fluorescence quenching and enhancement phenomena that make use of PEM films use them asfixed rather than tunable spacers [18, 47-51]. In these reports, additional film layers are deposited to increase the distance between metal and fluorophores [52, 53]. To date, only one paper examines plasmonic fluorescence enhancement using a tunable spacer. Yuan et al employed

poly(acryloyl hydrazide), as a pH-responsive polymer, as the spacer varying the distance between silver nanoparticles and Por^{4+} dyes in order to show an almost two-fold intensity enhancement as the ambient pH was changed [54]. In chapter 3 of this dissertation, I detail an experiment exploiting the swelling-deswelling behavior of PAH/PSS film to systematically vary the distance between gold nanospheres and a fluorophore, while the number of layers in PEM films is kept fixed.

Au nanoparticles (NPs), in particular spherical gold colloids have been extensively studied for a long time since they can be used in diverse and multidisciplinary research fields because of their optical properties. These depend upon the particle shape and size, the surrounding medium, and any inter-particle spacing [55-58]. The properties originate from LSPs profiles, the peak of which is in the visible region visible region and can be shifted when the properties on the surface of the Au NPs change [59, 60]. These characteristics make Au NPs excellent as a platform for biological sensors, chemical sensors, and other nanodevices [61-66]. The optical properties of Au NPs have been exploited for thousands of years; at least since the 8th century BC. The oldest known artifact that implement this is gold-plated Egyptian ivory where the purple staining in the ivory was achieved by Au NPs formed during the production process [67]. Another prominent example is the Roman Lycurgus Cup (4th century) as shown in Figure 1.1. The glass matrix of this vessel contains 20-50 nm-sized Au and Ag NPs, which make it appear red in transmitted light (or when illuminated from behind) and turn green in reflected light (or when illuminated from the front) [68, 69]. Other handicrafts include the Purple of Cassius teapot (ca. 17th century), ornamental cups, glasses, lustre plates (15th –16th century) etc. [70, 71].

Due to the unique color of Au NPs, their optical properties were first investigated by Michael Faraday. He accounted for the color of "a beautiful ruby fluid" (or Au colloids in the present terminology) as a result of "a mere variation in the size of particles" in the Bakerian lecture entitled "Experimental Relations of Gold (and Other Metals) to Light" [72]. His report paved the way for many scientists to conduct theoretical and experimental studies on the optical characteristics of nanoparticles made of gold and other metals [73-76].

There are numerous approaches, both *top-down* and *bottom-up* to fabricate Au NPs, which vary in particle shape, size, solubility, stability and functionality [77]. For example, Au nanospheres in a water suspension are commonly prepared by a citrate reduction method [78-80]. For Au nanorod synthesis, a seed-mediated growth method is usually used [81, 82]. Physical fabrication methods (e.g. thermolysis, sonochemistry, photochemistry etc.) have also been reported [83-85]. In this dissertation, chemical synthesis, which is in the class of "bottom-up" approach, has been used to synthesize spherical Au NPs suspended in water. This synthesis is based on the reduction of Au^{3+} ions to Au^{0} by reducing agents, where the Au NPs are made stable by capping or stabilizing agents that are adsorbed on the particle surface and repel each other, thereby preventing the particles from aggregating. A variety of reducing and stabilizing agents is available depending on the medium in which the particles are, and on the particle size. For example, citrate or ascorbate act as reducing and stabilizing agents in aqueous medium [86, 87], while glycol acts as a reducing and stabilizing agent in an organic medium [88].

Figure 1.1: The Lycurgus Cup, a 4th-century Roman drinking glass goblet which changes color under different illumination. This cup has a dull green background in normal lighting from the front, but appears ruby red under lighting originating from the back. The color changing effect stems from metal (Au and Ag) nanoparticles embedded inside the glass. The left image has been obtained by unknown from the Wikipedia website (https://en.wikipedia.org/wiki/Lycurgus_Cup#/media/File: Lycurgus_Cup_red_BM_MME1958.12-2.1.jpg). It was made available by Marie-Lan Nguyen which is licensed under a CC BY 2.5. It is attributed to "unknown". The right image has been obtained by Johnbod from the Wikipedia website (https://en.wikipedia.org/wiki/Lycurgus_Cup#/media/File:Green_Lycurgus_Cup.jpg). It was made available by Johnbod which is licensed under a CC BY-SA 3.0. It is attributed to "Johnbod".

The oldest and best-established method to fabricate Au nanosphere in an aqueous medium is the citrate reduction method due by Turkevich. It uses citrate ions acting as both reducing and stabilizing agents [79]. Au NPs obtained from this reaction have diameters between 10 and 50 nm, which can be controlled by the amount of citrate ions as shown by Frens. and are stable due to electrostatic repulsion of the negatively charged double layers created by citrate ions adsorbed on the Au NP surface [78]. Even after nearly seven decades, this method still remains heavily used because of the inexpensive reductant and non-toxic medium that are biocompatible and also compatible with many other applications. Au NPs with small diameters between 2-6 nm can be synthesized by the Brust method, but the medium is an organic solvent (toluene) which requires the phase-transfer technique if an aqueous medium is needed [89]. With other approaches, monodisperse and quasi-spherical Au NPs up to 200 nm in diameter can be fabricated by a kinetically controlled seeded growth strategy, which yields a narrow-sized distributions of Au NP in aqueous medium [87, 90].

Au NPs are not only used as individual units, but can also be combined into more complex ordered structures, such as nanocube-nanosphere dimers [91], heterodimers [92], and a core-satellite structure [93]. Such nanoparticle assembly has recently received a considerable amount of attention as the resulting nanostructures can be very helpful for a number of applications. For example, a plasmonic chiral sensor made of Au NPs dimers and oligomers can detect chiral molecules of antibiotics [94], heavy metals (e.g. Hg^{2+}, Ag^{+}) [95, 96], and DNA [97]. Other structures of this type of sensor include NP chains [98], NP helices [99], and NP pyramids [100]. A plasmonic fluorescence sensor in a form of a core-satellite structure was made from CdTe quantum dots and Au NP in order to enhance fluorescence intensity in proteins [101]. In addition to conventional colorimetric sensors using Au NPs colloids [102], a spectral blue shift of Au NPs dimers has also been used to probe DNA in serum [103]. A SERS sensor made of vertically aligned Au nanorods has been demonstrated for monitoring minute food contaminants at femtomolar concentrations [104].

Due to the great variety of complex ordered nanostructures useful in applications, numerous techniques and strategies have been employed to assemble NPs into larger structures. This dissertation focuses on a particular type of nanoassembly known as an "orientational assembly" where each building block is precisely arranged in a preferential direction in order to form a one- (1D) or two-(2D) dimensional nanostructure. The building blocks may be either isotropic (e.g. nanospheres) or anisotropic NPs (e.g. nanorods, nanostars, or nanocubes) where the interaction between NPs is designed such that a specific orientation of assembly is achieved. The interactions may depend on many factors, such as the shape of NPs, the capping layer coating the NPs, and the ligands used for binding the NPs together [105, 106]. Orientational alignment may be mediated by the shape anisotropy of the NPs themselves [91]. Even if the shape of a NP is isotropic, the assembly may be controlled by an anisotropic driving force, resulting in an aligned structure [107]. The interaction driving the assemble can have different origins, such as electrostatic attraction [107], entropic forces [108, 109], hydrogen bonds [110], and van der waals forces [111-113]. In addition to such intrinsic forces, efficient directional control on NP assembly can be achieved using external forces such as an applied electric field [114], surface-modified substrates [115], or bimolecular ligands [116]. For NPs assembly from biomolecules, Mirkin and Alivistatos were the first to harness DNA as a linker in order to organize Au NPs into a nanocrystal form in 1996 [102, 117]. As DNA is easily synthesized and controlled in terms of base sequences, it is often employed for other regiospecific structures such as Au-Ag dimers [118], Au NPs dimers [116, 119, 120], Au NPs trimers [121], Janus (two-faced) clusters [122], and alternating particle chains [98]. This work has also inspired other complex nanostructures to be built with other molecules such as poly(ethyleneglycol) [101], antibodies [123], and disulfide linkages [124].

In this dissertation, I use a photocleavable molecule as the linker between NPs. These are molecules that release an active functional group upon absorption of a photon. Many equivalent terms are used to describe such molecules, including photocleavable, photolabile, photoremovable, photoactivatable, photouncaging or photoreleasable [125]. These moieties were first introduced in 1966 [126, 127], and can be integrated

into larger ligands for a multitude of applications such as cell adhesion [128], sequential protein release [129], DNA sequencing [130], and NPs assembly [131, 132]. For the case of NPs assembly, the photoreleased product is usually a positively or negatively charged functional group that enables binding by electrostatic attraction. More specifically, such a photocleavable molecule comprises a photoremovable group, which reacts to light as an external stimulus, and ligand attached to a NP that presents the caged group upon irradiation. For example, nitrophenethyl and nitrobenzyl groups undergo a photouncaging reaction when irradiated with UV light [133-136], while a 4-α-amino acid and an *o*-nitrobenzyl methacrylate are chemically cleaved upon irradiation with visible light [125, 137]. Other derivatives have also been developed as photoactivable groups, including benzoin esters, cinnamyl esters, fluorenecarboxylates etc. [138, 139]. Note that photoclevable molecules undergo a bond cleavage only if enough energy is provided by the light. In chapter 4 of this dissertation, I describe an experiment where a photocleavable linker was used to form well-defined Au NPs dimers.

This nanostructure consists of two different Au nanospheres of two different diameters. The alignment of small Au NPs on large Au NPs is here controlled by the polarization of the incident UV light. A bond cleavage occurs preferentially in a certain area of the spheres, leaving positively charged amines under low pH condition. This allows negatively charged particles to assemble onto the desired areas, creating structures of a defined orientation as defined by the polarization direction. Such structures have potential applications in several fields, including pharmacology and optoelectronic devices.

1.2 Dissertation outline

This dissertation consists of this introductory chapter and three additional chapters, each relating a specific experiment as outlined below:

1.2.1 Chapter 2 Launching low energy surface plasmon resonances (SPRs) in the purple gold ($AuAl_2$) intermetallic

Chapter 2 demonstrates the existence of SPs in the $AuAl_2$ intermetallic compound. $AuAl_2$ is an oxidation-resistant material with an intense purple color. This color has long been thought to be due to an interband absorption transition, but its theoretical dielectric function predicts that SPs are responsible for the unusual color. This chapter describes an experiment that launches SPs in $AuAl_2$ thin film using the Kretschmann configuration, verifying the SP origin of the color. The SP dispersion relation was established experimentally from a careful experimental measurement and found to be in a good agreement with the theoretical dispersion relation. A SPR sensor based on $AuAl_2$ films was also investigated in order to further verify the existence of low energy SPPs in this material. Finally, the chapter ends with a discussion of the feasibility of employing $AuAl_2$ nanoparticles in particular applications.

1.2.2 Chapter 3 Tunable fluorescence intensity by pH-responsive polymer on Au nanocomposites

Chapter 3 places an emphasis on the role of LSPs on fluorescence phenomena, i.e., fluorescence quenching and enhancement. This chapter begins with a literature review of the study of what is known as *plasmon-enhanced fluorescence (PEF)*. It describes the mechanisms behind the quenching and enhancement of fluorophore luminescence intensity in terms of bright and dark plasmons. The chapter also outlines the concept of *plasmonic nanoantenna*, which provides a means of estimating the emission rate of the fluorophore such as a fluorescent molecule or a quantum dot in the presence of a metallic nanoparticle. An experiment is elaborated using the swelling-deswelling property of certain PAH/PSS films to tune the distance between gold nanospheres and a fluorophore by varying the ambient pH. The characterizations, such as extinction and fluorescence spectra, of a system composed of Au NPs and fluorophores are plotted

as a function of the ambient pH. Finally, this chapter draws a conclusion from the experiment and discusses the possibility of practical applications in biosensors and photonic devices.

1.2.3 Chapter 4 Optically aligned assembly of gold nanospheroids

Chapter 4 is dedicated to a novel approach to nanoparticle assembly. Gold nanoparticles are used as the building blocks for a fabrication of nanosphere dimers. The introduction of this chapter explores recent literature on self-assembly of different types of nanoparticles. Background on the chemistry of a photocleavable molecule, known as LIP3, used in this research is also provided. In addition, preliminary results of self-assembled monolayer (SAM) of LIP3 on gold film are presented. Our plan to combine larger and smaller gold nanoparticles into complex ordered aggregates is outlined. This chapter also reports experimental results obtained using field emission scanning electron (FESEM) microscopy. Finally, this chapter examines the possibility of controlling and binding different types of nanoparticles (e.g. gold and hematite nanoparticles) for an application in a water-splitting reaction.

1.3 Background: Plasmonics

Recent interest in surface plasmon polaritons (SPPs) and localized surface plasmons (LSPs) has led to the emergence of the new branch at the intersection of material science and optics known as *plasmonics*. Plasmonics is dedicated to fundamental phenomena and applications of optical phenomena associated with surface electromagnetic (EM) waves at the dielectric-metal interface in extended as well as in nanoscale systems. It is of considerable interest in nanoscience because of two striking characteristics of SPPs and LSPs, namely the localization and the enhancement of the EM field.

The first unusual feature of SPPs and LSPs is the ability to confine an EM wave to a volume of subwavelength width along a metal dielectric interface with applications to plasmonic waveguiding and transmission. Despite the dominance of electronic components based on semiconductors in integrated

circuits, information transmission is still limited by electrons that carry less data, travel slower, and create more heating than photons. Consequently, photonics–the area of study that harnesses light for application–offers photons as the information carrier to improve performance in information processing and transmission. Though photonic components feature superior rates of information transfer, the size of conventional photonic components (e.g. optical fibers) are bulky owing to the diffraction limit of light, which makes the size of the photonic devices at least one or two orders of magnitude larger than those of the electronic devices. This size mismatch between the electronic and photonic components impedes the capability of making smaller, faster, and more powerful devices. Because SPPs are strongly confined along a surface with lateral dimensions potentially much smaller than the wavelength of light, they can be employed in plasmonic waveguides, and by extension in plasmonic circuits, which then are good candidates to bridge the size-gap between nanoscale electronics and microscale photonics devices [140-146].

The second remarkable feature of SPPs and LSPs is the capability of providing a strong intensity enhancement of the plasmon EM field enhancement relative to the excitation field. In this context, regions with greatly enhanced EM fields are known as *hot spots*. This effect is particularly pronounced within a few nanometers of sharp corners or narrow gaps in metal nanostructures. Some examples of such structures include hemisphere dimers [147-149], nanocube dimers [150-152], nanostar [153-155] dimers, as well as larger aggregations of more than two particles [156]. Multiple hot spots are also observed on sharp corner structures and sharp tips [157, 158] including nanorods [159], nanoprisms [160, 161], and nanoflowers [162]. Hot spot generation can significantly increase the Raman signal in Raman spectroscopy–a technique for identifying molecules based on their mechanical vibrational modes. The near-field enhancement factor, defined as $g = (E_{local}/E_0)^2$ where E_0 is the amplitude of the electric field of the incident light, can be engineered, depending on the configuration of the nanostructure, to reach values of up to 10^7 [163], which has opened a new field known as *surface enhanced Raman spectroscopy (SERS)* [164-166].

Plasmonic hot spots are also instrumental in the area of plasmon-enhanced fluorescence (PEF) spectroscopy. By placing a fluorescent molecule in the vicinity of a metallic nanostructure, the highly

enhanced local EM field owing to LSPs can increase both the fluorescence excitation and the emission rate of the fluorophore. The fluorescence enhancement factor may increase about 2- to 200- fold for nanorods [167, 168], nanoholes [24, 169, 170] or core-shell nanoparticles [171-173]. A record 1300-fold enhancement was observed for a bowtie nanostructure and fluorophore with low intrinsic quantum efficiency [174]. This intensity enhancement provides higher signal-to-noise ratio in fluorescence imaging [34, 173, 175].

1.4 Terminologies

In this dissertation, certain common terms appear in several of the chapters. In this subsection, I provide the fundamental meaning and physical principles behind these terms. The details and derivation of interesting equations (e.g. a dispersion relation, a cross section, an efficiency etc.) will be elaborated in the relevant chapters.

1.4.1 The plasmon

A plasmon is a quantum mechanical quasiparticle resulting from the quantization of classical plasma oscillations. A plasma can be modeled as a gas of electrons overlapping a background of fixed positive ions such that the overall structure is charge neutral. Electrons are free to move in the structure, but any deviation from the equilibrium charge density is subject to a restoring force produced by the positive ions, which results in the possibility of plasma oscillations. Plasmons are bosonic particles and can be seen as a collective excitation of conduction electrons in a material, launched by the appropriate excitations such as particle impact or EM radiation. Nevertheless, the term *plasmon* is used to denote all kinds of conductive electron oscillations in a material and this can be categorized into three types depending upon the dimension of the conducting object. The three types are (1) volume or bulk plasmons, (2) surface plasmons, and (3) localized surface plasmons.

1.4.2 Volume or bulk plasmons

A volume or bulk plasmon, as suggested by the name, is a collective oscillation of electrons in a bulk material as shown in Figure 1.2. The simplest example of a bulk plasmon is a system of positive and negative ions of ionized gas in a discharge tube. In addition, plasmons are observed in metals because free electrons inside these materials behave similarly to a plasma under suitable excitation.

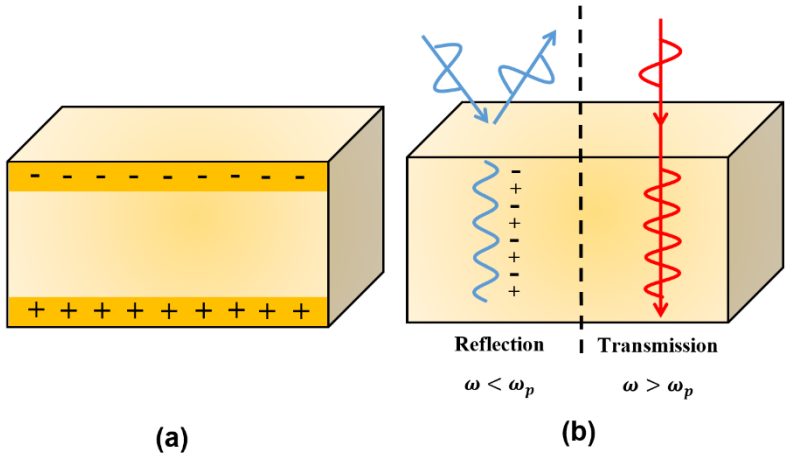

Figure 1.2: (a) Bulk or volume plasmons are coherent collective oscillations of free electrons at the plasma frequency ω_p given by Eq. (1.3.1) in bulk material. (b) If an incident electromagnetic (EM) wave (or light) with the frequency ω below the plasma frequency ω_p is incident upon the material, the majority of light is reflected and wave transmitted. In contrast, if the frequency ω of an incident EM is above the plasma frequency ω_p, light is transmitted through the material.

From the classical point of view, a bulk plasmon is an oscillation of conduction (or free) electrons back and forth relative to the positive fixed ions, which have heavier masses than electrons, at the frequency known as the *plasma frequency* ω_p:

$$\omega_p^2 = \frac{ne^2}{m_{eff}\epsilon_0}, \qquad (1.4.1)$$

in which n is the conduction electron density, e is the elementary charge, which equals 1.602×10^{-19} C, m_{eff} is the effective mass of an electron in the metal, and ϵ_0 is the permittivity of free space, which is approximately equal to 8.85×10^{-12} F m^{-1}. In bulk gold, the volume plasmon energy $\hbar\omega_p \approx 8.55$ eV [176]. Classical plasma oscillations were theoretically investigated by Langmuir in 1928 [177]. However, the term *bulk plasmons* was later introduced by Pines in 1964 [178] when he and his collaborator Bohm pioneered theoretical research on plasmas in the quantum regime [179-182]. The existence of bulk plasmons was later experimentally verified by electron energy loss spectroscopy in aluminum and magnesium thin foils [183].

1.4.3 Surface plasmons and surface plasmon polaritons

A surface plasmon (SP) is the collective oscillation of conduction electrons near an interface such as the interface between a metal and a dielectric, as shown in Figure 1.3. Because this type of plasmon travels along the surface of the material, it is also known as a *propagating surface plasmons (PSPs)*. There are several other ways to view the SP. From the perspective of electrodynamics, the SP is a particular case of a surface wave in the theory of ground-wave propagation along the Earth by Zenneck [184] and Sommerfeld [185]. From the perspective of optics, the SP is one of the modes of an interface. Finally, from the aspect of solid state physics, the SP is a collective oscillation of electrons or the quantization of plasma travelling near the surface of a metal [186].

Surface plasmon resonance (SPR) is a physical phenomenon that occurs when the in-plane wave vector of incident photons matches the wave vector of a SP at the frequency of the light, thereby exciting SPs that propagate along the interface.

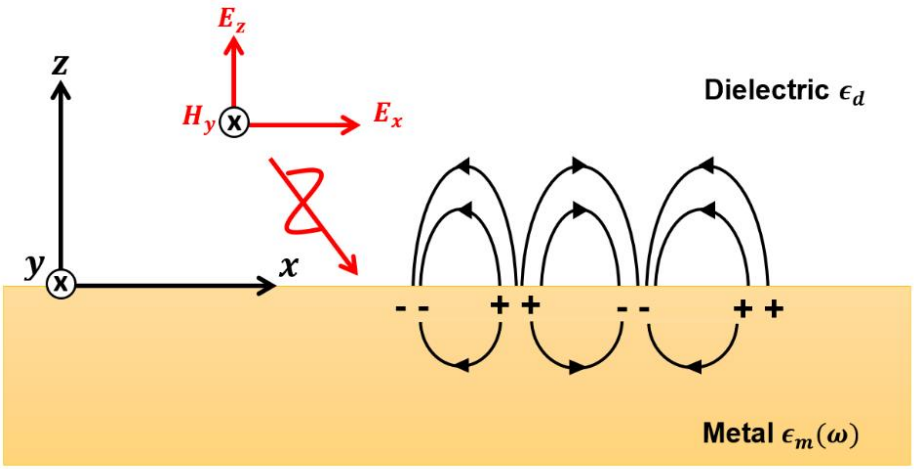

Figure 1.3: Surface plasmons (SPs) are coherent electron oscillations travelling along the interface between two media such as a metal and a dielectric.

Another term used interchangeably with SP in many publications is surface plasmon-polariton (SPP). The word polariton refers to a quasi-particle associated with the coupling between a photon and any other elementary excitation, such as a phonon, polaron, exciton etc. This term emphasizes that the plasmonic excitation includes a EM component as well as an electron component that together make up the SPP.

The term *surface plasmon* was originally introduced by Ritchie in 1957 as he theoretically explained SPs as the mechanism behind the energy loss of fast electrons passing through thin metal films [182]. In addition, the term *polariton* was first proposed by Hopfield in 1958 in order to describe the electromagnetic response of a medium using a quantum model [187, 188]. Finally, the term *surface plasmon polariton* was adopted when Elson and Ritchie exploited Hopfield's idea to explain a quantization of surface plasma waves [189].

In this dissertation, the term *SPPs* will be used for most propagating surface plasmon modes. Other terms and acronyms found in the literature for the same phenomenon include plasmon surface polariton (PSPs), surface plasma waves (SPWs), surface plasma oscillations (SPOs), and surface electromagnetic waves (SEWs) [190]. Many publications also use the short term *surface plasmons* instead of the longer *surface plasmon polaritons*.

1.4.4 Localized surface plasmon

A localized surface plasmon (LSP) is, again, the collective coherent oscillations of conduction electrons inside a nanostructure such as metallic nanospheres, nanotriangles, nanorods etc. As the size (or a diameter) of the nanoparticle is generally smaller than the wavelength of the incoming light, the free electrons inside the particle do not propagate along the surface. Instead they oscillate within the nanostructure due to the oscillatory electric field of the incident light as shown schematically in Figure 1.4. As the coherent electron oscillations usually happen in a nanoparticle, the LSP is also called a *particle plasmon* [191-194]. However, LSPs can exist locally within extended structured surfaces and constructs [195, 196]. Lastly, the term localized surface plasmon resonance (LSPR) is not different from LSP. The "R" simply emphasizes the resonant nature of this mode, which distinguishes it from a SPP. Such resonance can be observed as a peak in the extinction spectrum as shown in **Figure 1.10** and **Figure 1.11**.

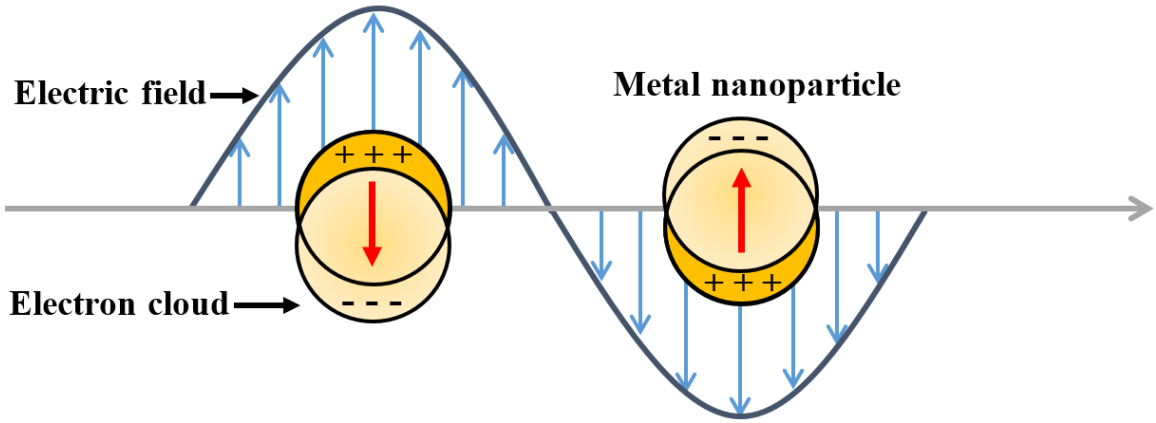

Figure 1.4: Schematic diagram representing a localized surface plasmon (LSP) inside a metal nanoparticle. The incident light travels to the right and induces (free) conduction electrons to oscillate, in phase with the incoming electric field. Such oscillations are widely distributed over the volume of a particle. Even if light is composed of an oscillating electric ***E*** and magnetic ***B*** fields perpendicular to each other, only the ***E*** fields (blue arrows) are shown because most materials are non-magnetic. Therefore, the effect of ***B*** field is negligible compared to that of ***E*** field which can exert a Coulomb force directly on the charged particles, in this case electrons.

1.5 Theory

1.5.1 Dispersion Relation of a surface plasmon polariton

In this section, we will focus on a SPP propagating along smooth interfaces or thin films. Note that this section provides a summary, while the full treatment will be laid out in Raether's book [203].

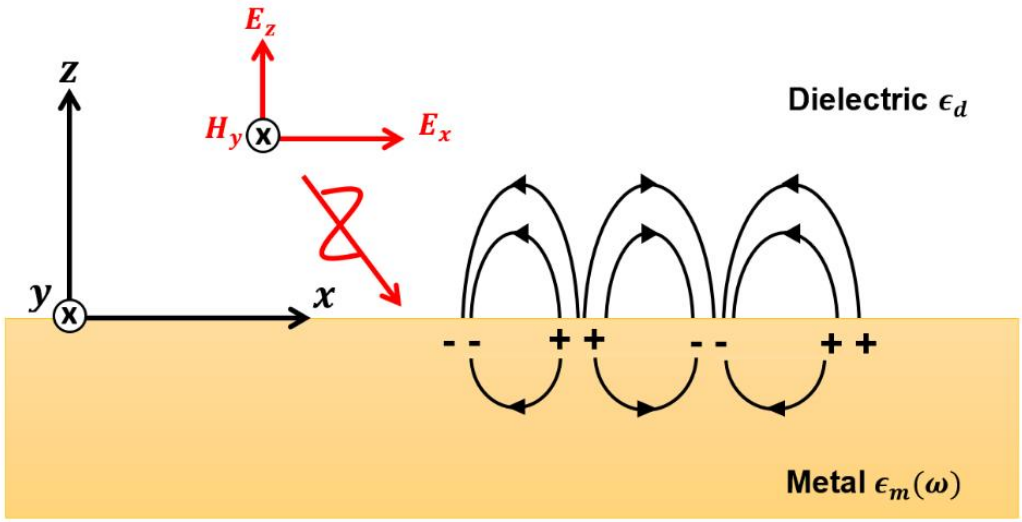

Figure 1.5: Schematic representation of a surface plasmon polariton (SPP) propagating in the x-direction on the interface ($z = 0$) between a metal with a complex dielectric function $\epsilon_m(\omega)$ and a dielectric with a real positive dielectric constant ϵ_d. Since a SPP is a p-polarized EM wave, in each medium, the y-component of the $\boldsymbol{E}$ field vanishes, and the x- and z- components of the $\boldsymbol{H}$ field are zero.

Consider a SPP propagating on a planar interface between two materials in the x-direction as indicated in Figure 1.5. Since a SPP usually exists on a metal-dielectric interface, we assume that the dielectric material has an isotropic, *positive*, *real* dielectric constant ϵ_d in the upper half-space $z > 0$, while the metal surface has an isotropic frequency-dependent, *complex* dielectric function $\epsilon_m(\omega) = \epsilon_{mR} + i\,\epsilon_{mI}$ in the lower half-space $z < 0$.

1.5.1.1 The solutions to Maxwell's equations *E* and *H* fields

A SPP can be represented by the electric field $\boldsymbol{E}$ and magnetic field $\boldsymbol{H}$ in each medium. This can be obtained from the solution of Maxwell's equations with the appropriated boundary conditions (BCs). The solutions for a p-polarized EM wave at frequency ω are as follows:

In the dielectric ($z > 0$)

$$\boldsymbol{E}_d = (E_{xd}, 0, E_{zd}) \exp i(k_x x + k_{zd} z - \omega t) ,$$
$$\boldsymbol{H}_d = \big(0, H_{yd}, 0\big) \exp i(k_x x + k_{zd} z - \omega t) . \tag{1.5.2}$$

In the metal ($z < 0$)

$$\boldsymbol{E}_m = (E_{xm}, 0, E_{zm}) \exp i(k_x x - k_{zm} z - \omega t) ,$$
$$\boldsymbol{H}_m = \big(0, H_{ym}, 0\big) \exp i(k_x x - k_{zm} z - \omega t) . \tag{1.5.3}$$

The propagation vector $\boldsymbol{k}$ in each medium depends on the frequency ω and the dielectric functions $\epsilon_m(\omega)$ and $\omega_d(\omega)$ via

$$k_{SPP}(\omega) = k_x = \frac{\omega}{c} \sqrt{\frac{\epsilon_m \epsilon_d}{\epsilon_m + \epsilon_d}}, \tag{1.5.4}$$

$$k_{zd(m)} = \frac{\omega}{c} \sqrt{\frac{\epsilon_{d(m)}}{\epsilon_m + \epsilon_d}}, \tag{1.5.5}$$

where c is the speed of light in vacuum.

A SP dispersion relation $\omega(k)$ may be recast as energy E and the wave vector k by using the fact that $E = \hbar\omega$. Therefore, (1.5.5) can be rewritten as

$$E = \hbar c k_{SPP} \sqrt{\frac{\epsilon_m + \epsilon_d}{\epsilon_m \epsilon_d}}. \qquad (1.5.6)$$

The SP dispersion relations of Au and $AuAl_2$ in air calculated from (1.5.6) are shown in Figure 1.6.

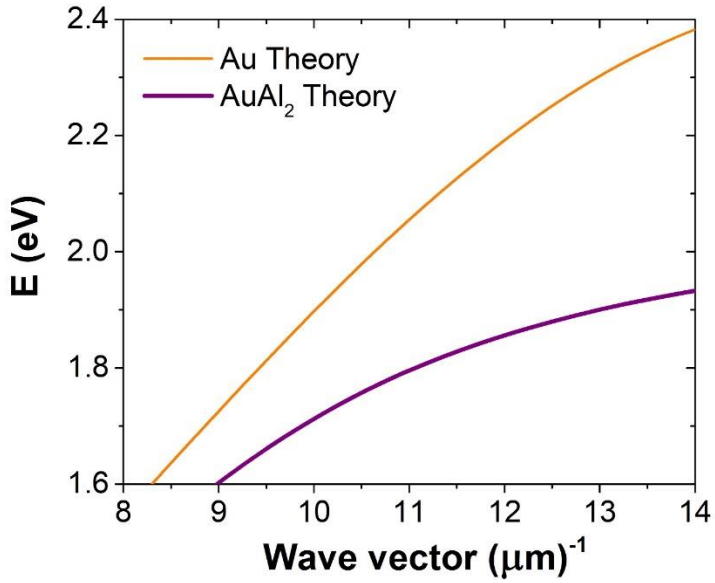

Figure 1.6: The theoretical dispersion relations $E(k)$ of SPPs on Au and $AuAl_2$ calculated from (1.5.6). The experimental dielectric function of Au is from Johnson and Christy [197], while that of $AuAl_2$ is from Supansomboon [198]. The adjacent dielectric is air.

1.5.1.2 Discussion on the existence of a SPP

If a SPP exists and travels along the x-direction but not in the z-direction, i.e., it is bound to the interface, two conditions must be met:

1.k_{zd} and k_{zm} must be imaginary because the amplitudes of the $\boldsymbol{E}$ and $\boldsymbol{H}$ fields decay exponentially with the distance z from the interface, i.e., $Re(k_{zd}) = 0$ and $Re(k_{zm}) = 0$.

2.k_{SPP} must be real and positive, i.e., $Re(k_x) > 0$. Thus, from (1.5.4) and (1.5.5), one has

$$\epsilon_m(\omega) \cdot \epsilon_d < 0\,, \qquad (1.5.7)$$

and

$$\epsilon_m(\omega) + \epsilon_d < 0\,. \qquad (1.5.8)$$

To meet these requirements, one possibility is that (i) ϵ_d is frequency-independent positive real and (ii) $\epsilon_m(\omega) = \epsilon_{mR} + i\,\epsilon_{mI}$ is frequency-dependent and complex where $\epsilon_{mR} < 0$ and $\epsilon_{mR} > \epsilon_d$; that is, the real part of $\epsilon_m(\omega)$ must be negative enough such that $\epsilon_m(\omega) + \epsilon_d < 0$. These condition can be satisfied in a large number of metals and other conductors at frequencies in the UV, visible, or near infrared.

1.5.1.3 Excitation of a surface plasmon polariton

We have already seen there are several ways to launch surface plasmons. One of them is to employ electron-energy-loss-spectroscopy (EELS), which uses fast electrons to excite 2D surface plasmons in certain materials (e.g. doped graphene) [199-201]. The other conventional way is optical excitation, which harness light or an electromagnetic wave to launch surface plasmons, and it will be the principal method used here. To launch SPPs by optical excitation, a phase matching condition must be fulfilled, which has three requirements:

1.The frequency ω of the incoming EM wave must be the same as that of the SPP, i.e., $\omega_{EM,in} = \omega_{SPP}$.

2.The component of the wave vector $\boldsymbol{k}$ of the incoming EM wave that is parallel to the propagation direction of the SPP must be the same as that of the SPP, i.e., $k_{||\,EM,in} = k_{SPP}$ or $k_{x\,EM,in} = k_x$.

3.The polarization of the incoming EM wave must be the same as that of the SPP, i.e., p-polarization.

In quantum mechanics terminology, the first requirement is the so-called *energy matching* because $E = \hbar\omega$, while the second is known as *momentum matching* because $p = \hbar k$.

In other words, phase matching occurs when two dispersion relations (of the incoming EM wave and the SPP) intersect. At the intersection point, all conditions above can be satisfied causing energy transfer between the incoming EM wave and the SPPs.

In practice, the first and third requirements are easily fulfilled, while the second is not accomplished by a simple setup. To illustrate this, consider the optical excitation of a SPP on a planar surface (e.g. a metal film in air). The p-polarized light is incident on the surface from the adjacent dielectric medium (e.g. air or vacuum) which is next to the metal film.

The dispersion relation $\omega(k)$ for the incoming EM wave is simply given by

$$\omega = ck\,, \tag{1.5.9}$$

while the dispersion relation of the SPP can be rewritten from (1.5.6) as

$$\omega_{SPP} = ck_{SPP}\sqrt{\frac{\epsilon_m + \epsilon_d}{\epsilon_m \epsilon_d}}. \tag{1.5.10}$$

These two expressions (1.5.9) and (1.5.10) can be plotted as the red line and the black curve depicted in Figure 1.7. Since $Re\left(\sqrt{\frac{\epsilon_m+\epsilon_d}{\epsilon_m\epsilon_d}}\right) < 1$, these two lines do not intersect at any frequency above $\omega = 0$ nor can the in-plane component of the light wave vector $k_x \leq k$, ever satisfy the momentum-matching condition. In other words, SPPs cannot be excited by simply shining light on a metal. This is a direct consequence of the SPPs confinements to the interface, which requires an imaginary k_{zd}, precluding any propagation in the z-direction.

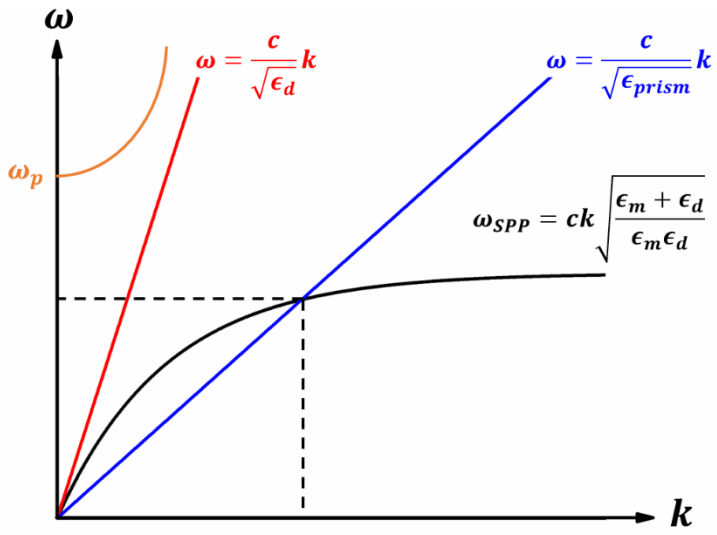

Figure 1.7: Excitation of SPPs on a metal film-air interface. The solid black curve represents the SPP dispersion relation on a metal (1.5.10). The solid red line is the light line in vacuum (1.5.9), which does not intersect the SPP dispersion relation at any point except the origin. In other words, SPP cannot be excited by the light line in free space. However, if light line is excited in a dielectric (e.g. a prism in the next section) as represented by the solid blue line, the light dispersion relation changes and can intersect the black curve, causing SPRs in a metal film. The orange line represents leaky surface modes given by $\omega = \sqrt{\omega_p^2 + c^2k^2}$.

1.5.1.4 Reflectivity minimum in the Kretschmann configuration

There are several experimental configurations that provide the wave vector matching needed for optical excitation of SPPs. For example, one can use diffraction of surface waves on a grating or on surface features [202-204]. The effective magnitude of the in-plane component of the incident light wave vector is then increased by adding the grating's reciprocal lattice vector to that of the light's wave vector such that momentum matching occurs. Another important technique is to use photon tunneling under total internal reflection (TIR). Two versions of this are usually discussed: (i) the Kretschmann [205] and (ii) the Otto [206] configurations.

In this dissertation, the Kretschmann configuration is adopted because of the convenient practical setup where a metal film is deposited onto a dielectric prism made from high-refractive index glass as depicted in the inset of Figure 1.8.The prism is illuminated as shown in the inset so that an angle of incidence on the

hypothenuse θ_i greater than the critical angle θ_c can be obtained. The reflection of the wave off the metal creates an evanescent field that penetrates into the metal film. If the phase matching condition illustrated in Figure 1.7 is satisfied, the evanescent field can excite a SPP on the outer surface of the metal film. When the excitation of a SPPs occurs, a minimum in the reflectivity vs. angle of incidence curve is observed. Note that the thickness of the metal film has an impact on the angle θ_{min} at which the reflectivity is minimum and on the launching of the SPRs because the thicker the film is, the harder it is to launch SPPs as the evanescent SPP wave decays exponentially before it reaches the other side of the Au film so that for sufficiently thick films, the excitation of the SPPs vanishes [207].

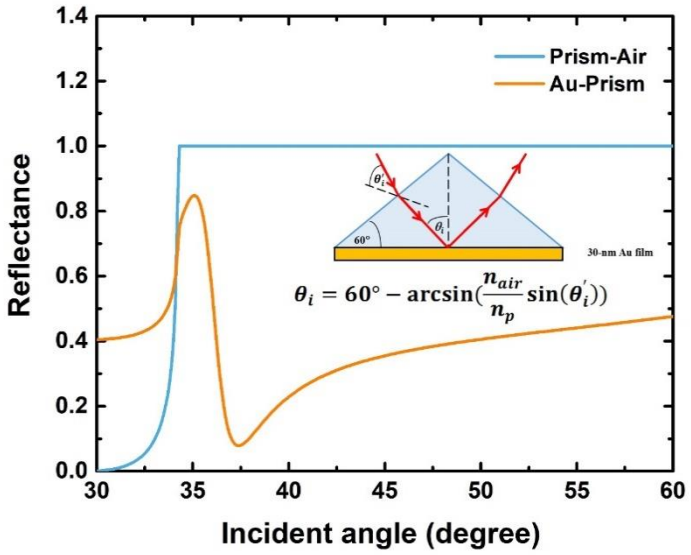

Figure 1.8: Theoretical reflectivity R of the excitation EM wave plotted as a function of the incident angle θ_i in the Kretschmann configuration for prism-air (blue curve) and Au-air (orange curve) interfaces. The inset shows the Kretschmann configuration which contains a prism with a 30-nm thick Au film coated on one side. Light at wavelength $\lambda = 632.8$ nm is incident from air to the prism and then to the Au film and then reflected back through the prism and air where the detector is located. The SPP excitation happens at the Au-air interface when the incident angle $\theta_i = \theta_{res} = 37.4°$, which is in the total internal reflection regime ($\theta_i > \theta_c = 34.2°$ for glass with $n = 1.78$).

Figure 1.8 shows the theoretical reflection curve for the case of a 30-nm Au film deposited on an equilateral prism made of N-SF11 glass, the refractive index of which at wavelength $\lambda = 632.8$ nm is $n_p = 1.7786 +$

$i(3.8639 \times 10^{-8}) \cong 1.7786$ (because the imaginary part of the refractive index –the extinction coefficient– is much smaller than the real part). The critical angle θ_c is given by $\theta_c = \arcsin\left(\frac{n_{air}}{n_p}\right)$, and equals 34.2°.

The orange curve is the reflectivity at the Au-prism interface. The minimum reflectivity R_{min} is observed at an incident angle $\theta_{res} = 37.4°$, which is the angle at which SPRs occurs and SPPs are launched. From Figure 1.7, the SPPs excitation takes place at an angle greater than the critical angle ($\theta_{res} > \theta_c$). At the resonance angle, the wave vector $k_{||\,EM}$ in a prism matches the SPP wave vector k_{SPP} in (1.5.4). From the inset of Figure 1.8, the wave vector in a prism k_p with refractive index n_p is given by $k_p = 2\pi\lambda_p = 2\pi/(\lambda/n_p) = 2\pi n_p/\lambda$ where λ is the wavelength of light in vacuum or air. Moreover, the component of a wave vector in the prism that is parallel to the surface is $k_p \sin\theta$. Thus, at the resonance angle $\theta_i = \theta_{res}$, $k_{||\,EM} = k_p \sin\theta_{min}$ or

$$k_{||,EM} = \frac{\omega}{c} n_p \sin\theta_{res}\,. \qquad (1.5.11)$$

The calculation of the reflectance R shown in Figure 1.8 was obtained from the *characteristic transfer matrix (CTM)* method, the details of which are elaborated in appendix A.

There are two interpretations that are true simultaneously that account for why there is minimum in the reflectance when SPPs are excited. The first interpretation is that the dip in reflectance results from the conversion of light to SPPs that carry energy away along the interface, so that it never reaches the detector [203, 207-210]. The second interpretation explains the reflectivity minimum as a result of the destructive interference between (i) light emitted from the SPP due to radiation damping and (ii) total internal reflection of the incident light [211-215].

1.5.2 Localized surface plasmon resonances (LSPRs)

For the case of a sufficiently small metallic nanoparticle (MNP), the electromagnetic excitation of a plasmon differs from that in the bulk (or volume) and on the surface of a thin film because the size of a particle d is comparable to the metal skin depth and usually much smaller than the incident wavelength λ, i.e. $d \ll \lambda$. Accordingly, an electric field associated with an incoming light can penetrate inside the particle and induce the net charge difference at the particle boundaries. Although the $\boldsymbol{E}$ field oscillates over time for small ($d \ll \lambda$) particles, it can be considered to be static at any instant. This treatment is known as the *quasi-static approximation*. In this case, all free conduction electrons inside the particle move under the influence of an electric field according to Coulomb's law with respect to the positive ion cores, which are much heavier and can be taken to be immobile. The net displacement of the negatively charged electrons with respect to the positively charged ions generates the restoring force pulling electrons back toward equilibrium, thereby causing a coherent oscillation of the conduction electrons at the resonance frequency of the particle, as shown in Figure 1.4. The wavelength at which the maximum extinction occurs, denoted, in this dissertation, by λ_{LSPR}, depends on the size, shape, surface chemistry, agglomeration state of the particle, etc. [55-58]. In LSPs, the electrons do not propagate along the surface, but locally oscillate inside the particle. This kind of plasmon is called a *localized surface plasmons* (LSPs) or a *localized surface plasmon resonances* (LSPRs) [19, 216-218]. This is because the restoring force leads to harmonic oscillation that can be excited through resonant coupling to an incident EM wave [219].

1.5.2.1 Mathematical formulation for a spherical nanoparticle: Mie scattering theory

To describe the interaction between light and a particle quantitatively, one needs to solve Maxwell's equations with appropriate boundary conditions. Those solutions, i.e. $\boldsymbol{E}$ and $\boldsymbol{H}$ fields in every region of the incident, scattered and internal fields, allow the calculation of extinction, scattering and absorption cross sections σ. The analytical solution to Maxwell's equations for a spherical particle was achieved and first

given by Gustav Mie in 1908 [73], which led to the main formulation of the so-called *Mie scattering theory*. It is also referred to *Lorenz-Mie theory* or *Lorenz-Mie-Debye theory*. See Bohren and Huffman [220] for a complete exposition of this theory.

Consider a spherical nanoparticle with radius a, of which the complex permittivity is ϵ_p, the magnetic permeability is μ_p, and the complex refractive index is n_p or $n_p^2 = \epsilon_p \mu_p$. It is embedded in a linear, homogeneous and isotropic ambient medium, whose real permittivity is ϵ_m, magnetic permeability is μ_m, and the real refractive index is n_m or $n_m^2 = \epsilon_m \mu_m$. This particle is illuminated by light of wavelength $\lambda_m = \lambda_0 / n_m$ and wave vector $k_m = 2\pi/\lambda_m$ where λ_0 is the wavelength of light in a vacuum or air as shown in Figure 1.9.

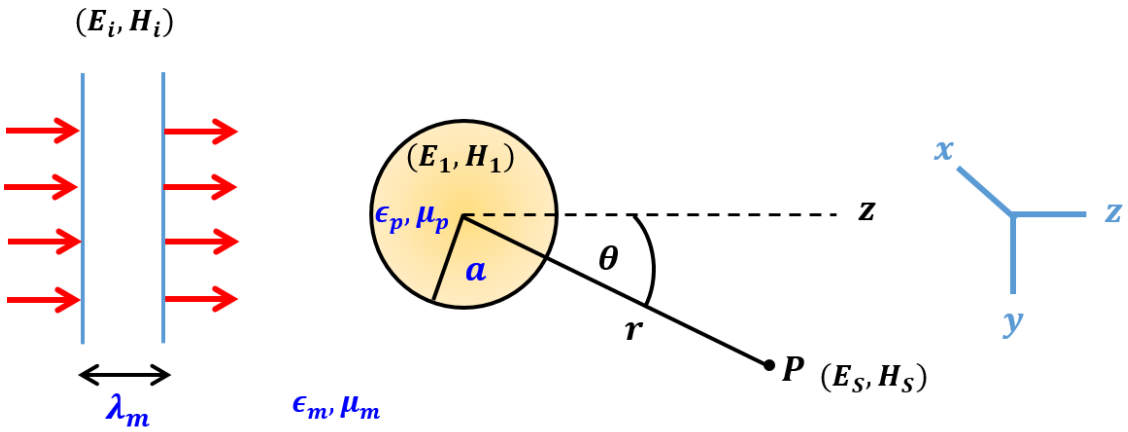

Figure 1.9: Schematic diagram for Mie scattering theory. A plane x-polarized electromagnetic wave with incident fields $(\boldsymbol{E_i}, \boldsymbol{H_i})$ in the surrounding medium is impinging upon a spherical particle of radius a. The internal fields $(\boldsymbol{E_1}, \boldsymbol{H_1})$ inside the sphere and the scattered fields $(\boldsymbol{E_s}, \boldsymbol{H_s})$ after the reradiation can be achieved by solving the wave equations derived from Maxwell's equations with the appropriate boundary conditions.

In this situation, the extinction σ_{ext}, scattering σ_{sca} and absorption σ_{abs} cross sections are given respectively by:

$$\sigma_{ext} = \pi a^2 \frac{2}{x^2} \sum_{l=1}^{\infty} (2l+1) Re(a_l + b_l) \cong \pi a^2 \frac{2}{x^2} \sum_{l=1}^{N_{max}} (2l+1) Re(a_l + b_l)\,,$$

$$\sigma_{sca} = \pi a^2 \frac{2}{x^2} \sum_{l=1}^{\infty} (2l+1)(|a_l|^2 + |b_l|^2) \cong \pi a^2 \frac{2}{x^2} \sum_{l=1}^{N_{max}} (2l+1)(|a_l|^2 + |b_l|^2)\,, \qquad (1.5.12)$$

$$\sigma_{abs} = \sigma_{ext} - \sigma_{sca},$$

where the coefficients[1] a_l and b_l, also known as *Mie coefficients* for the scattered fields, are

$$a_l = \frac{m^2 j_l(mx)[x j_l(x)]' - \mu j_n(x)[mx j_l(mx)]'}{m^2 j_l(mx)\left[x h_l^{(1)}(x)\right]' - \mu h_l^{(1)}(x)[mx j_l(mx)]'},$$

$$b_l = \frac{\mu j_l(mx)[x j_l(x)]' - j_n(x)[mx j_l(mx)]'}{\mu j_l(mx)\left[x h_l^{(1)}(x)\right]' - h_l^{(1)}(x)[mx j_l(mx)]'}, \qquad (1.5.13)$$

where $m = n_p/n_m$, $\mu = \mu_p/\mu_m$, and the size parameter $x = k_m a$. The functions $j_l(z)$, $h_l^{(1)}(z)$ where $z = x$ or mx are the l-th order spherical Bessel and Hankel functions of the first kind, respectively.

The cross sections in (1.5.12) are theoretically obtained by summing an infinite series of the coefficients a_l and b_l. This series comprises the sum of different order modes where $l = 1$ corresponds to the dipolar mode, $l = 2$ the quadrupolar mode, $l = 3$ the octupolar mode etc. In practice, the sum can be truncated after some $l = N_{max}$. In this dissertation, I use the value proposed by Bohren and Huffman where $N_{max} = x + 4x^{1/3} + 2$.

[1] The index l instead of n is employed to avoid confusion of using n which, in this case, refers to the (complex) refractive index.

Mie theory is also applicable for the quasi-static approximation. This special case is also known as *Rayleigh theory* where (1.5.12) reduces to

$$\sigma_{ext} = \sigma_{sca} + \sigma_{abs} ,$$

$$\sigma_{sca} = \frac{3}{2} k_m^4 V^2 \left| \frac{\epsilon_p - \epsilon_m}{\epsilon_p + 2\epsilon_m} \right|^2 , \tag{1.5.14}$$

$$\sigma_{abs} = 3k_m V Im\left(\frac{\epsilon_p - \epsilon_m}{\epsilon_p + 2\epsilon_m} \right),$$

where V is the volume of a particle.

1.5.2.2 Numerical calculation of efficiencies of Au NPs

As Au NPs are widely used in many applications, this subsection shows the computational results of efficiencies Qs defined in terms of σ as $Q = \sigma/\pi a^2$ of Au NPs in comparison with experimental results that will be shown later in this dissertation. The system studied in this case is a spherical Au NP with varying diameters suspended in water as the surrounding medium with $n_m = 1.33$ and $\mu_m = 0.999992 \cong 1$ [221, 222]. The wavelength-dependent complex refractive indices of gold $n_p(\lambda)$ were obtained from Johnson and Christy [197]. A linear interpolation was exploited to compute the complex refractive indices at intermediate wavelengths such that the calculation could be performed for any wavelength in range from 400 to 1000 nm. The relative magnetic permeability of gold is one ($\mu_p = 1$) [221, 222].

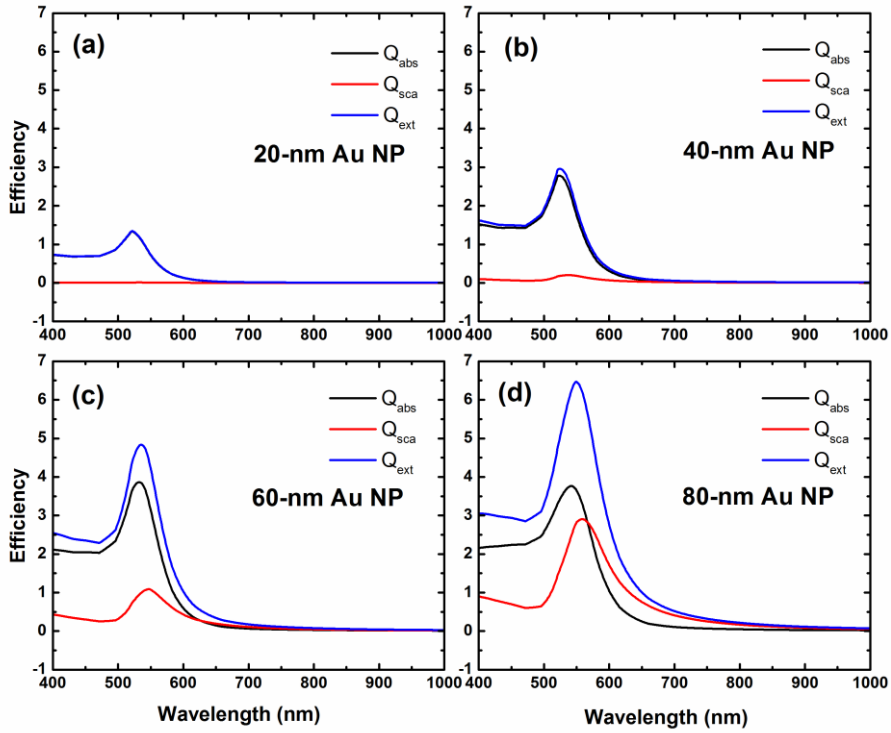

Figure 1.10: LSPR absorption (black), scattering (red) and extinction (blue) efficiencies calculated using Mie theory for spherically-shaped Au NPs with diameters ($d = 2a$) of (a) 20 nm, (b) 40 nm, (c) 60 nm, and (d) 80 nm. The black curve (a) almost coincides with the blue curve, indicating the absorption plays a dominant role in small particles.

Figure 1.10 plots the calculated Q_{abs}, Q_{sca}, and Q_{ext} of spherical Au NPs with diameters of 20, 40, 60, 80 nm, respectively in water. There are two interesting aspects which can be deduced from these plots. First, it is seen that the scattering efficiency increases as the size of a nanoparticle increases, while the absorption efficiency is larger than that of scattering as the size of a nanoparticle decreases. In other words, the extinction of a smaller particle is dominated by absorption, while the extinction (= scattering + absorption) of a larger particle is dominated by scattering. This is expected because Rayleigh theory predicts that the absorption and scattering efficiencies are proportional to the first and the second power of the particle's volume ($Q_{abs} \propto V$ and $Q_{sca} \propto V^2$), respectively. Second, the resonance wavelength corresponding to the maximum extinction λ_{LSPR} is red shifted, i.e. λ_{LSPR} increases to a longer wavelength, when the diameter of a nanoparticle increases (cf. Figure 1.11). This is due to electromagnetic retardation effect which is why

λ_{LSPR} is insensitive to particle size in the quasi-static regime where $d \ll \lambda$. This feature enables one to qualitatively determine the size or the agglomeration state of a particle from the extinction spectrum in the experiment, at least for sufficiently large particles.

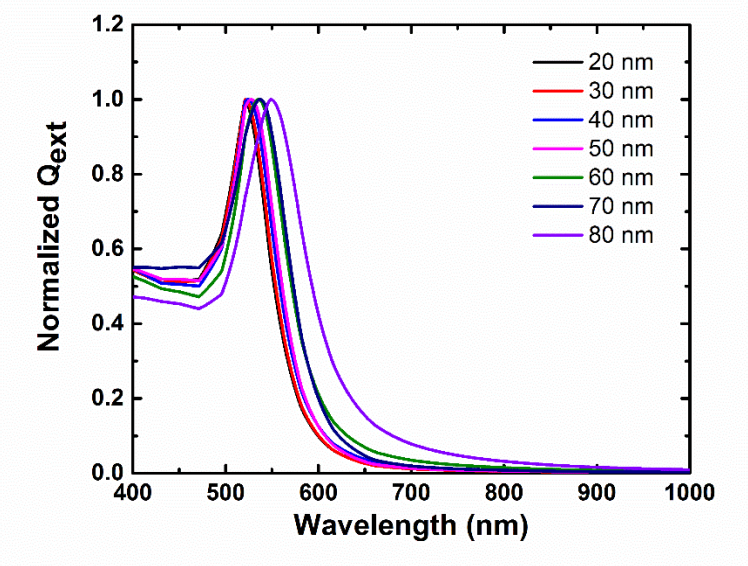

Figure 1.11: Normalized extinction efficiencies of spherical Au NPs of various diameters in the range 20-80 nm. As the Au NPs become larger, the resonance peaks shift to longer wavelengths and broaden due to an inhomogeneous polarization inside the nanoparticle by the incident electromagnetic field.

1.6 References

[1] M. Ieong, V. Narayanan, D. Singh, A. Topol, V. Chan, Z. Ren, Transistor scaling with novel materials, Materials Today, 9 (2006) 26-31.

[2] R.R. Schaller, Moore's law: past, present and future, IEEE Spectrum, 34 (1997) 52-59.

[3] M. Lundstrom, Moore's Law Forever?, Science, 299 (2003) 210.

[4] M.L. Brongersma, V.M. Shalaev, The Case for Plasmonics, Science, 328 (2010) 440.

[5] J.A. Schuller, E.S. Barnard, W. Cai, Y.C. Jun, J.S. White, M.L. Brongersma, Plasmonics for extreme light concentration and manipulation, Nature Materials, 9 (2010) 193.

[6] V. Naik Gururaj, M. Shalaev Vladimir, A. Boltasseva, Alternative Plasmonic Materials: Beyond Gold and Silver, Advanced Materials, 25 (2013) 3264-3294.

[7] Y. Liu, Q. Liu, S. Chen, F. Cheng, H. Wang, W. Peng, Surface Plasmon Resonance Biosensor Based on Smart Phone Platforms, Scientific Reports, 5 (2015) 12864.

[8] U. Jönsson, L. Fägerstam, B. Ivarsson, B. Johnsson, R. Karlsson, K. Lundh, S. Löfås, B. Persson, H. Roos, I. Rönnberg, Real-Time Biospecific Interaction Analysis Using Surface Plasmon Resonance and Sensor Chip Technology, 1991.

[9] B. Liedberg, C. Nylander, I. Lundström, Biosensing with surface plasmon resonance — how it all started, Biosensors and Bioelectronics, 10 (1995) i-ix.

[10] B. Liedberg, C. Nylander, I. Lunström, Surface plasmon resonance for gas detection and biosensing, Sensors and Actuators, 4 (1983) 299-304.

[11] C. Höppener, L. Novotny, Exploiting the light–metal interaction for biomolecular sensing and imaging, Quarterly Reviews of Biophysics, 45 (2012) 209-255.

[12] S. Lal, N.K. Grady, J. Kundu, C.S. Levin, J.B. Lassiter, N.J. Halas, Tailoring plasmonic substrates for surface enhanced spectroscopies, Chemical Society Reviews, 37 (2008) 898-911.

[13] B. Sharma, R.R. Frontiera, A.-I. Henry, E. Ringe, R.P. Van Duyne, SERS: Materials, applications, and the future, Materials Today, 15 (2012) 16-25.

[14] J. Dostálek, W. Knoll, Biosensors based on surface plasmon-enhanced fluorescence spectroscopy (Review), Biointerphases, 3 (2008) FD12-FD22.

[15] J.R. Lakowicz, K. Ray, M. Chowdhury, H. Szmacinski, Y. Fu, J. Zhang, K. Nowaczyk, Plasmon-controlled fluorescence: a new paradigm in fluorescence spectroscopy, Analyst, 133 (2008) 1308-1346.

[16] K.H. Drexhage, IV Interaction of Light with Monomolecular Dye Layers, in: E. Wolf (Ed.) Progress in Optics, Elsevier1974, pp. 163-232.

[17] J.-H. Song, T. Atay, S. Shi, H. Urabe, A.V. Nurmikko, Large Enhancement of Fluorescence Efficiency from CdSe/ZnS Quantum Dots Induced by Resonant Coupling to Spatially Controlled Surface Plasmons, Nano Letters, 5 (2005) 1557-1561.

[18] X. Zhang, C.A. Marocico, M. Lunz, V.A. Gerard, Y.K. Gun'ko, V. Lesnyak, N. Gaponik, A.S. Susha, A.L. Rogach, A.L. Bradley, Experimental and Theoretical Investigation of the Distance Dependence of Localized Surface Plasmon Coupled Förster Resonance Energy Transfer, ACS Nano, 8 (2014) 1273-1283.

[19] K.A. Willets, R.P. Van Duyne, Localized Surface Plasmon Resonance Spectroscopy and Sensing, Annual Review of Physical Chemistry, 58 (2007) 267-297.

[20] E.M. Purcell, Spontaneous emission probabilities at radio frequencies, 1946, pp. 681.

[21] H. Iwase, D. Englund, J. Vučković, Analysis of the Purcell effect in photonic and plasmonic crystals with losses, Opt. Express, 18 (2010) 16546-16560.

[22] T.W. Ebbesen, H.J. Lezec, H.F. Ghaemi, T. Thio, P.A. Wolff, Extraordinary optical transmission through sub-wavelength hole arrays, Nature, 391 (1998) 667.

[23] Y.M. Strelniker, Theory of optical transmission through elliptical nanohole arrays, Physical Review B, 76 (2007) 085409.

[24] A.G. Brolo, S.C. Kwok, M.G. Moffitt, R. Gordon, J. Riordon, K.L. Kavanagh, Enhanced Fluorescence from Arrays of Nanoholes in a Gold Film, Journal of the American Chemical Society, 127 (2005) 14936-14941.

[25] Q. Huang, Z. Huang, G. Meng, Y. Fu, J.R. Lakowicz, Plasmonic nanorod arrays for enhancement of single-molecule detection, Chemical Communications, 49 (2013) 11743-11745.

[26] Y.-W. Hao, H.-Y. Wang, Z.-Y. Zhang, X.-L. Zhang, Q.-D. Chen, H.-B. Sun, Time-Resolved Fluorescence Anisotropy of Surface Plasmon Coupled Emission on Metallic Gratings, The Journal of Physical Chemistry C, 117 (2013) 26734-26739.

[27] Z.Y. Zhang, H.Y. Wang, J.L. Du, X.L. Zhang, Y.W. Hao, Q.D. Chen, H.B. Sun, Surface Plasmon-Modulated Fluorescence on 2D Metallic Silver Gratings, IEEE Photonics Technology Letters, 27 (2015) 821-823.

[28] B. Yang, N. Lu, D. Qi, R. Ma, Q. Wu, J. Hao, X. Liu, Y. Mu, V. Reboud, N. Kehagias, M.S. Torres Clivia, C. Boey Freddy Yin, X. Chen, L. Chi, Tuning the Intensity of Metal-Enhanced Fluorescence by Engineering Silver Nanoparticle Arrays, Small, 6 (2010) 1038-1043.

[29] M. Szalkowski, K.U. Ashraf, H. Lokstein, S. Mackowski, R.J. Cogdell, D. Kowalska, Silver island film substrates for ultrasensitive fluorescence detection of (bio)molecules, Photosynthesis Research, 127 (2016) 103-108.

[30] H. Mishra, Y. Zhang, C.D. Geddes, Metal enhanced fluorescence of the fluorescent brightening agent Tinopal-CBX near silver island film, Dyes and Pigments, 91 (2011) 225-230.

[31] D.A. Weitz, S. Garoff, C.D. Hanson, T.J. Gramila, J.I. Gersten, Fluorescent lifetimes of molecules on silver-island films, Opt. Lett., 7 (1982) 89-91.

[32] Y. Zhang, K. Aslan, M.J.R. Previte, C.D. Geddes, Metal-enhanced fluorescence from copper substrates, Applied Physics Letters, 90 (2007) 173116.

[33] S.V. Karpov, V.S. Gerasimov, I.L. Isaev, V.A. Markel, Spectroscopic studies of fractal aggregates of silver nanospheres undergoing local restructuring, The Journal of Chemical Physics, 125 (2006) 111101.

[34] A.L. Feng, M.L. You, L. Tian, S. Singamaneni, M. Liu, Z. Duan, T.J. Lu, F. Xu, M. Lin, Distance-Dependent Plasmon-Enhanced Fluorescence of Upconversion Nanoparticles using Polyelectrolyte Multilayers as Tunable Spacers, Scientific Reports, 5 (2015) 7779.

[35] S. Schietinger, T. Aichele, H.-Q. Wang, T. Nann, O. Benson, Plasmon-Enhanced Upconversion in Single NaYF4:Yb3+/Er3+ Codoped Nanocrystals, Nano Letters, 10 (2010) 134-138.

[36] N. Mauser, D. Piatkowski, T. Mancabelli, M. Nyk, S. Mackowski, A. Hartschuh, Tip Enhancement of Upconversion Photoluminescence from Rare Earth Ion Doped Nanocrystals, ACS Nano, 9 (2015) 3617-3626.

[37] C.D. Bain, E.B. Troughton, Y.T. Tao, J. Evall, G.M. Whitesides, R.G. Nuzzo, Formation of monolayer films by the spontaneous assembly of organic thiols from solution onto gold, Journal of the American Chemical Society, 111 (1989) 321-335.

[38] K. Itano, J. Choi, M.F. Rubner, Mechanism of the pH-Induced Discontinuous Swelling/Deswelling Transitions of Poly(allylamine hydrochloride)-Containing Polyelectrolyte Multilayer Films, Macromolecules, 38 (2005) 3450-3460.

[39] J.A. Hiller, M.F. Rubner, Reversible Molecular Memory and pH-Switchable Swelling Transitions in Polyelectrolyte Multilayers, Macromolecules, 36 (2003) 4078-4083.

[40] S.E. Burke, C.J. Barrett, Acid−Base Equilibria of Weak Polyelectrolytes in Multilayer Thin Films, Langmuir, 19 (2003) 3297-3303.

[41] J. Choi, M.F. Rubner, Influence of the Degree of Ionization on Weak Polyelectrolyte Multilayer Assembly, Macromolecules, 38 (2005) 116-124.

[42] J. Goicoechea, F.J. Arregui, J.M. Corres, I.R. Matias, Study and Optimization of Self-Assembled Polymeric Multilayer Structures with Neutral Red for pH Sensing Applications, Journal of Sensors, 2008 (2008) 7.

[43] R.T. Hill, K.M. Kozek, A. Hucknall, D.R. Smith, A. Chilkoti, Nanoparticle–Film Plasmon Ruler Interrogated with Transmission Visible Spectroscopy, ACS Photonics, 1 (2014) 974-984.

[44] N. Parveen, M. Schönhoff, Swelling and Stability of Polyelectrolyte Multilayers in Ionic Liquid Solutions, Macromolecules, 46 (2013) 7880-7888.

[45] O.M. Tanchak, C.J. Barrett, Swelling Dynamics of Multilayer Films of Weak Polyelectrolytes, Chemistry of Materials, 16 (2004) 2734-2739.

[46] J. Zhang, N.A. Peppas, Synthesis and Characterization of pH- and Temperature-Sensitive Poly(methacrylic acid)/Poly(N-isopropylacrylamide) Interpenetrating Polymeric Networks, Macromolecules, 33 (2000) 102-107.

[47] N.S. Abadeer, M.R. Brennan, W.L. Wilson, C.J. Murphy, Distance and Plasmon Wavelength Dependent Fluorescence of Molecules Bound to Silica-Coated Gold Nanorods, ACS Nano, 8 (2014) 8392-8406.

[48] L. Bujak, M. Olejnik, T.H.P. Brotosudarmo, M.K. Schmidt, N. Czechowski, D. Piatkowski, J. Aizpurua, R.J. Cogdell, W. Heiss, S. Mackowski, Polarization control of metal-enhanced fluorescence in hybrid assemblies of photosynthetic complexes and gold nanorods, Physical Chemistry Chemical Physics, 16 (2014) 9015-9022.

[49] D. Cheng, Q.-H. Xu, Separation distance dependent fluorescence enhancement of fluorescein isothiocyanate by silver nanoparticles, Chemical Communications, DOI 10.1039/B612401A(2007) 248-250.

[50] P. Reineck, D. Gómez, S.H. Ng, M. Karg, T. Bell, P. Mulvaney, U. Bach, Distance and Wavelength Dependent Quenching of Molecular Fluorescence by Au@SiO2 Core–Shell Nanoparticles, ACS Nano, 7 (2013) 6636-6648.

[51] Y. Zhang, A. Dragan, C.D. Geddes, Wavelength Dependence of Metal-Enhanced Fluorescence, The Journal of Physical Chemistry C, 113 (2009) 12095-12100.

[52] K.A. Kang, J. Wang, J.B. Jasinski, S. Achilefu, Fluorescence Manipulation by Gold Nanoparticles: From Complete Quenching to Extensive Enhancement, Journal of Nanobiotechnology, 9 (2011) 16.

[53] G. Schneider, G. Decher, N. Nerambourg, R. Praho, M.H.V. Werts, M. Blanchard-Desce, Distance-Dependent Fluorescence Quenching on Gold Nanoparticles Ensheathed with Layer-by-Layer Assembled Polyelectrolytes, Nano Letters, 6 (2006) 530-536.

[54] S. Yuan, F. Ge, Y. Chen, Z. Cai, Tunable metal-enhanced fluorescence by pH-responsive polyacryloyl hydrazide capped Ag nanoparticles, RSC Advances, 7 (2017) 6358-6363.

[55] K.L. Kelly, E. Coronado, L.L. Zhao, G.C. Schatz, The Optical Properties of Metal Nanoparticles: The Influence of Size, Shape, and Dielectric Environment, The Journal of Physical Chemistry B, 107 (2003) 668-677.

[56] S. Link, M.A. El-Sayed, Size and Temperature Dependence of the Plasmon Absorption of Colloidal Gold Nanoparticles, The Journal of Physical Chemistry B, 103 (1999) 4212-4217.

[57] C. Noguez, Surface Plasmons on Metal Nanoparticles: The Influence of Shape and Physical Environment, The Journal of Physical Chemistry C, 111 (2007) 3806-3819.

[58] I.O. Sosa, C. Noguez, R.G. Barrera, Optical Properties of Metal Nanoparticles with Arbitrary Shapes, The Journal of Physical Chemistry B, 107 (2003) 6269-6275.

[59] T.A. El-Brolossy, T. Abdallah, M.B. Mohamed, S. Abdallah, K. Easawi, S. Negm, H. Talaat, Shape and size dependence of the surface plasmon resonance of gold nanoparticles studied by Photoacoustic technique, The European Physical Journal Special Topics, 153 (2008) 361-364.

[60] A.M. Alkilany, S.E. Lohse, C.J. Murphy, The Gold Standard: Gold Nanoparticle Libraries To Understand the Nano–Bio Interface, Accounts of Chemical Research, 46 (2013) 650-661.

[61] X. Huang, P.K. Jain, I.H. El-Sayed, M.A. El-Sayed, Gold nanoparticles: interesting optical properties and recent applications in cancer diagnostics and therapy, Nanomedicine, 2 (2007) 681-693.

[62] X. Huang, M.A. El-Sayed, Gold nanoparticles: Optical properties and implementations in cancer diagnosis and photothermal therapy, Journal of Advanced Research, 1 (2010) 13-28.

[63] W. Cai, T. Gao, H. Hong, J. Sun, Applications of gold nanoparticles in cancer nanotechnology, Nanotechnology, science and applications, 2008 (2008) 10.2147/NSA.S3788.

[64] L.A. Dykman, N.G. Khlebtsov, Gold Nanoparticles in Biology and Medicine: Recent Advances and Prospects, Acta Naturae, 3 (2011) 34-55.

[65] M. Homberger, U. Simon, On the application potential of gold nanoparticles in nanoelectronics and biomedicine, Philosophical Transactions of the Royal Society A: Mathematical, Physical and Engineering Sciences, 368 (2010) 1405.

[66] E.A. Coronado, E.R. Encina, F.D. Stefani, Optical properties of metallic nanoparticles: manipulating light, heat and forces at the nanoscale, Nanoscale, 3 (2011) 4042-4059.

[67] J. Spadavecchia, E. Apchain, M. Albéric, E. Fontan, I. Reiche, One-Step Synthesis of Collagen Hybrid Gold Nanoparticles and Formation on Egyptian-like Gold-Plated Archaeological Ivory, Angewandte Chemie International Edition, 53 (2014) 8363-8366.

[68] I. Freestone, N. Meeks, M. Sax, C. Higgitt, The Lycurgus Cup — A Roman nanotechnology, Gold Bulletin, 40 (2007) 270-277.

[69] F.E. Wagner, S. Haslbeck, L. Stievano, S. Calogero, Q.A. Pankhurst, K.P. Martinek, Before striking gold in gold-ruby glass, Nature, 407 (2000) 691-692.

[70] J. Moir, COLLOIDAL GOLD AND "PURPLE OF CASSIUS.", Transactions of the Royal Society of South Africa, 2 (1910) 203-204.

[71] M. Blosi, S. Albonetti, F. Gatti, G. Baldi, M. Dondi, Au–Ag nanoparticles as red pigment in ceramic inks for digital decoration, Dyes and Pigments, 94 (2012) 355-362.

[72] M. Faraday, The Bakerian Lecture: Experimental Relations of Gold (and Other Metals) to Light, Philosophical Transactions of the Royal Society of London, 147 (1857) 145-181.

[73] G. Mie, Beiträge zur Optik trüber Medien, speziell kolloidaler Metallösungen, Annalen der Physik, 330 (1908) 377-445.

[74] P.K. Jain, K.S. Lee, I.H. El-Sayed, M.A. El-Sayed, Calculated Absorption and Scattering Properties of Gold Nanoparticles of Different Size, Shape, and Composition: Applications in Biological Imaging and Biomedicine, The Journal of Physical Chemistry B, 110 (2006) 7238-7248.

[75] C.L. Nehl, H. Liao, J.H. Hafner, Optical Properties of Star-Shaped Gold Nanoparticles, Nano Letters, 6 (2006) 683-688.

[76] L. Nguyen Ngoc, V. Le Van, K. Chu Dinh, D. Sai Cong, N. Cao Thi, H. Pham Thi, T. Nguyen Duy, Q. Luu Manh, Synthesis and optical properties of colloidal gold nanoparticles, Journal of Physics: Conference Series, 187 (2009) 012026.

[77] M.-C. Daniel, D. Astruc, Gold Nanoparticles: Assembly, Supramolecular Chemistry, Quantum-Size-Related Properties, and Applications toward Biology, Catalysis, and Nanotechnology, Chemical Reviews, 104 (2004) 293-346.

[78] G. Frens, Controlled Nucleation for the Regulation of the Particle Size in Monodisperse Gold Suspensions, Nature, 241 (1973) 20-22.

[79] J. Turkevich, P.C. Stevenson, J. Hillier, A study of the nucleation and growth processes in the synthesis of colloidal gold, Discussions of the Faraday Society, 11 (1951) 55-75.

[80] C. Ziegler, A. Eychmüller, Seeded Growth Synthesis of Uniform Gold Nanoparticles with Diameters of 15−300 nm, The Journal of Physical Chemistry C, 115 (2011) 4502-4506.

[81] A. Gole, C.J. Murphy, Seed-Mediated Synthesis of Gold Nanorods: Role of the Size and Nature of the Seed, Chemistry of Materials, 16 (2004) 3633-3640.

[82] N.D. Burrows, S. Harvey, F.A. Idesis, C.J. Murphy, Understanding the Seed-Mediated Growth of Gold Nanorods through a Fractional Factorial Design of Experiments, Langmuir, 33 (2017) 1891-1907.

[83] S. Mössmer, J.P. Spatz, M. Möller, T. Aberle, J. Schmidt, W. Burchard, Solution Behavior of Poly(styrene)-block-poly(2-vinylpyridine) Micelles Containing Gold Nanoparticles, Macromolecules, 33 (2000) 4791-4798.

[84] G.B. Khomutov, Two-dimensional synthesis of anisotropic nanoparticles, Colloids and Surfaces A: Physicochemical and Engineering Aspects, 202 (2002) 243-267.

[85] V.G. Pol, A. Gedanken, J. Calderon-Moreno, Deposition of Gold Nanoparticles on Silica Spheres: A Sonochemical Approach, Chemistry of Materials, 15 (2003) 1111-1118.

[86] H. Mühlpfordt, The preparation of colloidal gold particles using tannic acid as an additional reducing agent, Experientia, 38 (1982) 1127-1128.

[87] N.G. Bastús, J. Comenge, V. Puntes, Kinetically Controlled Seeded Growth Synthesis of Citrate-Stabilized Gold Nanoparticles of up to 200 nm: Size Focusing versus Ostwald Ripening, Langmuir, 27 (2011) 11098-11105.

[88] D. Shenoy, W. Fu, J. Li, C. Crasto, G. Jones, C. DiMarzio, S. Sridhar, M. Amiji, Surface functionalization of gold nanoparticles using hetero-bifunctional poly(ethylene glycol) spacer for intracellular tracking and delivery, International Journal of Nanomedicine, 1 (2006) 51-57.

[89] M. Brust, M. Walker, D. Bethell, D.J. Schiffrin, R. Whyman, Synthesis of thiol-derivatised gold nanoparticles in a two-phase Liquid-Liquid system, Journal of the Chemical Society, Chemical Communications, DOI 10.1039/C39940000801(1994) 801-802.

[90] V.K. LaMer, R.H. Dinegar, Theory, Production and Mechanism of Formation of Monodispersed Hydrosols, Journal of the American Chemical Society, 72 (1950) 4847-4854.

[91] D. Lee, S. Yoon, Gold Nanocube–Nanosphere Dimers: Preparation, Plasmon Coupling, and Surface-Enhanced Raman Scattering, The Journal of Physical Chemistry C, 119 (2015) 7873-7882.

[92] L.V. Brown, H. Sobhani, J.B. Lassiter, P. Nordlander, N.J. Halas, Heterodimers: Plasmonic Properties of Mismatched Nanoparticle Pairs, ACS Nano, 4 (2010) 819-832.

[93] Z. Zhang, S. Zhang, M. Lin, DNA-embedded Au-Ag core-shell nanoparticles assembled on silicon slides as a reliable SERS substrate, Analyst, 139 (2014) 2207-2213.

[94] H. Kuang, X. Chen, C. Hao, W. Ma, L. Xu, C. Xu, Immuno-driven plasmonic oligomer sensor for the ultrasensitive detection of antibiotics, RSC Advances, 3 (2013) 17294-17299.

[95] Y. Zhu, L. Xu, W. Ma, Z. Xu, H. Kuang, L. Wang, C. Xu, A one-step homogeneous plasmonic circular dichroism detection of aqueous mercury ions using nucleic acid functionalized gold nanorods, Chemical Communications, 48 (2012) 11889-11891.

[96] Z. Xu, L. Xu, M. Liz-Marzán Luis, W. Ma, A. Kotov Nicholas, L. Wang, H. Kuang, C. Xu, Sensitive Detection of Silver Ions Based on Chiroplasmonic Assemblies of Nanoparticles, Advanced Optical Materials, 1 (2013) 626-630.

[97] W. Ma, H. Kuang, L. Xu, L. Ding, C. Xu, L. Wang, N.A. Kotov, Attomolar DNA detection with chiral nanorod assemblies, Nature Communications, 4 (2013) 2689.

[98] Y. Zhao, L. Xu, L.M. Liz-Marzán, H. Kuang, W. Ma, A. Asenjo-Garcı́a, F.J. García de Abajo, N.A. Kotov, L. Wang, C. Xu, Alternating Plasmonic Nanoparticle Heterochains Made by Polymerase Chain Reaction and Their Optical Properties, The Journal of Physical Chemistry Letters, 4 (2013) 641-647.

[99] J. Sharma, R. Chhabra, A. Cheng, J. Brownell, Y. Liu, H. Yan, Control of Self-Assembly of DNA Tubules Through Integration of Gold Nanoparticles, Science, 323 (2009) 112.

[100] A.J. Mastroianni, S.A. Claridge, A.P. Alivisatos, Pyramidal and Chiral Groupings of Gold Nanocrystals Assembled Using DNA Scaffolds, Journal of the American Chemical Society, 131 (2009) 8455-8459.

[101] J. Lee, P. Hernandez, J. Lee, A.O. Govorov, N.A. Kotov, Exciton–plasmon interactions in molecular spring assemblies of nanowires and wavelength-based protein detection, Nature Materials, 6 (2007) 291.

[102] A.P. Alivisatos, K.P. Johnsson, X. Peng, T.E. Wilson, C.J. Loweth, M.P. Bruchez Jr, P.G. Schultz, Organization of 'nanocrystal molecules' using DNA, Nature, 382 (1996) 609.

[103] J.I.L. Chen, Y. Chen, D.S. Ginger, Plasmonic Nanoparticle Dimers for Optical Sensing of DNA in Complex Media, Journal of the American Chemical Society, 132 (2010) 9600-9601.

[104] B. Peng, G. Li, D. Li, S. Dodson, Q. Zhang, J. Zhang, Y.H. Lee, H.V. Demir, X. Yi Ling, Q. Xiong, Vertically Aligned Gold Nanorod Monolayer on Arbitrary Substrates: Self-Assembly and Femtomolar Detection of Food Contaminants, ACS Nano, 7 (2013) 5993-6000.

[105] Y. Min, M. Akbulut, K. Kristiansen, Y. Golan, J. Israelachvili, The role of interparticle and external forces in nanoparticle assembly, Nature Materials, 7 (2008) 527.

[106] S.-Y. Zhang, M.D. Regulacio, M.-Y. Han, Self-assembly of colloidal one-dimensional nanocrystals, Chemical Society Reviews, 43 (2014) 2301-2323.

[107] A.M. Kalsin, M. Fialkowski, M. Paszewski, S.K. Smoukov, K.J.M. Bishop, B.A. Grzybowski, Electrostatic Self-Assembly of Binary Nanoparticle Crystals with a Diamond-Like Lattice, Science, 312 (2006) 420.

[108] P.F. Damasceno, M. Engel, S.C. Glotzer, Predictive Self-Assembly of Polyhedra into Complex Structures, Science, 337 (2012) 453.

[109] Z. Zhu, W. Liu, Z. Li, B. Han, Y. Zhou, Y. Gao, Z. Tang, Manipulation of Collective Optical Activity in One-Dimensional Plasmonic Assembly, ACS Nano, 6 (2012) 2326-2332.

[110] Z. Sun, W. Ni, Z. Yang, X. Kou, L. Li, J. Wang, pH-Controlled Reversible Assembly and Disassembly of Gold Nanorods, Small, 4 (2008) 1287-1292.

[111] A. Lee, G.F.S. Andrade, A. Ahmed, M.L. Souza, N. Coombs, E. Tumarkin, K. Liu, R. Gordon, A.G. Brolo, E. Kumacheva, Probing Dynamic Generation of Hot-Spots in Self-Assembled Chains of Gold Nanorods by Surface-Enhanced Raman Scattering, Journal of the American Chemical Society, 133 (2011) 7563-7570.

[112] A. Lukach, K. Liu, H. Therien-Aubin, E. Kumacheva, Controlling the Degree of Polymerization, Bond Lengths, and Bond Angles of Plasmonic Polymers, Journal of the American Chemical Society, 134 (2012) 18853-18859.

[113] Z. Nie, D. Fava, M. Rubinstein, E. Kumacheva, "Supramolecular" Assembly of Gold Nanorods End-Terminated with Polymer "Pom-Poms": Effect of Pom-Pom Structure on the Association Modes, Journal of the American Chemical Society, 130 (2008) 3683-3689.

[114] S. Gupta, Q. Zhang, T. Emrick, T.P. Russell, "Self-Corralling" Nanorods under an Applied Electric Field, Nano Letters, 6 (2006) 2066-2069.

[115] T.B. Jones, Electromechanics of Particles, Cambridge University Press, Cambridge, 1995.

[116] L. Xu, W. Ma, L. Wang, C. Xu, H. Kuang, N.A. Kotov, Nanoparticle assemblies: dimensional transformation of nanomaterials and scalability, Chemical Society Reviews, 42 (2013) 3114-3126.

[117] C.A. Mirkin, R.L. Letsinger, R.C. Mucic, J.J. Storhoff, A DNA-based method for rationally assembling nanoparticles into macroscopic materials, Nature, 382 (1996) 607.

[118] X. Wu, L. Xu, L. Liu, W. Ma, H. Yin, H. Kuang, L. Wang, C. Xu, N.A. Kotov, Unexpected Chirality of Nanoparticle Dimers and Ultrasensitive Chiroplasmonic Bioanalysis, Journal of the American Chemical Society, 135 (2013) 18629-18636.

[119] T. Chen, Y. Hong, B.M. Reinhard, Probing DNA Stiffness through Optical Fluctuation Analysis of Plasmon Rulers, Nano Letters, 15 (2015) 5349-5357.

[120] L. Guo, Y. Xu, A.R. Ferhan, G. Chen, D.-H. Kim, Oriented Gold Nanoparticle Aggregation for Colorimetric Sensors with Surprisingly High Analytical Figures of Merit, Journal of the American Chemical Society, 135 (2013) 12338-12345.

[121] L.H. Tan, H. Xing, H. Chen, Y. Lu, Facile and Efficient Preparation of Anisotropic DNA-Functionalized Gold Nanoparticles and Their Regioselective Assembly, Journal of the American Chemical Society, 135 (2013) 17675-17678.

[122] M.M. Maye, D. Nykypanchuk, M. Cuisinier, D. van der Lelie, O. Gang, Stepwise surface encoding for high-throughput assembly of nanoclusters, Nature Materials, 8 (2009) 388.

[123] L. Wang, Y. Zhu, L. Xu, W. Chen, H. Kuang, L. Liu, A. Agarwal, C. Xu, A. Kotov Nicholas Side-by-Side and End-to-End Gold Nanorod Assemblies for Environmental Toxin Sensing, Angewandte Chemie International Edition, 49 (2010) 5472-5475.

[124] P. Pramod, K.G. Thomas, Plasmon Coupling in Dimers of Au Nanorods, Advanced Materials, 20 (2008) 4300-4305.

[125] J. Zhou, C. Fang, Y. Liu, Y. Zhao, N. Zhang, X. Liu, F. Wang, D. Shangguan, Visible-light-induced cleavage of 4-[small alpha]-amino acid substituted naphthalimides and its application in DNA photocleavage, Organic & Biomolecular Chemistry, 13 (2015) 3931-3935.

[126] J.A. Barltrop, P.J. Plant, P. Schofield, Photosensitive protective groups, Chemical Communications (London), DOI 10.1039/C19660000822(1966) 822-823.

[127] A. Patchornik, B. Amit, R.B. Woodward, Photosensitive protecting groups, Journal of the American Chemical Society, 92 (1970) 6333-6335.

[128] J. Nakanishi, Y. Kikuchi, T. Takarada, H. Nakayama, K. Yamaguchi, M. Maeda, Photoactivation of a Substrate for Cell Adhesion under Standard Fluorescence Microscopes, Journal of the American Chemical Society, 126 (2004) 16314-16315.

[129] A. Azagarsamy Malar, S. Anseth Kristi, Wavelength-Controlled Photocleavage for the Orthogonal and Sequential Release of Multiple Proteins, Angewandte Chemie International Edition, 52 (2013) 13803-13807.

[130] X. Yuan, K. Fischer, W. Schärtl, Photocleavable Microcapsules Built from Photoreactive Nanospheres, Langmuir, 21 (2005) 9374-9380.

[131] Y. Fang, Y. Li, H. Xu, M. Sun, Ascertaining p,p′-Dimercaptoazobenzene Produced from p-Aminothiophenol by Selective Catalytic Coupling Reaction on Silver Nanoparticles, Langmuir, 26 (2010) 7737-7746.

[132] E.M. See, C.L. Peck, X. Guo, W. Santos, H.D. Robinson, Plasmon-Induced Photoreaction of o-Nitrobenzyl-Based Ligands under 550 nm Light, The Journal of Physical Chemistry C, DOI 10.1021/acs.jpcc.7b00707(2017).

[133] J. Cui, S. Miguel Verónica, A. del Campo, Light-Triggered Multifunctionality at Surfaces Mediated by Photolabile Protecting Groups, Macromolecular Rapid Communications, 34 (2012) 310-329.

[134] S.V. Wegner, O.I. Sentürk, J.P. Spatz, Photocleavable linker for the patterning of bioactive molecules, Scientific Reports, 5 (2015) 18309.

[135] C. Brieke, F. Rohrbach, A. Gottschalk, G. Mayer, A. Heckel, Light-Controlled Tools, Angewandte Chemie International Edition, 51 (2012) 8446-8476.

[136] D. Liu, Y. Xie, H. Shao, X. Jiang, Using Azobenzene-Embedded Self-Assembled Monolayers To Photochemically Control Cell Adhesion Reversibly, Angewandte Chemie International Edition, 48 (2009) 4406-4408.

[137] A. Bagheri, J. Yeow, H. Arandiyan, J. Xu, C. Boyer, M. Lim, Polymerization of a Photocleavable Monomer Using Visible Light, Macromolecular Rapid Communications, 37 (2016) 905-910.

[138] C.G. Bochet, Photolabile protecting groups and linkers, Journal of the Chemical Society, Perkin Transactions 1, DOI 10.1039/B009522M(2002) 125-142.

[139] P. Wang, Photolabile Protecting Groups: Structure and Reactivity, Asian Journal of Organic Chemistry, 2 (2013) 452-464.

[140] C.-P. Huang, Y.-Y. Zhu, Plasmonics: Manipulating Light at the Subwavelength Scale, Active and Passive Electronic Components, 2007 (2007) 13.

[141] R. Zia, J.A. Schuller, A. Chandran, M.L. Brongersma, Plasmonics: the next chip-scale technology, Materials Today, 9 (2006) 20-27.

[142] P. Berini, Plasmon-polariton waves guided by thin lossy metal films of finite width: Bound modes of symmetric structures, Physical Review B, 61 (2000) 10484-10503.

[143] P. Berini, Plasmon-polariton waves guided by thin lossy metal films of finite width: Bound modes of asymmetric structures, Physical Review B, 63 (2001) 125417.

[144] P. Berini, R. Charbonneau, N. Lahoud, G. Mattiussi, Characterization of long-range surface-plasmon-polariton waveguides, Journal of Applied Physics, 98 (2005) 043109.

[145] V.N. Konopsky, E.V. Alieva, Long-Range Propagation of Plasmon Polaritons in a Thin Metal Film on a One-Dimensional Photonic Crystal Surface, Physical Review Letters, 97 (2006) 253904.

[146] J.R. Krenn, B. Lamprecht, H. Ditlbacher, G. Schider, M. Salerno, A. Leitner, F.R. Aussenegg, Non–diffraction-limited light transport by gold nanowires, EPL (Europhysics Letters), 60 (2002) 663.

[147] W. Xu, X. Ling, J. Xiao, M.S. Dresselhaus, J. Kong, H. Xu, Z. Liu, J. Zhang, Surface enhanced Raman spectroscopy on a flat graphene surface, Proceedings of the National Academy of Sciences of the United States of America, 109 (2012) 9281-9286.

[148] S.J. Zhen, C.Z. Huang, J. Wang, Y.F. Li, End-to-End Assembly of Gold Nanorods on the Basis of Aptamer−Protein Recognition, The Journal of Physical Chemistry C, 113 (2009) 21543-21547.

[149] C. Novara, S. Dalla Marta, A. Virga, A. Lamberti, A. Angelini, A. Chiadò, P. Rivolo, F. Geobaldo, V. Sergo, A. Bonifacio, F. Giorgis, SERS-Active Ag Nanoparticles on Porous Silicon and PDMS

Substrates: A Comparative Study of Uniformity and Raman Efficiency, The Journal of Physical Chemistry C, 120 (2016) 16946-16953.

[150] S.Y. Lee, L. Hung, G.S. Lang, J.E. Cornett, I.D. Mayergoyz, O. Rabin, Dispersion in the SERS Enhancement with Silver Nanocube Dimers, ACS Nano, 4 (2010) 5763-5772.

[151] P.H.C. Camargo, L. Au, M. Rycenga, W. Li, Y. Xia, Measuring the SERS enhancement factors of dimers with different structures constructed from silver nanocubes, Chemical Physics Letters, 484 (2010) 304-308.

[152] O. Rabin, S.Y. Lee, SERS Substrates by the Assembly of Silver Nanocubes: High-Throughput and Enhancement Reliability Considerations, Journal of Nanotechnology, 2012 (2012) 12.

[153] F. Hao, C.L. Nehl, J.H. Hafner, P. Nordlander, Plasmon Resonances of a Gold Nanostar, Nano Letters, 7 (2007) 729-732.

[154] C. Hrelescu, T.K. Sau, A.L. Rogach, F. Jäckel, J. Feldmann, Single gold nanostars enhance Raman scattering, Applied Physics Letters, 94 (2009) 153113.

[155] W. Ma, M. Sun, L. Xu, L. Wang, H. Kuang, C. Xu, A SERS active gold nanostar dimer for mercury ion detection, Chemical Communications, 49 (2013) 4989-4991.

[156] J.D. Caldwell, O.J. Glembocki, F.J. Bezares, M.I. Kariniemi, J.T. Niinistö, T.T. Hatanpää, R.W. Rendell, M. Ukaegbu, M.K. Ritala, S.M. Prokes, C.M. Hosten, M.A. Leskelä, R. Kasica, Large-area plasmonic hot-spot arrays: sub-2 nm interparticle separations with plasma-enhanced atomic layer deposition of Ag on periodic arrays of Si nanopillars, Opt. Express, 19 (2011) 26056-26064.

[157] M. Bardhan, B. Satpati, T. Ghosh, D. Senapati, Synergistically controlled nano-templated growth of tunable gold bud-to-blossom nanostructures: a pragmatic growth mechanism, Journal of Materials Chemistry C, 2 (2014) 3795-3804.

[158] S.P. Hastings, Z. Qian, P. Swanglap, Y. Fang, N. Engheta, S.-J. Park, S. Link, Z. Fakhraai, Modal interference in spiky nanoshells, Opt. Express, 23 (2015) 11290-11311.

[159] P. Das, T.K. Chini, Substrate Induced Symmetry Breaking in Penta-twinned Gold Nanorod Probed by Free Electron Impact, The Journal of Physical Chemistry C, 118 (2014) 26284-26291.

[160] J. Nelayah, M. Kociak, O. Stéphan, F.J. García de Abajo, M. Tencé, L. Henrard, D. Taverna, I. Pastoriza-Santos, L.M. Liz-Marzán, C. Colliex, Mapping surface plasmons on a single metallic nanoparticle, Nature Physics, 3 (2007) 348.

[161] P. Das, T.K. Chini, J. Pond, Probing Higher Order Surface Plasmon Modes on Individual Truncated Tetrahedral Gold Nanoparticle Using Cathodoluminescence Imaging and Spectroscopy Combined with FDTD Simulations, The Journal of Physical Chemistry C, 116 (2012) 15610-15619.

[162] A. Maity, A. Maiti, P. Das, D. Senapati, T. Kumar Chini, Effect of Intertip Coupling on the Plasmonic Behavior of Individual Multitipped Gold Nanoflower, ACS Photonics, 1 (2014) 1290-1297.

[163] D. Radziuk, H. Moehwald, Prospects for plasmonic hot spots in single molecule SERS towards the chemical imaging of live cells, Physical Chemistry Chemical Physics, 17 (2015) 21072-21093.

[164] M.K. Hossain, Y. Kitahama, G.G. Huang, X. Han, Y. Ozaki, Surface-enhanced Raman scattering: realization of localized surface plasmon resonance using unique substrates and methods, Analytical and Bioanalytical Chemistry, 394 (2009) 1747-1760.

[165] X. Dou, P.-Y. Chung, P. Jiang, J. Dai, Surface plasmon resonance and surface-enhanced Raman scattering sensing enabled by digital versatile discs, Applied Physics Letters, 100 (2012) 041116.

[166] S.A. Meyer, E.C. Le Ru, P.G. Etchegoin, Combining Surface Plasmon Resonance (SPR) Spectroscopy with Surface-Enhanced Raman Scattering (SERS), Analytical Chemistry, 83 (2011) 2337-2344.

[167] T. Ming, L. Zhao, Z. Yang, H. Chen, L. Sun, J. Wang, C. Yan, Strong Polarization Dependence of Plasmon-Enhanced Fluorescence on Single Gold Nanorods, Nano Letters, 9 (2009) 3896-3903.

[168] K.L. Knappenberger, D.B. Wong, W. Xu, A.M. Schwartzberg, A. Wolcott, J.Z. Zhang, S.R. Leone, Excitation-Wavelength Dependence of Fluorescence Intermittency in CdSe Nanorods, ACS Nano, 2 (2008) 2143-2153.

[169] S.-H. Chang, S.K. Gray, G.C. Schatz, Surface plasmon generation and light transmission by isolated nanoholes and arrays of nanoholes in thin metal films, Opt. Express, 13 (2005) 3150-3165.

[170] A.G. Brolo, R. Gordon, B. Leathem, K.L. Kavanagh, Surface Plasmon Sensor Based on the Enhanced Light Transmission through Arrays of Nanoholes in Gold Films, Langmuir, 20 (2004) 4813-4815.

[171] L. Wang, Q. Song, Q. Liu, D. He, J. Ouyang, Plasmon-Enhanced Fluorescence-Based Core–Shell Gold Nanorods as a Near-IR Fluorescent Turn-On Sensor for the Highly Sensitive Detection of Pyrophosphate in Aqueous Solution, Advanced Functional Materials, 25 (2015) 7017-7027.

[172] S.A. Camacho, P.H.B. Aoki, P. Albella, O.N. Oliveira, C.J.L. Constantino, R.F. Aroca, Increasing the Enhancement Factor in Plasmon-Enhanced Fluorescence with Shell-Isolated Nanoparticles, The Journal of Physical Chemistry C, 120 (2016) 20530-20535.

[173] K. Hayashi, M. Nakamura, H. Miki, S. Ozaki, M. Abe, T. Matsumoto, K. Ishimura, Gold nanoparticle cluster-plasmon-enhanced fluorescent silica core-shell nanoparticles for X-ray computed tomography-fluorescence dual-mode imaging of tumors, Chemical Communications, 49 (2013) 5334-5336.

[174] K. Rivoire, A. Kinkhabwala, F. Hatami, W.T. Masselink, Y. Avlasevich, K. Müllen, W.E. Moerner, J. Vučković, Lithographic positioning of fluorescent molecules on high-Q photonic crystal cavities, Applied Physics Letters, 95 (2009) 123113.

[175] J. Chen, Y. Jin, N. Fahruddin, J.X. Zhao, Development of Gold Nanoparticle-Enhanced Fluorescent Nanocomposites, Langmuir, 29 (2013) 1584-1591.

[176] R. v. Baltz, Plasmons and Surface Plasmons in Bulk Metals, Metallic Clusters, and Metallic Heterostructures, in: B. Di Bartolo, S. Kyrkos (Eds.) Spectroscopy and Dynamics of Collective Excitations in Solids, Springer US, Boston, MA, 1997, pp. 303-338.

[177] I. Langmuir, Oscillations in Ionized Gases, Proceedings of the National Academy of Sciences of the United States of America, 14 (1928) 627-637.

[178] D. Pines, Elementary excitations in solids, Perseus1966.

[179] D. Bohm, D. Pines, A Collective Description of Electron Interactions. I. Magnetic Interactions, Physical Review, 82 (1951) 625-634.

[180] D. Pines, D. Bohm, A Collective Description of Electron Interactions: II. Collective vs Individual Particle Aspects of the Interactions, Physical Review, 85 (1952) 338-353.

[181] D. Bohm, D. Pines, A Collective Description of Electron Interactions: III. Coulomb Interactions in a Degenerate Electron Gas, Physical Review, 92 (1953) 609-625.

[182] D. Pines, A Collective Description of Electron Interactions: IV. Electron Interaction in Metals, Physical Review, 92 (1953) 626-636.

[183] C.J. Powell, J.B. Swan, Effect of Oxidation on the Characteristic Loss Spectra of Aluminum and Magnesium, Physical Review, 118 (1960) 640-643.

[184] J. Zenneck, Über die Fortpflanzung ebener elektromagnetischer Wellen längs einer ebenen Leiterfläche und ihre Beziehung zur drahtlosen Telegraphie, Annalen der Physik, 328 (1907) 846-866.

[185] A. Sommerfeld, Über die Ausbreitung der Wellen in der drahtlosen Telegraphie, Annalen der Physik, 333 (1909) 665-736.

[186] J.-J. Greffet, Introduction to Surface Plasmon Theory, in: S. Enoch, N. Bonod (Eds.) Plasmonics: From Basics to Advanced Topics, Springer Berlin Heidelberg, Berlin, Heidelberg, 2012, pp. 105-148.

[187] M.S. Tame, K.R. McEnery, Ş.K. Özdemir, J. Lee, S.A. Maier, M.S. Kim, Quantum plasmonics, Nature Physics, 9 (2013) 329.

[188] J.J. Hopfield, Theory of the Contribution of Excitons to the Complex Dielectric Constant of Crystals, Physical Review, 112 (1958) 1555-1567.

[189] J.M. Elson, R.H. Ritchie, Photon Interactions at a Rough Metal Surface, Physical Review B, 4 (1971) 4129-4138.

[190] D. Sarid, W.A. Challener, Modern Introduction to Surface Plasmons: Theory, Mathematica Modeling, and Applications, Cambridge University Press2010.

[191] R.-L. Chern, X.-X. Liu, C.-C. Chang, Particle plasmons of metal nanospheres: Application of multiple scattering approach, Physical Review E, 76 (2007) 016609.

[192] W.L. Barnes, Particle plasmons: Why shape matters, American Journal of Physics, 84 (2016) 593-601.

[193] X. Fan, W. Zheng, D.J. Singh, Light scattering and surface plasmons on small spherical particles, Light: Science &Amp; Applications, 3 (2014) e179.

[194] R. Ameling, H. Giessen, Cavity Plasmonics: Large Normal Mode Splitting of Electric and Magnetic Particle Plasmons Induced by a Photonic Microcavity, Nano Letters, 10 (2010) 4394-4398.

[195] D. Chen, J. Zhou, M. Rippa, L. Petti, Structure-dependent localized surface plasmon resonance characteristics and surface enhanced Raman scattering performances of quasi-periodic nanoarrays: Measurements and analysis, Journal of Applied Physics, 118 (2015) 163101.

[196] Z. Enming, J. Peipei, E.-H. Heike, L. Hanyang, H. Peng, L. Diyou, L. Hanyang, Y. Xinghua, L. Lu, G. Chunying, Localized surface plasmon resonance sensing structure based on gold nanohole array on beveled fiber edge, Nanotechnology, 28 (2017) 435504.

[197] P.B. Johnson, R.W. Christy, Optical Constants of the Noble Metals, Physical Review B, 6 (1972) 4370-4379.

[198] S. Supansomboon, A. Maaroof, M.B. Cortie, “Purple glory”: The optical properties and technology of AuAl2 coatings, Gold Bulletin, 41 (2008) 296-304.

[199] F.J. García de Abajo, Optical excitations in electron microscopy, Reviews of Modern Physics, 82 (2010) 209-275.

[200] F.J. Garcıía de Abajo, Multiple Excitation of Confined Graphene Plasmons by Single Free Electrons, ACS Nano, 7 (2013) 11409-11419.

[201] A.L. Koh, K. Bao, I. Khan, W.E. Smith, G. Kothleitner, P. Nordlander, S.A. Maier, D.W. McComb, Electron Energy-Loss Spectroscopy (EELS) of Surface Plasmons in Single Silver Nanoparticles and Dimers: Influence of Beam Damage and Mapping of Dark Modes, ACS Nano, 3 (2009) 3015-3022.

[202] E.L. Wood, J.R. Sambles, N.P. Cotter, S.C. Kitson, Diffraction Grating Characterization Using Multiple-wavelength Excitation of Surface Plasmon Polaritons, Journal of Modern Optics, 42 (1995) 1343-1349.

[203] H. Raether, Surface plasmons on smooth and rough surfaces and on gratings, Springer, Berlin, 1988.

[204] H.J. Lezec, A. Degiron, E. Devaux, R.A. Linke, L. Martin-Moreno, F.J. Garcia-Vidal, T.W. Ebbesen, Beaming Light from a Subwavelength Aperture, Science, 297 (2002) 820.

[205] E. Kretschmann, H. Raether, Notizen: Radiative Decay of Non Radiative Surface Plasmons Excited by Light, Zeitschrift für Naturforschung A, 1968, pp. 2135.

[206] A. Otto, Excitation of nonradiative surface plasma waves in silver by the method of frustrated total reflection, Zeitschrift für Physik A Hadrons and nuclei, 216 (1968) 398-410.

[207] L. Novotny, Principles of nano-optics, 2nd ed. ed., Cambridge University Press, Cambridge, 2012.

[208] E.T. Arakawa, M.W. Williams, R.N. Hamm, R.H. Ritchie, Effect of Damping on Surface Plasmon Dispersion, Physical Review Letters, 31 (1973) 1127-1129.

[209] M. Mayy, G. Zhu, A.D. Webb, H. Ferguson, T. Norris, V.A. Podolskiy, M.A. Noginov, Toward parametric amplification in plasmonic systems: Second harmonic generation enhanced by surface plasmon polaritons, Opt. Express, 22 (2014) 7773-7782.

[210] S.A. Maier, Plasmonics : fundamentals and applications, Springer, New York, 2007.

[211] P. Ferguson, R.F. Wallis, M. Belakhovsky, J.P. Jadot, J. Tomkinson, Surface plasma waves in silver and gold, Surface Science, 76 (1978) 483-498.

[212] J.J. Burke, G.I. Stegeman, T. Tamir, Surface-polariton-like waves guided by thin, lossy metal films, Physical Review B, 33 (1986) 5186-5201.

[213] T. Wakamatsu, K. Saito, Interpretation of attenuated-total-reflection dips observed in surface plasmon resonance, J. Opt. Soc. Am. B, 24 (2007) 2307-2313.

[214] L. Wendler, R. Haupt, An Improved Virtual Mode Theory of ATR Experiments on Surface Polaritons. Application to Long-Range Surface Plasmon-Polaritons in Asymmetric Layer Structures, physica status solidi (b), 143 (1987) 131-148.

[215] D. Brissinger, L. Salomon, F. De Fornel, Unguided plasmon-mode resonance in optically excited thin film: exact modal description of Kretschmann–Raether experiment, J. Opt. Soc. Am. B, 30 (2013) 333-337.

[216] S.A. Maier, Plasmonics: Fundamentals and Applications, Springer2007.

[217] Tru, A. gler, Optical Properties of Metallic Nanoparticles : Basic Principles and Simulation, Springer, Cham, 2016.

[218] M. Li, S.K. Cushing, N. Wu, Plasmon-enhanced optical sensors: a review, Analyst, 140 (2015) 386-406.

[219] S.K. Ghosh, T. Pal, Interparticle Coupling Effect on the Surface Plasmon Resonance of Gold Nanoparticles: From Theory to Applications, Chemical Reviews, 107 (2007) 4797-4862.

[220] C.F. Bohren, Absorption and scattering of light by small particles, Wiley-Interscience, New York, 1983.

[221] CRC Handbook of Chemistry and Physics, 84th Edition Edited by David R. Lide (National Institute of Standards and Technology). CRC Press LLC: Boca Raton. 2003. 2616 pp. $139.95. ISBN 0-8493-0484-9, Journal of the American Chemical Society, 126 (2004) 1586-1586.

[222] D.J. Griffiths, Introduction to electrodynamics, 4th ed. ed., Pearson, Boston, 2013.

Chapter 2 Launching low energy surface plasmon resonances (SPRs) in the purple gold ($AuAl_2$) intermetallic

This chapter will explore the surface plasmons (SPs) in the intermetallic compound known as purple gold ($AuAl_2$). Intermetallic compounds are phases formed by two or more metallic elements in definite stoichiometry. Their properties (e.g. bonding, crystal structure, electrical and optical properties etc.) can be quite dissimilar to their constituents. This is exemplified by the gold-aluminum (Au-Al) system. If one were to anneal a bulk junction between Au and Al, one would obtain all five intermetallic phases with different colors that are formed simultaneously as shown in Figure 2.1. These are Au_4Al (tan), Au_5Al_2 (tan), Au_2Al (metallic grey), AuAl (white) and $AuAl_2$ (purple), respectively.

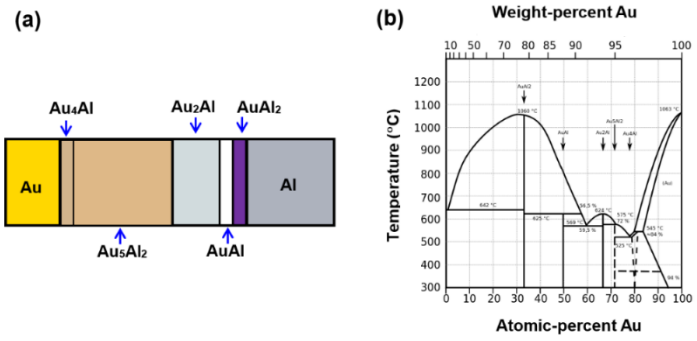

Figure 2.1: The formation of all five intermetallic compounds from a bulk junction between gold (Au) and aluminum (Al). (a) Schematic diagram of all five phases and (b) the phase diagram of the Au-Al system. The right image (or Figure 2.1 (b)) has been modified and obtained by Cepheiden from the Wikipedia website (https://en.wikipedia.org/wiki/Gold-aluminium_intermetallic#/media/File:Phasendiagramm_Gold-Aluminium.svg). It was made available by Cepheiden which is licensed under a CC BY-SA 3.0. It is attributed to "Cepheiden".

Intermetallics differ from alloys even though both are formed by two or more metallic elements. In particular, alloys are random mixtures of metals, while intermetallics possess the long-range order of a multicomponent crystalline compound. This order gives the intermetallic distinct properties from their parent metals [1].

This chapter is based on a manuscript that has been submitted for publication. Some theoretical calculations have been elaborated for clarity and ease of understanding.

2.1 Introduction

2.1.1 The intermetallic compound purple gold

Of the five intermetallic compounds between gold (Au) and aluminum (Al) [2], the most aluminum-rich is $AuAl_2$, or purple gold. It is made of 79% by weight of Au and 21% by weight of Al. As this name suggests, $AuAl_2$ is distinguished by an intense and unusual purple color, first described by W. C. Robert-Austen in 1891 as amethyst gold [3]. As it meets the definition of 18 carat gold, its main use today is as a decorative element in gold jewelry [4-6]. In a negative sense, it is also important technologically as it occurs in gold wirebonds onto aluminum contact pads in integrated circuits, where its presence signifies a contact of poor reliability, which has earned the compound the moniker “purple plague,” as it is associated with microcircuit failure during wire bonding. For this reason, there is an extensive literature studying the formation of intermetallics at the interface between Au and Al [2, 7-11]. Despite its past notoriety, purple gold has been employed in a number of applications beyond the jewelry, such as a transparent electrode [12] and a selective solar absorber [13].

2.1.2 Color perception and the interband transition

Before discussing the mechanism contributing to purple color in purple gold, the color perception of human will be discussed using bulk gold and silver (Ag) as examples. First, people perceive color either as (i) a consequence of the interactions between white light and an object or because (ii) the object itself emits a non-white light spectrum. White light is composed of the entire spectrum (different colors) of visible light. These colors are red, orange, yellow, green, blue, indigo, and violet as seen from the separated color from a prism or in a rainbow. Alternatively, white light may be interpreted as a combination of three primary colors (red, green, and blue) of light with equal intensity.

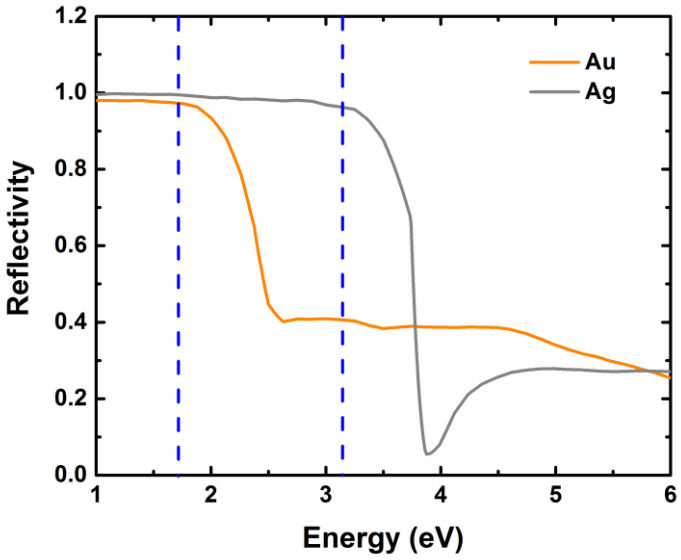

Figure 2.2: A plot of normal reflectivity of bulk Au and Ag vs energy. The reflectivity R is calculated using Fresnel's equations at zero angle of incidence ($\theta_i = 0$). The energy range between dashed blue lines represent the range of white light or visible spectrum. The refractive indices of Au and Ag are obtained from Johnson and Christy [14].

Consider a graph of normal reflectance versus energy in bulk Au and Ag demonstrated by blue dashed lines in the Figure 2.2. The range of energy of visible spectrum light is from around 1.7 to 3.1 eV. For Au, the reflected intensity drops at the blue end of the spectrum under white light illumination; that is, red and green light together appearing as a yellow color will be reflected from bulk Au more effectively than blue light.

Therefore, the color of Au appears as yellow. For Ag, the reflectance is high across the entire visible spectrum, which results in a pure metallic white color.

The mechanism that accounts for the formation of color of pure Au and Ag have been long known and can be explained with band theory. In this framework, the origin of the color formation is the so-called *interband transition*, which constitutes the excitation of electrons from an occupied band to an unoccupied band. The interband transitions correspond to the absorption peaks in the imaginary part of a dielectric function or a relative permittivity ϵ_I, which is depicted in Figure 2.3 for the case of bulk Au and Ag.

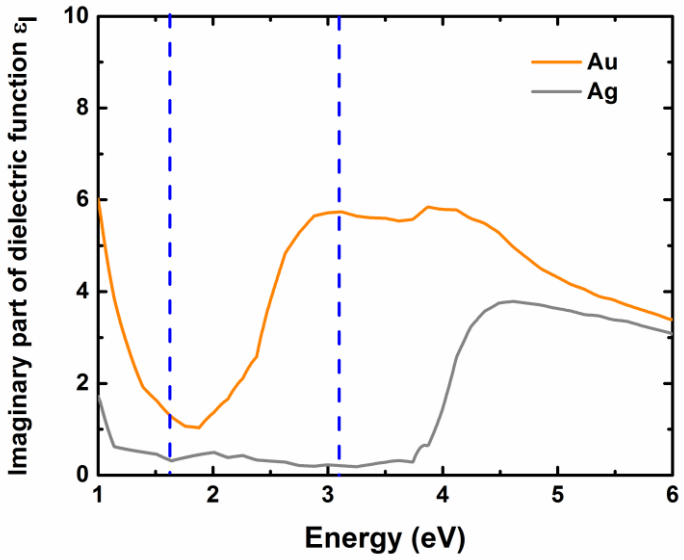

Figure 2.3: The dependence of the imaginary part of the complex dielectric function ϵ_I as a function of energy E of bulk Au and Ag. Both complex dielectric functions $\epsilon = \epsilon_R + i\epsilon_I$ of Au and Ag are obtained from Johnson and Christy [14].

The electron configuration of Au is [Xe] $4f^{14}$ $5d^{10}$ $6s^1$, while that of Ag is [Kr] $4d^{10}$ $5s^1$, which means that Au and Ag have a similar electronic structure in that they have one free conduction electron per atom. As a consequence, both elements have a same mechanism for the interband transition.

In Au (the orange line), the peak of $\epsilon_{I(Au)}$ occurs around 2.5 eV (blue-green spectrum), which corresponds to the onset of the interband transitions from the 5d band to the 6sp hybrid band, giving rise to an additional absorption process. The observed color of Au is yellow, as the corresponding wavelengths (~2.5 eV) are absorbed, thus reflecting the rest of the visible spectrum. For the case of Ag (the grey line), the same

mechanism applies since Ag has a similar electronic structure as Au. However, the onset of the interband transition occurs around 4.0 eV, which lies in the ultraviolet. All of the visible spectrum is reflected, causing the characteristic white metallic color of silver. Knowing the mechanism that explains the formation of color in bulk Au and Ag, the next section will elaborate the case of purple gold.

2.1.3 Optical properties of purple gold

It was originally assumed that $AuAl_2$ also derives its color from an interband absorption [15, 16] akin to how copper and gold achieve their colors, although several authors have argued that the 5d band in this compound lies too far below the Fermi level for this to be plausible [17-19]. A recent calculation of the $AuAl_2$ dielectric function ε_m suggested that low energy bulk plasmons play a pivotal role in the origin of the purple color [20, 21]. The existence of bulk plasmons in purple gold was also experimentally made plausible by the same authors through electron energy-loss spectroscopy (EELS) [21].

To elucidate the argument above, one need to interpret the frequency dependence of the complex dielectric function[2] $\epsilon(\omega) = \epsilon_R + i\epsilon_I$ of purple gold ($AuAl_2$) as well as that of gold (Au) for comparison. Note that the rising zero crossing of the real part of the dielectric function ϵ_R is characteristic of bulk plasmons, while a peak in the imaginary part ϵ_I suggests the dominance of interband transitions. Figure 2.4 depicts the experimental dielectric functions of Au and $AuAl_2$.

[2] The term dielectric function is ambiguous because some authors use this term for the absolute permittivity ϵ which has the unit F m^{-1}. Here, the dielectric function represents the relative permittivity ϵ_r defined as the ratio between the absolute permittivity ϵ and the permittivity of free space $\epsilon_0 = 8.854 \times 10^{-12}\ F\ m^{-1}$.

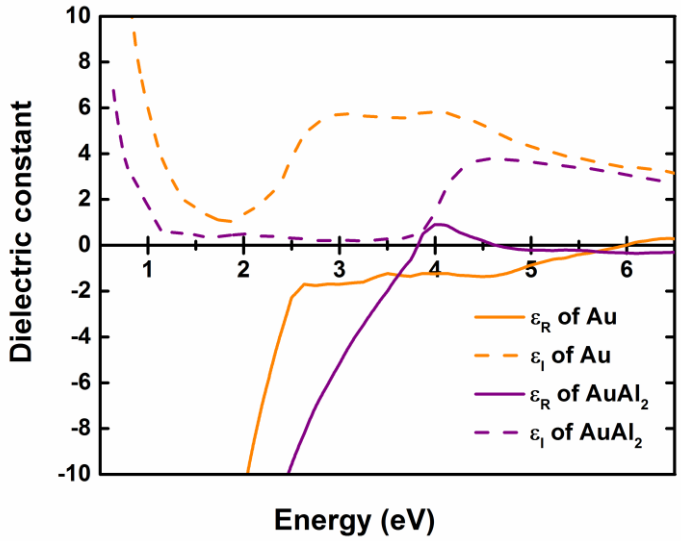

Figure 2.4: Experimental dielectric functions $\epsilon = \epsilon_R + i\epsilon_I$ of Au and $AuAl_2$. The solid curves are the real part ϵ_R, whereas the dash curves represent the imaginary part ϵ_I. The experimental data of Au is from Johnson and Christy [14], while that of $AuAl_2$ were deduced from normal reflection analysis [22].

For the case of Au, the zero crossing of ϵ_R occurs at much higher energy (~6 eV), which is outside the visible spectrum (~1.7 - 3.1 eV). The peak in ϵ_I (~2.5 eV), however, lies inside that region. Therefore, the interband transition (a peak in ϵ_I) plays a significant role in the yellow color of gold, while bulk plasmons (a vanishing of ϵ_R) come into play at higher energy.

For the case of $AuAl_2$, the situation is the reverse of that of pure Au. The significant absorption peak in ϵ_I (~4.3 eV), occurs at the higher energy, which is outside the visible spectrum. However, the zero crossing of ϵ_R occurs in visible region. Therefore, the presence of bulk plasmon instead plays an important role in the purple color of $AuAl_2$, while the interband transition plays a role in UV region.

2.1.4 Evidence of low energy plasmons

One of the possible ways to excite a plasmon is to launch an electron beam through a thin film specimen and measure the energy-loss distribution of reflected or transmitted electron owing to inelastic scattering.

The presence of plasmons will show as peaks in EELS spectra [21, 23-25]. Keast *et al*. observed a peak around 2 eV, indicating low-energy plasmons as predicted from the reflection spectrum (a zero crossing of $\epsilon_R \sim 2$ eV). A calculated spectrum of EELS can be obtained from the energy-loss function $\Im(-1/\epsilon)$ and is in agreement with experimental spectra [21].

2.1.5 Objectives

From the previous section 2.1.4, the existence of bulk plasmons in the $AuAl_2$ intermetallic are consistent with EELS results. However, there is still no direct experimental evidence for the presence of surface plasmons and localized surface plasmon resonances in $AuAl_2$ compounds as the EELS peak could conceivably have non-plasmon origins. Accordingly, the objective of this work is to verify whether the strong purple color of $AuAl_2$ is due to a low energy surface plasmon even though the prevailing assumption has been that it is due only to interband transitions.

To accomplish this, one needs to prove the existence surface plasmon resonances in $AuAl_2$ thin films. Moreover, surface plasmon polariton dispersion relations should be derived both theoretically and experimentally.

In this chapter, we confirm the plasmon assumptions by demonstrating that surface plasmons (SPs) can be launched into thin $AuAl_2$ films just as in pure gold films. We extract a dispersion relation for the surface plasmon in purple gold and compare it to theory. We show that although SPs in $AuAl_2$ are quite lossy, they still lend themselves to surface plasmon resonance (SPR) sensing. Finally, we discuss potential plasmonics applications of $AuAl_2$, which would be particularly promising in purple gold nanoparticles ($AuAl_2$ NPs).

2.2 $AuAl_2$ sample fabrication

$AuAl_2$ can be fabricated in several different ways depending on whether bulk or thin film samples are desired.

To investigate the presence and properties of a surface plasmon, one need to fabricate thin film specimen. However, the procedure for producing thin film sample is different from that of its bulk counterpart.

2.2.1 Distinctions between bulk and thin film forms

$AuAl_2$ in bulk form can be prepared by annealing a bulk mixture of Au and Al. However, the final product will not be pure $AuAl_2$; there are also four other Au-Al phases: Au_4Al, Au_5Al_2, Au_2Al and AuAl. In other words, once a bulk couple of Au and Al are heated to a high enough temperature and for a long adequate time, one metallic species will interdiffuse to the other. As a result, they will form all five intermetallic compounds are formed as can be expected from the equilibrium phase diagram of Au-Al system (see Figure 2.1) [8].

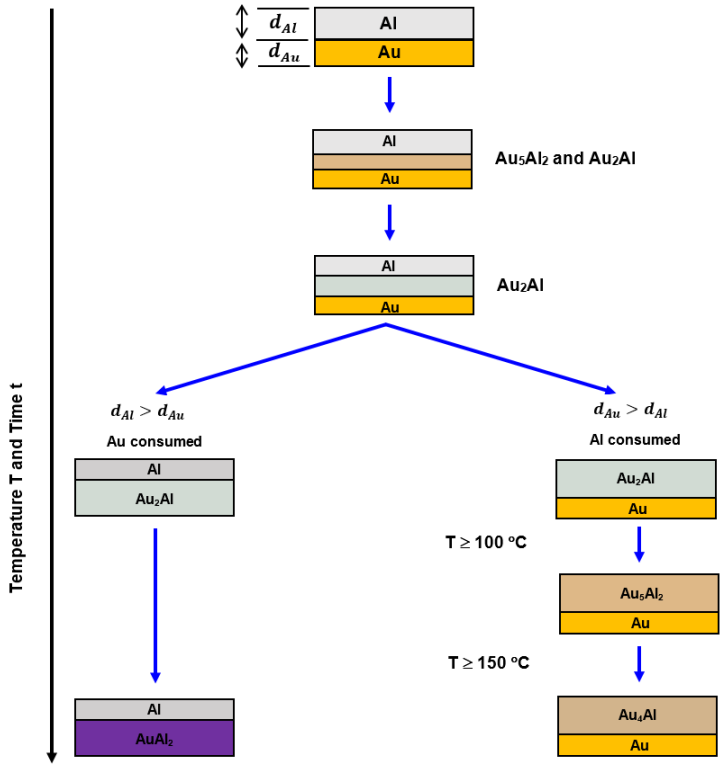

Figure 2.5: Schematic diagram for Au-Al compound formation in the thin-film form. The process is different from that of bulk formation in Figure 2.1.

$AuAl_2$ thin films, on the other hand, cannot be obtained simply by scaling the thickness down from a bulk-diffusion couple and expecting the formation of all five intermetallic phases after heat treatment. Thin film reaction results in only one or two phases due to the single compound formation sequence as illustrated in Figure 2.5. Therefore, the desired intermetallic compound or the final phase can be achieved by controlling the amount of materials available in the initial reaction. For example, the $AuAl_2$ thin film is the end phase of the Al-rich ($d_{Al} > d_{Au}$) bimetallic Au-Al film annealed at temperature more than 150 °C for a sufficient time.

2.2.2 $AuAl_2$ thin film fabrication

A significant literature exists to guide the fabrication of this $AuAl_2$ films, showing that the just described method is prone to the production of undesired compounds, such as AuAl or Al, along with $AuAl_2$. For instance, G.Majni et al. made a binary Au-Al thin film of thickness 150 and 140 nm, respectively and then annealed it at temperature around 247 °C for 5 minutes. The final product appeared with a purple color; nonetheless, $^4He^+$ MeV backscattering spectra revealed another Au-Al compound–AuAl, underneath the $AuAl_2$ film [26], showing the importance of correctly chosen thickness ratios of Au and Al, if we are to obtain a pure $AuAl_2$ film. More specifically, the following parameters must be chosen appropriately:

(i) The ratio of Al and Au films thickness d_{Al}/d_{Au};

(ii) The annealing temperature;

(iii) The annealing time;

(iv) The annealing environment.

2.2.3 Color of $AuAl_2$ thin film from various conditions

To find a working procedure for producing a pure and uniform $AuAl_2$ film, the deposition and annealing conditions were adjusted so that the most intense purple color appeared as observed by the naked eye.

Table 2.1: Characteristic color, shown on both sides, of 50-nm thick Au-Al thin films with different (i) thickness ratios of Al and Au films (d_{Al}/d_{Au}) and (ii) annealing temperature.

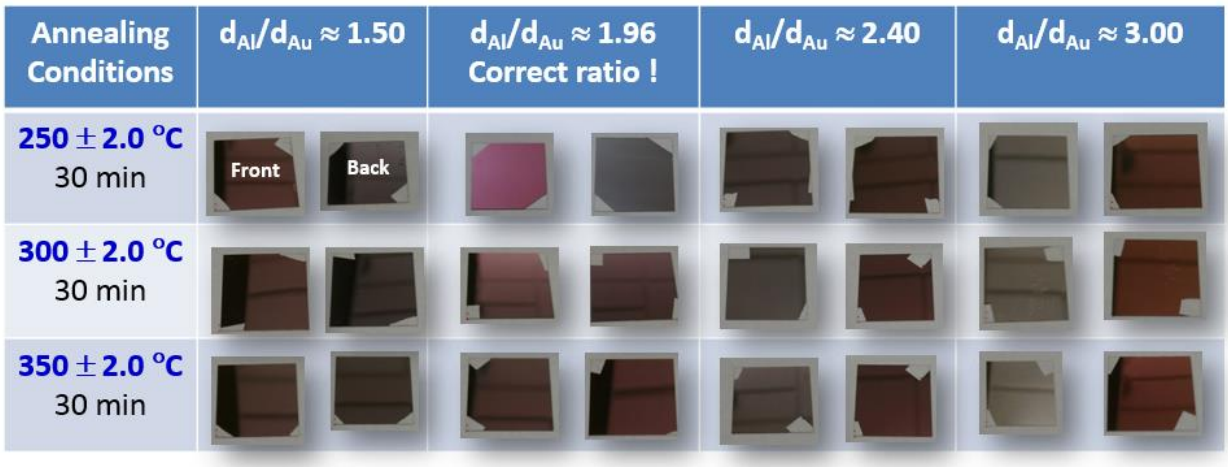

Table 2.1 illustrates the color appearance of a series of bilayer Au-Al thin film, from both the front and back sides. The thickness ratio of Al and Au d_{Al}/d_{Au} and the annealing temperature were varied, while the total film thickness was kept constant at 50 nm, and the annealing time was maintained at 30 minutes for all cases. All other parameters, e.g. base pressure of the thin film deposition and nearly-free-oxygen environment during heat treatment, were also kept constant.

Firstly, if one looks at the first column where the thickness ratio d_{Al}/d_{Au} is approximately 1.50, the front side of each sample exhibits purple color, but the back does not, which implies that those specimens contains Au-Al intermetallic other than purple gold $AuAl_2$, most likely AuAl. As a result, this thickness ratio is not appropriate for making good $AuAl_2$ thin film at any annealing temperature.

Secondly, consider the extreme case where the ratio d_{Al}/d_{Au} is about 3.00, as shown in the last column. Here, the back side instead shows intense purple color, while the front appears a metallic-gray color, which indicates an excess of aluminum after annealing, as can be expected from Figure 2.5.

Thirdly, a similar behavior and its explanation also materializes for the case of $d_{Al}/d_{Au} \approx 2.40$ in the third column.

Finally, purple color characteristic of $AuAl_2$ appears on both sides of samples with thickness ratio of $d_{Al}/d_{Au} \approx 1.96$, where those samples annealed at temperature more than 300 °C revealed more intense purple color than the sample heated at 250 °C. However, any difference in color between the two specimens annealed at 300 °C and 350 °C is not evident to the naked eye.

Note that the ratio 1.96 is theoretically the correct thickness ratio between Al and Au for formation of the $AuAl_2$ compound, which can be proved as follows:

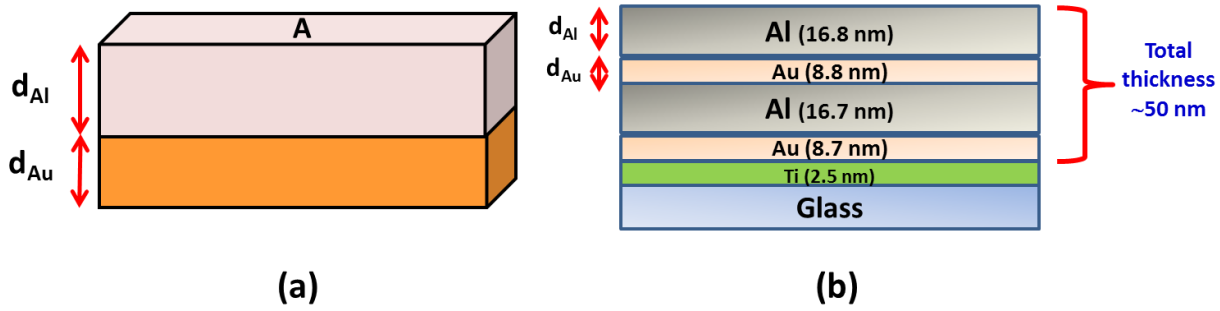

Figure 2.6: Schematic picture of a binary Au-Al thin film. (a) A single-bilayer Au-Al film where the Au film is beneath Al film. We need $d_{Al}/d_{Au} \approx 1.96$ to obtain the $AuAl_2$ intermetallic. (b) A 50-nm double bilayer Au-Al film with layer thicknesses chosen to produce a $AuAl_2$ thin film.

Consider a binary Au-Al thin film where an aluminum film is on the top of a gold film. Each layer has the same surface area A but different thickness d_{Al} and d_{Au} for aluminum and gold, respectively (See Figure 2.6 (a)). Owing to the same surface area A and constant term N_A of both films, the thickness ratio is given by

$$\frac{d_{Al}}{d_{Au}} = \left(\frac{N_{Al}}{N_{Au}}\right)\left(\frac{M_{Al}}{M_{Au}}\right)\left(\frac{\rho_{Au}}{\rho_{Al}}\right) = \left(\frac{2}{1}\right)\left(\frac{26.98\ u}{196.97\ u}\right)\left(\frac{19.30\ g\ cm^{-3}}{2.70\ g\ cm^{-3}}\right) \approx 1.96, \quad (2.2.15)$$

since the number ratio of aluminum to gold atoms $N_{Al}N_{Au}$ should be 2:1 to obtain the $AuAl_2$ intermetallic. In sum, according to Table 2.1, to fabricate purple gold ($AuAl_2$) thin films, we need to make a double-bilayer Au-Al thin film with thickness ratio d_{Al}/d_{Au} around 1.96 and anneal it at a temperature of at least 300 °C for at least 30 minutes. The reason for depositing two successive bilayers rather than one is to ensure that the resulting film consists of uniform $AuAl_2$ without inclusions of other intermetallics.

2.2.4 $AuAl_2$ thin film procedures

In-house fabricated $AuAl_2$ 30 nm thick film was deposited onto two kinds of substrates: (i) 2.5 × 2.5 cm^2 glass slides, and (ii) equilateral prisms made of NS-F11 glass. The former is for characterization of the $AuAl_2$ compound with non-optical methods (e.g. XPS, SIMS, etc.), while the latter is for Kretschmann excitation of SPPs. In that case, metal was deposited only on half of the hypotenuse of the prism, leaving other half uncoated, so it can be used for total internal reflection measurements. The pure gold films were deposited in the same configuration, although just a single 30 nm film was deposited at once with no annealing required.

The glass slides were precleaned by submersion in freshly-prepared aqua regia–a 1:3 V/V mixture of conc. HNO_3:HCl–for 20 minutes, then rinsing with copious amounts of nanopure water 3 times, and drying with a stream of dry nitrogen (N_2) gas. The surface of the equilateral prisms was however used without cleaning as they were clean as received. After cleaning, the substrates were immediately loaded into an electron beam (e-beam) evaporator chamber and pumped down to high vacuum for thin film deposition. Once the pressure had reached 7.0×10^{-7} Torr, the system was flushed with N_2 gas, pumped down again, and five sequential layers were deposited as follows: (i) 2.6 nm Ti, (ii) 5.2 nm Au, (iii) 10.9 nm Al, (iv) 5.3 nm Au,

(v) 10.1 nm Al. The Ti film was included to obtain good adhesion between the metal film and the glass substrate. This stack has a 1.96:1 ratio of Al and Au as required for a $AuAl_2$ film. After thin film deposition, the substrates were forthwith annealed at 300 °C for 30 minutes under nearly oxygen- and water-free conditions in a glove box. A change of color from grey (attributed to the Al film at the top of the stack) to purple was clearly noticeable, indicating the formation of $AuAl_2$. This purple color does not change significantly over the course of several months at least. This is because despite the high Al content, $AuAl_2$ is highly resistant to oxidation [27].

2.2.5 $AuAl_2$ thin film verification

At this stage, the color of the resulting film was used as a guide to whether the compound is $AuAl_2$ or not. If the film appeared purple, it was assumed to consist of $AuAl_2$. Although we did not perform them here, more quantitative methods for characterizing the film may be performed in the future. I will note two such methods here. The first method is to determine the atomic ratio of Au and Al, which can be compared to that of $AuAl_2$, i.e., Al:Au = 2. This can be attained by secondary ion mass spectrometry (SIMS). The second approach is to compare X-Ray diffraction patterns from the films to that of $AuAl_2$ [22, 28].

2.3 Excitation of SPs by the Kretschmann configuration

Before attempting to launch SPs in $AuAl_2$, we use the Kretschmann configuration to verify that we can observe SPs in a regular Au film.

2.3.1 SPRs in 30-nm thick Au films at a single wavelength

The schematic diagram depicted in Figure 2.7 shows the setup for exciting SPPs in a Au thin film. The light source in this case is a HeNe laser, which emits a monochromatic, coherent, and collimated light of 633 nm wavelength.

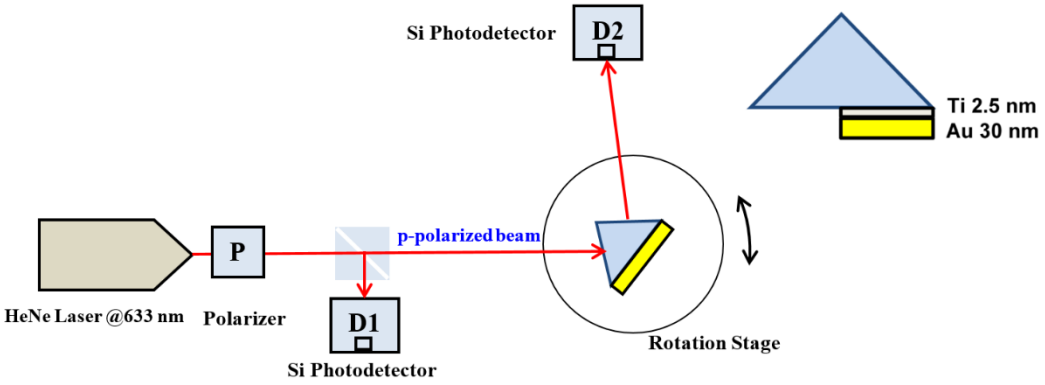

Figure 2.7: Schematic diagram of our SPR setup for launching SPPs in Au film using a HeNe laser as a light source. The inset shows the prism has Au film deposited on only the half face hypotenuse and a 2.5-nm Ti film with adhesion layer to ensure the metal sticks to the glass.

Since this laser outputs randomly polarized light, a linear polarizer P was added so that a well-defined polarization state was obtained. The beam was then p-polarized after passing through a polarizing beam splitter cube, while deflected s-polarized residue beam was recorded by a Si photodetector D1, which was connected to a voltmeter for reading the voltage. The transmitted p-polarized light excited SPPs by illuminating the Au film surface coated on the half face of the N-SF11 equilateral prism as described in section 2.2.4 and shown here in the inset of Figure 2.7. A 2.5-nm Ti film was first deposited for better adhesion between a prism and Au film. The reflected light from the prism was collected by a Si photodetector D2 for reading the light intensity for each incident angle θ_i, which was varied by moving a rotational stage. Note that the Si photodetector D2 was moved every time when the incident angle changes to collect the reflected light at the highest intensity.

The angle θ_i' read from the rotational stage is not the actual incident angle θ_i onto the metal but can be transformed to the real incident angle using the geometry as shown in the inset of Figure 1.7 in Chapter 1, i.e.,

$$\theta_i = 60° - \arcsin\left(\frac{n_{air}}{n_p}\sin(\theta_i')\right). \quad (2.3.16)$$

Let S be a signal which is the ratio of the voltage read from D2 and D1, respectively. The relative reflectance R can then be calculated as a ratio of signal from the gold coated and uncoated sections at the prisms as:

$$R = \frac{S_{Au}}{S_{prism}} \text{ where } S = \frac{V_{D2}}{V_{D1}}. \quad (2.3.17)$$

A graph of the reflectance R as a function of the angle of incidence θ_i for the gold film is shown in Figure 2.8.

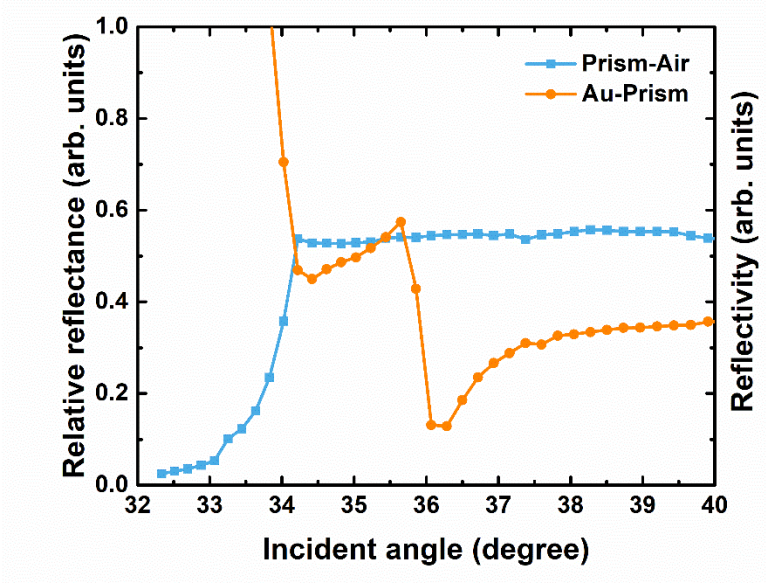

Figure 2.8: Experimental SPR reflectivity curve of a 30-nm thick film of Au at wavelength $\lambda = 633$ nm from a HeNe laser. The blue and orange curves represent the relative reflectance from the prism-air and Au-air interfaces, respectively. The dip in reflectivity in the red curve at 36.3° is a manifestation of SPP excitation.

The reflectance from the Au-prism interface (orange curve) exhibits the signature of SPRs in the Au film. The SPR manifests as a minimum in the reflectivity that occurs around 36.3° (or $\theta_{res,exp}$= 36.3°), which is

more than the critical angle ($\theta_{c,exp}$ = 34.2°) from the prism-air interface (blue curve), verifying that SPR occurs in the range of total internal reflection regime.

This experimental results show a good agreement with the theoretical results as already shown in Chapter 1 where $\theta_{res,theory}$ = 37.4° and $\theta_{c,theory}$ = = 34.2°. The difference between θ_{min} from theory and experiment may be attributed to (i) the actual thickness of Au film, which may not be exactly 30 nm, and (ii) the addition of Ti film to the experiment, which should have been taken into account in the theoretical calculation.

2.3.2 SPRs in 30-nm Au film probed by white light

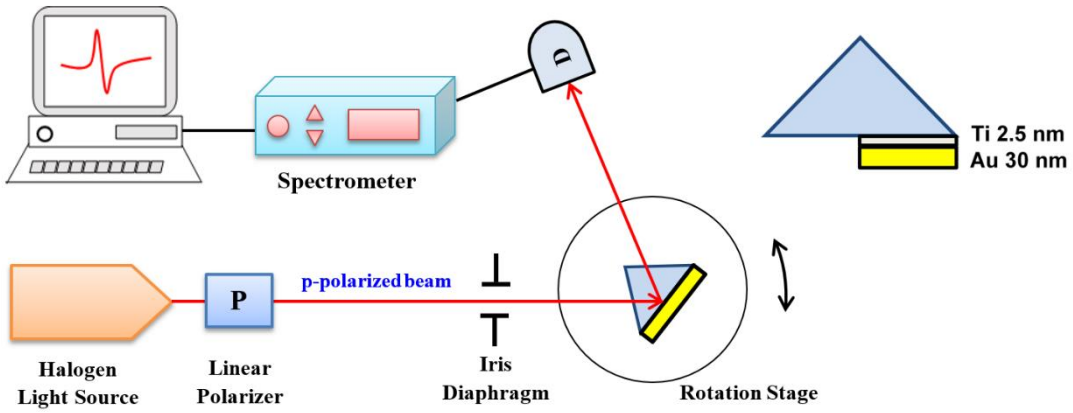

Figure 2.9: Schematic diagram for SPP excitation in 30-nm Au film. This setup was employed for a dispersion relation reconstruction.

The light source used in this setup was a halogen light source, which provides a broad and intense spectrum of white light ranging approximately from 400 to 1000 nm. As with the HeNe laser, the beam was p-polarized by the linear polarizer P. The light was then passed through an iris diaphragm to make the size of the beam smaller and more collimated, leading to a smaller spread in the angle of incidence. The prism and rotation stage was the same as in the HeNe measurement, but the light was collected by a fiber optic and

then sent to a spectrometer as shown in Figure 2.9. The results of this experiment are shown in Figure 2.10 as a graph between reflectance R and wavelength λ where each curve is associated with the reflection from Au film for a given angle of incidence θ_i.

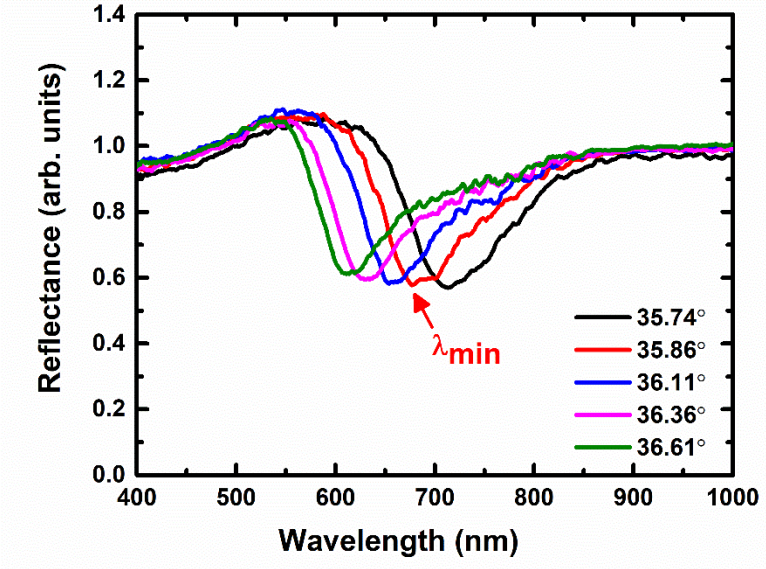

Figure 2.10: Reflectivity spectra from a 30-nm Au film in the Kretschmann configuration. Each curve represents the reflectance at a different incident angle as a broad spectrum light source was used for illumination.

Each curve in the graph manifests SPRs in Au thin film as a dip in reflectivity as outlined in Chapter 1. The wavelength at which the reflectivity is minimum (λ_{min}) corresponds to the wavelength where the SPR conditions are satisfied, and that therefore that can launch SPPs at a specific incident angle θ_i. We can see that λ_{min} blue shifts as the incident angle increases.

Having measured λ_{min} for each angle of incidence θ_i, a SPP dispersion relation for SPs in the Au film can be plotted by calculating the wave vector k and the energy $E = \hbar\omega = hc/\lambda_{min}$, where the wave vector k is given by

$$k = \frac{2\pi}{\lambda_{min}} n_p \sin\theta_i \,. \qquad (2.3.18)$$

2.3.3 SPRs in 30-nm $AuAl_2$ film by a Halogen light source

Having verified that we can launch SPPs in Au thin films and used this data to obtain the SPP dispersion relations in gold, the next step is to repeat these experiments in the case of purple gold. However, the setup in Figure 2.9 results in a very broad spectrum which makes it difficult to find the wavelength of minimum reflectivity λ_{min}. To work around this, the setup was modified as shown in Figure 2.11. This setup is similar to that of Figure 2.9, but the setup implements a technique known as *phase-polarization contrast*, which allowed us to observe the dip in reflectivity more clearly [29].

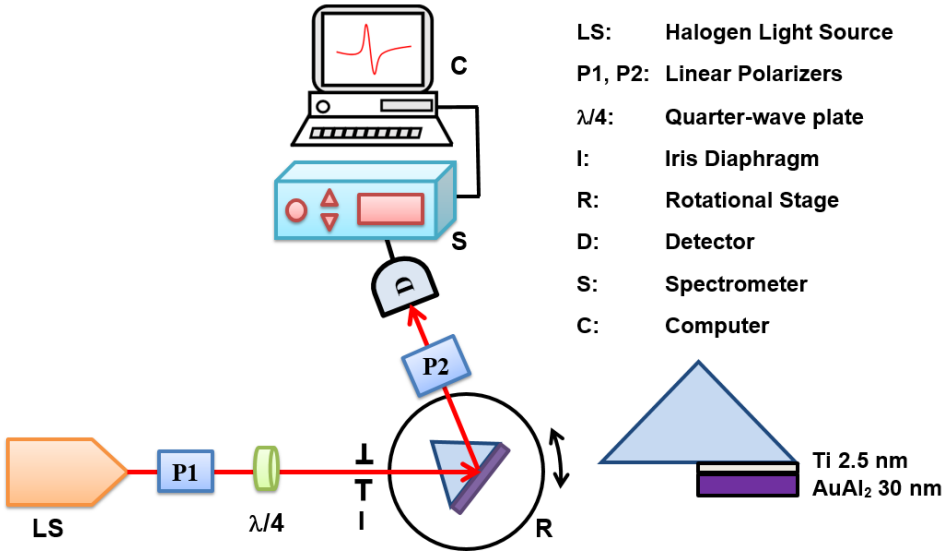

Figure 2.11: Experimental setup for launching SPPs in $AuAl_2$ thin films based on the Kretschmann configuration. To enhance the contrast in the SPRs intensity profile, a technique known as "phase-polarization contrast" was implemented in this experiment. This technique makes use of the rapid phase change that reflected p-polarized light undergoes when either the incident angle θ_i or energy E are tuned through the SP.

At the resonance angle of incidence θ_{res}, the reflected p-polarized component changes its intensity and phase while the s-component remains unchanged. Therefore, a quarter-wave plate is added to the setup to create a 90° phase difference between s- and p- polarizations, while a polarizer P2 will be added such that

the p-polarized light interferes destructively with the s-polarized light at the SP resonance, which causes a minimum in the observed reflectivity.

Apart from this modification, the experiment on $AuAl_2$ films was performed in the same way as on Au film. A graph of reflectivity vs wavelength for different angles of incidence was plotted in Figure 2.12.

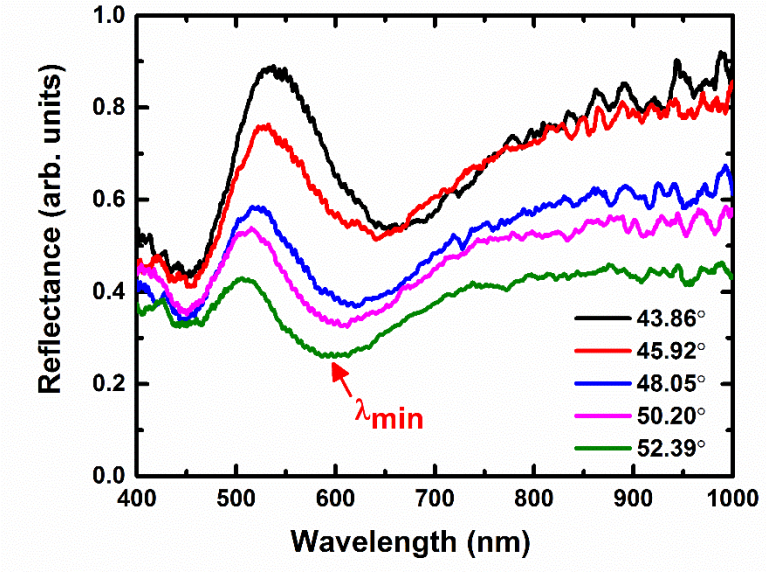

Figure 2.12: A plot of p-polarization reflectance (normalized by s-polarization reflectance) versus wavelength in 30 nm thick $AuAl_2$ film. Each curve corresponds to a different incident angle θ_i and yields an associated λ_{min} from which the surface plasmon dispersion relation can be found.

A broad and shallow minimum in the reflectivity spectrum was observed, but it was nevertheless sufficiently well-defined for the detectability of λ_{min}. Using the same calculation as in the Au case, a SPP dispersion relation can be constructed, which indicates that we have launched SPPs in a $AuAl_2$ thin film.

2.4 Surface plasmon polariton (SPP) dispersion relations

After obtaining a λ_{min} for each angle of incidence θ_i from the reflectivity spectra of Au and $AuAl_2$ film, an in-plane wave vector k and its corresponding photon energy E can be computed using (2.3.4) and (2.3.5). To determine if the experimental results support the theoretical predictions, the wave vector k and the

energy E were also calculated using (1.3.8) and (2.3.5) with literature values of relative permittivities of Au and $AuAl_2$ [14, 22]. The dispersion relations for both theoretical and experimental data are plotted in Figure 2.13, including the light line in air (or vacuum) given by $\omega = ck$.

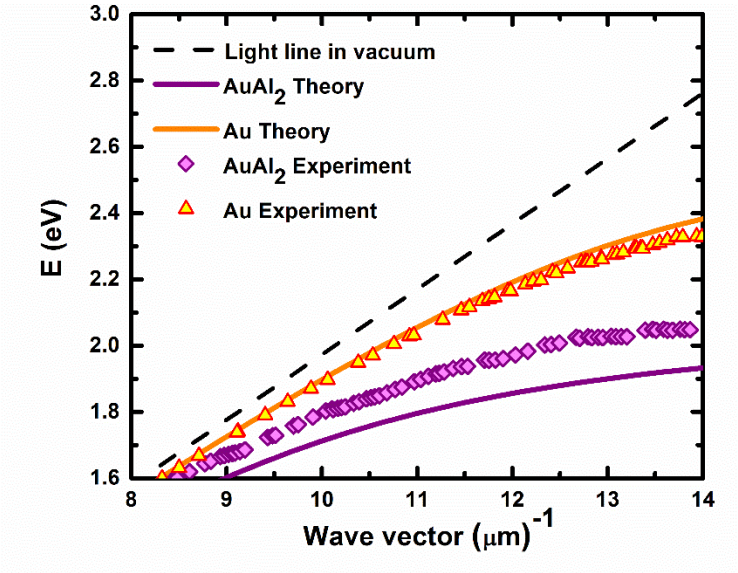

Figure 2.13: Theoretical (solid lines) and experimental (symbols) SPP dispersion relations of $AuAl_2$ (purple line and purple diamonds) and Au (orange line and yellow triangles) films. The dash black line represents the light line in vacuum (or air) given by $\omega = ck$.

The dispersion relations for both of Au and $AuAl_2$ are below the light line in vacuum as expected from theory and appear to approach a constant energy in the limit of large wave vectors. For Au, the experimental dispersion relation shows a good agreement with the theoretical one. For $AuAl_2$, the experiment and theory agree somewhat less well, but they still display a similar behavior at the large wave vector limit. More specifically, theory predicts that $\lim_{k\to\infty} E^{theory} = \lim_{k\to\infty} \hbar\omega_{SPP}^{theory} = 1.9\, eV$, while experiment anticipates that $\lim_{k\to\infty} E^{exp} = \lim_{k\to\infty} \hbar\omega_{SPP}^{exp} = 2.1\, eV$. There are several possibilities that cause the deviation of the experimental curve from the theoretical one. Firstly, it may result from the determination of λ_{min} from the reflectivity curve, which may not be exact and be somewhat offset due to the phase-polarization contrast technique. Secondly, there may be an excess of Au or Al in $AuAl_2$ film. Lastly, the experimental relative permittivity $\epsilon(\lambda)$ obtained from Supansomboon [22] may not be the same as the film obtained from this

experiment. Furrer et al. showed that the microstructure of a $AuAl_2$ film depends on the annealing temperature during the formation process. This results in a different shade of purple color, thereby causing in different relative permittivities in different $AuAl_2$ films [28].

2.5 Surface plasmon resonance (SPR) sensing

2.5.1 General background

Whenever the condition for SPR are met in a metal film, an evanescent electric field exists and decays exponentially from the outer metal surface into the environment. The decay length of this field is around 0.2-0.3 light wavelengths. As a result, any changes of refractive index in the close vicinity of the metal will have an impact on the SPR conditions and lead to a shift in the resonance angle. This is the principle of operation behind SPR biosensors, which are used for identifying or detecting small amount of ligands or proteins in a solution. SPR sensors can probe biomolecular interaction in real time, and without labeling. The sensors can therefore be of benefit in a number of fields, including chemistry, pharmacology, biology etc. [30-34].

In this section, we will demonstrate the existence of SPs in $AuAl_2$ using SPR sensing. In other words, we will study a change of reflected light intensity at a particular incident angle near the resonance angle when the refractive index of the close vicinity of $AuAl_2$ film changes. That angle is called the *sensitive angle* θ_{sen} because the reflectiviy has the highest slope at this wavelength, yielding the highest sensitivity to changes in refractive index. To illustrate this idea, consider Figure 2.14, which shows reflected light intensities under SPR from a Au film with thickness 50 nm in two different environments near the film: water ($n_w = 1.33$) and sucrose solution ($n_s = 1.34$). In practice, a convenient way to change the medium near the Au film is through a so-called *flow cell*, which is mounted onto the Au film.

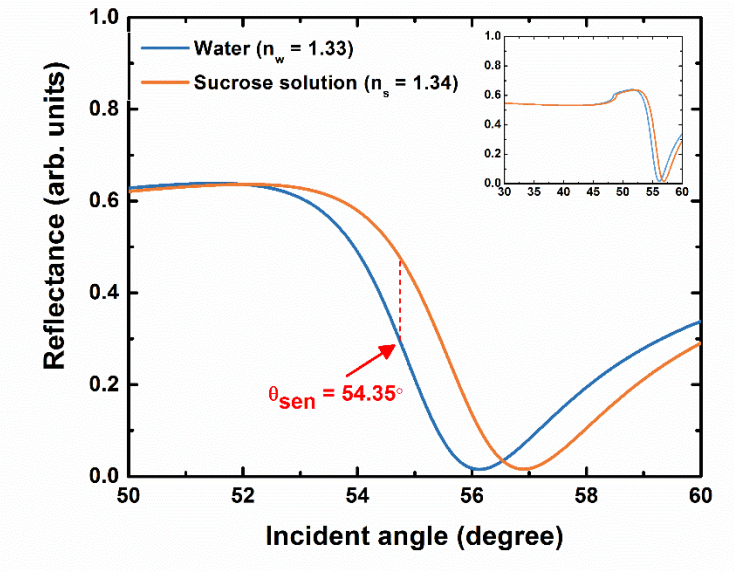

Figure 2.14: Theoretical SPR reflectivity curves for 50-nm Au film with two different solutions-water $n_w = 1.33$ (blue) and sucrose solution $n_s = 1.34$ (orange)-are in contact. The inset shows the same graphs but over a larger range of angles of incidence.

It is clear from the graph that the reflectivity curve as well as the resonance angle θ_{res} shift to the right (from 56.13° to 56.9°) when the refractive index of the close vicinity increases (from $n_w = 1.33$ to $n_s = 1.34$). Moreover, suppose one chose the sensitive angle θ_{sen} at 54.35°, the reflectivity would also increase (from 0.409 to 0.541). Therefore, small changes in the refractive index of the surrounding medium can be sensitively detected via a change in the reflected light intensity.

2.5.2 Experimental setup

To investigate the SPR sensing, a sensitive angle θ_{sen} must first be determined as we will measure reflectivity at that angle when the environment near the $AuAl_2$ film is changed. The experimental setup for finding θ_{sen} is illustrated in Figure 2.15. The light source used here was a 20-mW laser diode [LDM785, Thorlabs, Inc.], which emits a 785-nm-wavelength beam. It was chosen because we focused on the low-energy surface plasmon as shown in the dispersion relation in **Figure 2.13**.

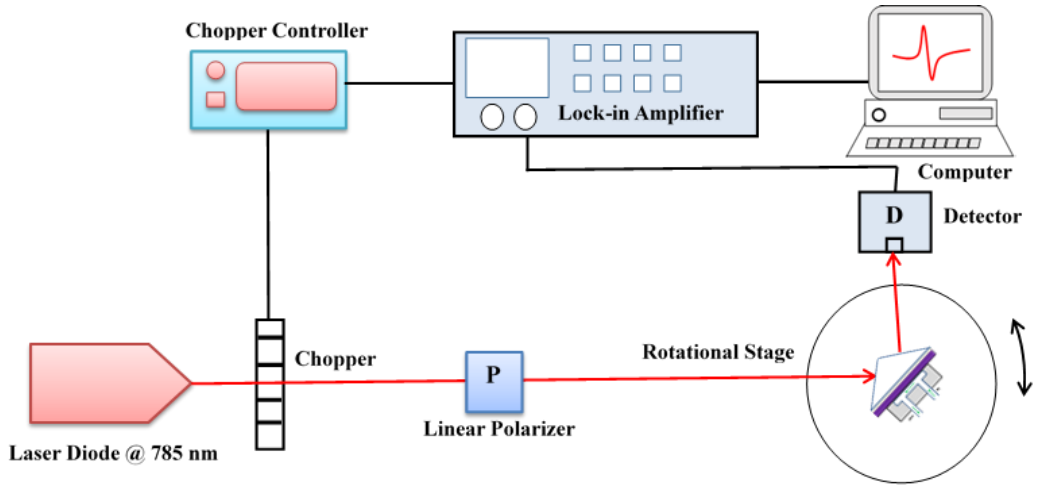

Figure 2.15: Schematic representation for the SPR sensor used to determine the sensitivity of SPPs in $AuAl_2$ and Au films to changes of refractive index of the surrounding medium.

As previously, p-polarized light was achieved when the beam passed through a linear polarizer P. This light was the incident upon a prism with a $AuAl_2$ film fabricated on its hypotenuse. The prism was mounted to a flow cell, where the reference solution was DI water. The reflected light was collected by a Si-photodetector [DET100A, Thorlabs, Inc.]. A chopper and a chopper controller [MC2000, Thorlabs, Inc.] were employed to make a periodic interruption of light at a certain frequency (f = 400 Hz). A lock-in amplifier [SR850, Stanford Research Institute] was then used to extract small signals otherwise obscured by noise. These small signals were then transmitted to a computer and analyzed in a LabVIEW™ program.

Reflectivity curves as a function of incident angle for ambient media of water and air are plotted in Figure 2.16. These graphs indicate the presence of SPRs in $AuAl_2$ in both sets of curves (either air with $n_a = 1.0000$ or DI water with $n_w = 1.3330$). The theoretical curves (Figure 2.16 (a)), generated from the Fresnel equations, demonstrate broad dips on both interfaces which should be compared to a sharper dip in Au films which has lower damping. Figure 2.16 (b) shows an experimental plot between reflectivity and angle of incidence, which can be varied by moving the rotational stage. Note that the last angle we were able to perform the experiment was at 60° due to the fact that we were working with the equilateral prism.

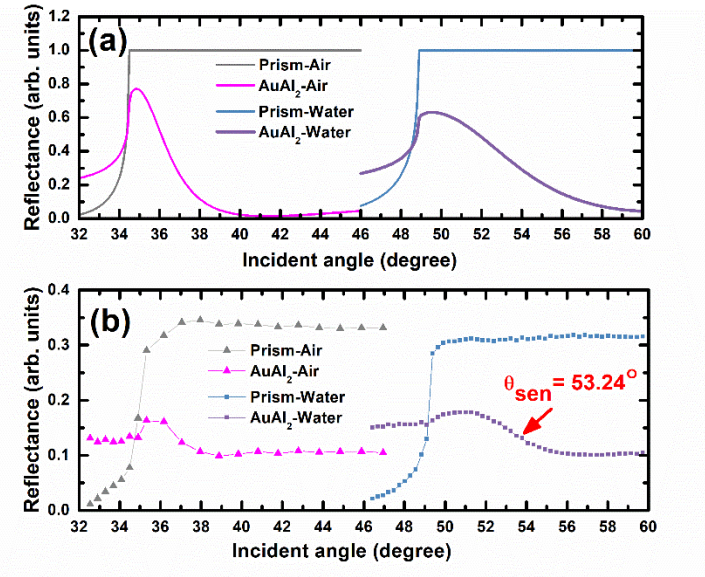

Figure 2.16: Calculated (a) and measured (b) angular reflectivity spectra of a system consisting of NSF11-$AuAl_2$-Air and NSF11-$AuAl_2$-Water. Curves for prism-air and prism-water interfaces are included to illustrate that the SPR curves lie within the total internal reflection regime. Note that the film thickness of $AuAl_2$ is 30 nm.

As liquids (e.g. sucrose solutions) would be introduced into a flow cell, a sensitive angle of $\theta_{sen} = 57.24°$ was selected from the $AuAl_2$-water-interface curve in which the purple-square graph indicates SPRs in $AuAl_2$. Note that plots for $AuAl_2$-air interface are shown for completeness and are not related to the detection experiment.

2.5.3 Refractive index sensitivity

To measure the signal change in our SPR sensor when the refractive indices of the surrounding medium changes, three different concentrations of sucrose solution were prepared (see Table 2.2). The signal was then collected at the sensitive angle in the same setup we used before (see Figure 2.15) where DI water ($n_w = 1.3330$) was used as the reference solution. Note that a 1°-Brix sucrose solution is 1 g of sucrose in 100 g of solution.

Table 2.2: Sucrose solutions used for the SPR sensing study in Au and $AuAl_2$ films.

Solutions (at 20°C)*	n	Δn	%ΔSignal (Au)	%ΔSignal ($AuAl_2$)
DI Water (reference)	1.3330	0	-	-
0.35°-Brix sucrose solution	1.3335	5×10^{-4}	5.89	0.47
0.70°-Brix sucrose solution	1.3340	10×10^{-4}	8.54	0.95
1.75°-Brix sucrose solution	1.3355	25×10^{-4}	26	2.43

* Methods of Analysis of the Association of Agricultural (now "Analytical") Chemist (A.O.A.C.) 1965

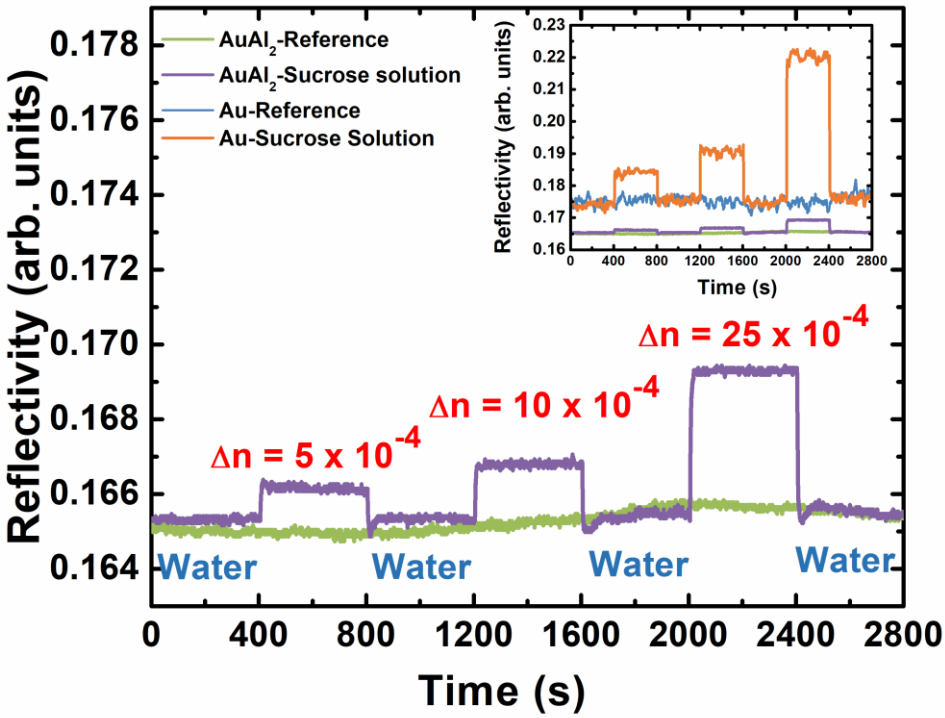

Figure 2.17: Time evolution of reflectivity when different solutions were injected into a SPR- $AuAl_2$ (purple) sensor at θ_{sen} = 53.24° and a SPR-Au (orange) sensor at θ_{sen} = 54.21° (shown in inset).

The change in SPR reflectivity as a function of time as the sucrose concentration was changed every 400 s is depicted in Figure 2.17. It is clear that the signal (purple line) increases when refractive index in close vicinity of $AuAl_2$ film increases. For example, at time t ~ 400 s the reflectivity changed from 0.165 to 0.166

when the 0.35°-Brix sucrose solution ($n_{s,0.35} = 1.3335$ or $\Delta n = n_s - n_w = n_{s,0.35} - n_w = 5 \times 10^{-4}$) was injected into the flow cell. The signal then returned to 0.165 again at t ~ 800 s, when the flow cell was flushed with DI water. Similar behaviors also occured when 0.70°-Brix ($n_{s,0.7} = 1.3340$) and 1.75°-Brix ($n_{s,1.75} = 1.3355$) sucrose solutions were introduced into and then removed from the flow cell.

Furthermore, the inset of Figure 2.17 also shows signal change of SPR sensor based on Au film for comparison. Note that the experimental setup for Au is the same as that of $AuAl_2$ except (i) the light source in the case of Au was a He-Ne laser ($\lambda = 633.2$ nm) and (ii) a polarizing beam splitter [Thorlabs] was inserted between the chopper and the linear polarizer (see Figure 2.15). According to Table 2.2 and Figure 2.16, one can see that SPR sensing in the $AuAl_2$ film is much less sensitive to changes in refractive index than in the Au film, as the reflectivity change is far larger in Au for a given refractive index change. Even if the refractive index sensitivity of a $AuAl_2$-SPR sensor is not excellent, this experiment verifies the existence of SPPs in $AuAl_2$ film at an energy where we can assign the purple color of the film to its influences. Note that the noise in the $AuAl_2$ measurement is less than in the Au film because the 785-nm laser used in this experiment is more stable than the HeNe laser.

2.6 Possible applications for $AuAl_2$ nanoparticles

In practical plasmonic applications, $AuAl_2$ will be likely used in the form of nanoparticles. Such particles have not yet been made, but we can estimate their optical properties from the bulk dielectric function [22]. Figure 2.18 presents the theoretical scattering and absorption cross sections for spherical 20 nm diameter nanoparticles made from either $AuAl_2$ or Au, which is shown for comparison.

It is interesting to note that that $AuAl_2$ nanoparticles absorb light nearly uniformly over the entire ultraviolet and visible spectrum ranging from 300 to 750 nm. The order of magnitude of the absorption cross section is relatively comparable to one of the absorbance peaks in single-walled carbon nanotubes [35], and significantly higher than the absorbance of light-absorbing carbonaceous particles also known as carbon

blacks or black carbons [36]. The other striking property is the ability to absorb light in the infrared region even if the structure is a solid sphere. For other metals, surface plasmon resonances in the infrared are accomplished by more complex structures, such as nanorods, nanoshells, nanostars etc. [37-41]. This suggests possible applications of these particles as light absorbers in the field of obscurants [42] or photothermal cancer therapy [37-40] etc.

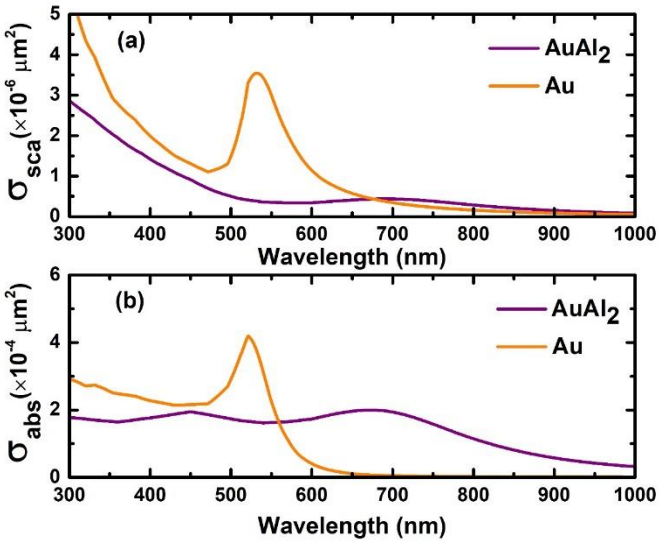

Figure 2.18: (a) Scattering cross section and (b) absorption cross section spectra of 20-nm diameter $AuAl_2$ (purple) and Au (yellow) nanospheres in water suspension calculated using Mie scattering theory.

Note that surface plasmon resonances in single crystal nanoparticles are usually stronger than those in polycrystalline ones [43]. Keast et al. predicted that the theoretical optical spectrum of small spherical $AuAl_2$ nanoparticles should be comparable in strength to that of Au nanoparticles [20], significantly stronger than what is shown in Figure 2.18. The difference between theoretical and bulk measurements may be attributed to defects in the film, which increases electron scattering and plasmon losses. This idea is supported by an experiment by Angela Furrer et al. that showed that the intense purple color of $AuAl_2$ thin film can be removed gradually with increasing doses of ion bombardment that create defects in the crystal, and recovered again by post-irradiation heat treatments that anneals out those defects [28]. The bulk intermetallic will always contain many defects, but a small single crystal nanosphere is likely to be nearly

defect free. The manufacture of such particles may therefore be even more worthy of pursuit than our estimates here indicate.

2.7 Conclusion

Surface plasmon polaritons (SPPs) can be launched in the intermetallic compound $AuAl_2$, also known as purple gold. These surface plasmons are of unsually low energy and account for intense purple color of this compound, even though it has long been believed that the color originates from an interband transitions. We have also measured the SPP dispersion relation in $AuAl_2$. It reveals that the plasmon energy in the large wave vector limit corresponds to 2.1 eV, i.e. $\lim_{k\to\infty} E^{exp} = 2.1\ eV$, notably lower than in Au. Due to the defects in the $AuAl_2$ film during the fabrication process, SPs in this intermetallic are quite lossy. In terms of SP sensing, $AuAl_2$ exhibits the ability to measure the change in the refractive index of standard sucrose solution, which also confirms the existence of SPs in the $AuAl_2$ film at an energy consistent with a plasmonic origin of the color. When $AuAl_2$ is used in nanoparticle form, Mie scattering theory shows that the small particles absorb light nearly uniformly over the entire visible spectrum with an order magnitude higher cross section than a light-absorbing carbon black. This suggests applications of these particles to solar steam generation and photothermal therapy.

2.8 References

[1] E. Antolini, Alloy vs. intermetallic compounds: Effect of the ordering on the electrocatalytic activity for oxygen reduction and the stability of low temperature fuel cell catalysts, Applied Catalysis B: Environmental, 217 (2017) 201-213.

[2] G.G. Harman, G.G. Harman, Wire bonding in microelectronics, 3rd ed. ed., McGraw-Hill, New York, 2010.

[3] W.C. Roberts-Austen, An introduction to the study of metallurgy, C. Griffin and company; J. B. Lippincott company, London, Philadelphia, 1891.

[4] R.W. Cahn, Materials science: A precious stone that isn't, Nature, 396 (1998) 523-524.

[5] C. Cretu, E. van der Lingen, Coloured gold alloys, Gold Bulletin, 32 (1999) 115-126.

[6] U.E. Klotz, Metallurgy and processing of coloured gold intermetallics — Part I: Properties and surface processing, Gold Bulletin, 43 (2010) 4-10.

[7] E. Philofsky, Intermetallic formation in gold-aluminum systems, Solid-State Electronics, 13 (1970) 1391-1394.

[8] G. Majni, C. Nobili, G. Ottaviani, M. Costato, E. Galli, Gold-aluminum thin-film interactions and compound formation, Journal of Applied Physics, 52 (1981) 4047-4054.

[9] C. Xu, T. Sritharan, S.G. Mhaisalkar, Interface transformations in thin film aluminum–gold diffusion couples, Thin Solid Films, 515 (2007) 5454-5461.

[10] H. Xu, C. Liu, V.V. Silberschmidt, S.S. Pramana, T.J. White, Z. Chen, M. Sivakumar, V.L. Acoff, A micromechanism study of thermosonic gold wire bonding on aluminum pad, Journal of Applied Physics, 108 (2010) 113517.

[11] N. Noolu, N. Murdeshwar, K. Ely, J. Lippold, W. Baeslack, Phase transformations in thermally exposed Au-Al ball bonds, Journal of Electronic Materials, 33 (2004) 340-352.

[12] H.R. Philipp, AuAl2: Optical Properties and Consideration as a Transparent Electrode Material, physica status solidi (a), 69 (1982) 547-551.

[13] R. Hahn, B. Seraphin, Spectrally selective surfaces for photothermal solar energy conversion, Physics of thin films, 10 (1978) 1-69.

[14] P.B. Johnson, R.W. Christy, Optical Constants of the Noble Metals, Physical Review B, 6 (1972) 4370-4379.

[15] S. Hüfner, J.H. Wernick, K.W. West, The density of states of AuAl2, AuIn2 and AuGa2, Solid State Communications, 10 (1972) 1013-1016.

[16] J.H. Wernick, A. Menth, T.H. Geballe, G. Hull, J.P. Maita, Superconducting, thermal and magnetic susceptibility behavior of some intermetallic compounds with the fluorite structure, Journal of Physics and Chemistry of Solids, 30 (1969) 1949-1956.

[17] A.C. Switendick, A. Narath, Band structure and $^{197}\mathrm{Au}$ Nuclear-Magnetic-Resonance Studies in Au${\mathrm{Al}}_{2}$, Au${\mathrm{Ga}}_{2}$, and Au${\mathrm{In}}_{2}$, Physical Review Letters, 22 (1969) 1423-1426.

[18] I. Perez, B. Qi, G. Liang, F. Lu, M. Croft, D. Wieliczka, Spectroscopic results on the above and below ${E}_{F}$ electronic structure of T${\mathrm{Al}}_{2}$, T=Au and Pt, Physical Review B, 38 (1988) 12233-12237.

[19] L.-S. Hsu, G.Y. Guo, J.D. Denlinger, J.W. Allen, Experimental and theoretical study of the electronic structure of AuAl2, Journal of Physics and Chemistry of Solids, 62 (2001) 1047-1054.

[20] V J. Keast, R L. Barnett, M.B. Cortie, First principles calculations of the optical and plasmonic response of Au alloys and intermetallic compounds, Journal of Physics: Condensed Matter, 26 (2014) 305501.

[21] V.J. Keast, K. Birt, C.T. Koch, S. Supansomboon, M.B. Cortie, The role of plasmons and interband transitions in the color of AuAl2, AuIn2, and AuGa2, Applied Physics Letters, 99 (2011) 111908.

[22] S. Supansomboon, A. Maaroof, M.B. Cortie, “Purple glory”: The optical properties and technology of AuAl2 coatings, Gold Bulletin, 41 (2008) 296-304.

[23] C. Kittel, Introduction to solid state physics, 8th ed. ed., Wiley, Hoboken, NJ :, 2005.

[24] V.J. Keast, An introduction to the calculation of valence EELS: Quantum mechanical methods for bulk solids, Micron, 44 (2013) 93-100.

[25] V.J. Keast, B. Zwan, S. Supansomboon, M.B. Cortie, P.O.Å. Persson, AuAl2 and PtAl2 as potential plasmonic materials, Journal of Alloys and Compounds, 577 (2013) 581-586.

[26] G. Majni, G. Ottaviani, E. Galli, AuAl compound formation by thin film interactions, Journal of Crystal Growth, 47 (1979) 583-588.

[27] M. Moser, P.H. Mayrhofer, H. Clemens, Oxidation Resistance and Ductility of a Coated γ-TiAl Based Alloy, BHM Berg- und Hüttenmännische Monatshefte, 153 (2008) 268-272.

[28] A. Furrer, M. Seita, R. Spolenak, The effects of defects in purple AuAl2 thin films, Acta Materialia, 61 (2013) 2874-2883.

[29] A.V. Kabashin, V.E. Kochergin, A.A. Beloglazov, P.I. Nikitin, Phase-polarisation contrast for surface plasmon resonance biosensors1This paper was presented at the Fifth World Congress on Biosensors, Berlin, Germany, 3–5 June 1998.1, Biosensors and Bioelectronics, 13 (1998) 1263-1269.

[30] J. Homola, Surface Plasmon Resonance Based Sensors, Springer Berlin Heidelberg2006.

[31] D.G. Drescher, N.A. Ramakrishnan, M.J. Drescher, Surface Plasmon Resonance (SPR) Analysis of Binding Interactions of Proteins in Inner-Ear Sensory Epithelia, Methods in molecular biology (Clifton, N.J.), 493 (2009) 323-343.

[32] B.D. Gupta, R.K. Verma, Surface Plasmon Resonance-Based Fiber Optic Sensors: Principle, Probe Designs, and Some Applications, Journal of Sensors, 2009 (2009) 12.

[33] H.H. Nguyen, J. Park, S. Kang, M. Kim, Surface Plasmon Resonance: A Versatile Technique for Biosensor Applications, Sensors (Basel, Switzerland), 15 (2015) 10481-10510.

[34] B.A. Sexton, B.N. Feltis, T.J. Davis, Characterisation of gold surface plasmon resonance sensor substrates, Sensors and Actuators A: Physical, 141 (2008) 471-475.

[35] J.K. Streit, S.M. Bachilo, S. Ghosh, C.-W. Lin, R.B. Weisman, Directly Measured Optical Absorption Cross Sections for Structure-Selected Single-Walled Carbon Nanotubes, Nano Letters, 14 (2014) 1530-1536.

[36] T.C. Bond, R.W. Bergstrom, Light Absorption by Carbonaceous Particles: An Investigative Review, Aerosol Science and Technology, 40 (2006) 27-67.

[37] A.M. Gobin, M.H. Lee, N.J. Halas, W.D. James, R.A. Drezek, J.L. West, Near-Infrared Resonant Nanoshells for Combined Optical Imaging and Photothermal Cancer Therapy, Nano Letters, 7 (2007) 1929-1934.

[38] L.C. Kennedy, L.R. Bickford, N.A. Lewinski, A.J. Coughlin, Y. Hu, E.S. Day, J.L. West, R.A. Drezek, A New Era for Cancer Treatment: Gold-Nanoparticle-Mediated Thermal Therapies, Small, 7 (2011) 169-183.

[39] B. Lissett, S. Jiantang, F. Kun, L. Nastassja, N. Vengadesan, C. Joseph, D. Rebekah, Enhanced multi-spectral imaging of live breast cancer cells using immunotargeted gold nanoshells and two-photon excitation microscopy, Nanotechnology, 19 (2008) 315102.

[40] X.H. Huang, I.H. El-Sayed, W. Qian, M.A. El-Sayed, Cancer cell imaging and photothermal therapy in the near-infrared region by using gold nanorods, J. Am. Chem. Soc., 128 (2006) 2115-2120.

[41] N. Cennamo, #039, G. Agostino, A. Donà, G. Dacarro, P. Pallavicini, M. Pesavento, L. Zeni, Localized Surface Plasmon Resonance with Five-Branched Gold Nanostars in a Plastic Optical Fiber for Bio-Chemical Sensor Implementation, Sensors, 13 (2013) 14676.

[42] G.A. Paul, Modelled infrared extinction and attenuation performance of atmospherically disseminated high aspect ratio metal nanoparticles, Journal of Optics A: Pure and Applied Optics, 9 (2007) 278.

[43] H. Ditlbacher, A. Hohenau, D. Wagner, U. Kreibig, M. Rogers, F. Hofer, F.R. Aussenegg, J.R. Krenn, Silver Nanowires as Surface Plasmon Resonators, Physical Review Letters, 95 (2005) 257403.

Chapter 3 Tunable fluorescence intensity by pH-responsive polymer layers on Au nanospheres

A fluorophore is a fluorescent molecule or other entity that can absorb incoming light and reemit it with a different and redder wavelength. The time between absorption and reemission is on the order on nanoseconds, which distinguishes it from the phenomenon of phosphorescence where the emission time is on the order of milliseconds to seconds. Fluorescence spectroscopy is an analytical technique that has been in use for several decades. It can produce a high-contrast image or detect a single molecule. It can also be used as a probe, a sensor, or a biomarker in medical diagnostics and other fields. Despite the versatility of its applications, the use of fluorophores is still limit owing to finite quantum yield, photostability, and emission intensity [1].

To improve the detection sensitivity of fluorescence spectroscopy, one of the possible ways is to couple a fluorophore with a metal nanoparticle (MNP). The effect of a MNP on the emission dynamics of fluorophores opens a new field of research known as “plasmon-enhanced fluorescence (PEF)”. Many equivalent terms are used to describe the effect we are interested in, including (i) metal-enhanced fluorescence (MEF), (ii) surface plasmon-enhanced fluorescence spectroscopy (SPFS), or (iii) surface-enhanced fluorescence spectroscopy (SEFS).

3.1 Introduction

3.1.1 Background

PEF is a complex phenomenon, where the emission intensity of a fluorophore may be either quenched or enhanced by a nearby MNP. The fluorophore-MNP interaction is influenced by several parameters including the size, shape, and surface chemistry of the MNP, the fluorophore-particle spacing, and the spectral overlap between the LSP spectrum of the MNP and the fluorophore absorption and emission spectra [2-5]. Of these parameters, the distance between the surface of the MNP and the fluorophore plays the primary role in determining the fluorescence intensity [2, 6, 7].

The optical effects originating with LSPs in MNP can be tuned by changing particle shape and size, the material composition of the particle, and the dielectric function of the surrounding medium [8-13]. This enables a precise control over the PEF effect, which is of great use in developing it into an optical contrast probe for biolabelling and bioimaging. When PEF is used to enhance fluorescence intensity, it provides a higher signal-to-noise ratio and better sensitivity, and decreases photobleaching rates [14, 15]. When used to quench fluorescence, PEF can be used for identification of biomolecules, tumor cells, and toxic pollutants [16-20].

The change in fluorescence intensity can be theoretically explained by the Purcell effect. In this present situation, LSPs act like an optical resonator that provides an enormous increase in the local density of optical states (LDOS) near the particle, thereby providing additional channels for relaxation that increase the emission rate of the fluorophore [21]. Accordingly, the fluorophore's excited state lifetime decreases, which brings about a reduction in photobleaching and a corresponding change in quantum yield [7, 14, 22-28] that depends on whether the states into which the emission is coupled are able to radiate light or not. This results in either an increase or a decrease in the effective fluorescence intensity.

Figure 3.1 schematically illustrates the Jablonski diagrams of the emission of a fluorophore with and without a MNP.

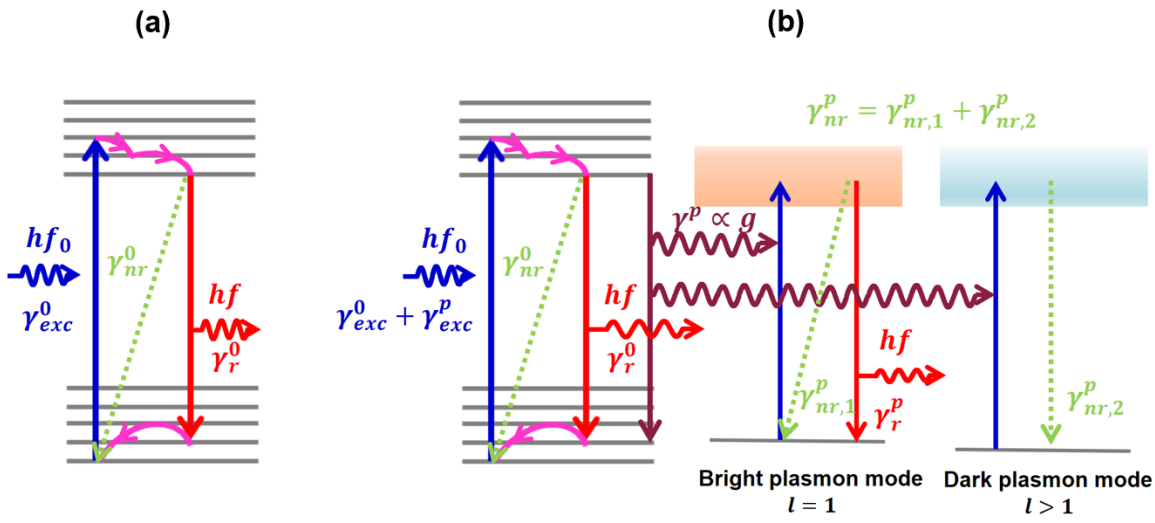

Figure 3.1: Jablonski diagrams of a fluorophore (a) without and (b) with a MNP. The latter is the situation in PEF.

In the absence of a MNP, the fluorophore absorbs energy from incoming photons with an excitation rate γ_{exc}^0 where the superscript zero indicates the state without a MNP. The electronic state of the fluorophore changes from the ground state to a higher excited state. The excited state then rapidly relaxes to a lower excited state by releasing vibrational energy in the form of phonons into the surrounding medium. The electrons remain in the lowest vibrational level of the electronic excited states on the time scale of nanoseconds known as the "fluorescence lifetime", and they relax to an accessible vibrational level of the electronic ground state by two processes. The first process is to emit a photon with a radiative rate γ_r^0, causing the fluorescence emission. The excited state can also decay nonradiatively at a rate of γ_{nr}^0 through various processes ultimately resulting in the production of heat rather than light.

In the presence of a MNP placed near a fluorophore, the total excitation rate of the fluorophore increases by an additional rate due to LSPs denoted by γ_{exc}^p. Here, the superscript p indicates that the process is plasmon-induced, i.e., it is due to coupling to plasmon modes in the nearby MNP. On the decay side, the interaction between the fluorophore and the MNP opens a new decay channel with rate γ^p owing to the presence of plasmons. This new rate is proportional to the near-field enhancement factor $g = (E_{local}/E_0)^2$ where E_0 is the amplitude of the electric field of the incident light. This decay results in the excitation of a

plasmon mode in the MNP, which in turn can decay either radiatively or non-radiatively. As a result, γ^p is a sum of a radiative and a non-radiative decay rate, or $\gamma^p = \gamma_r^p + \gamma_{nr}^p$.

The new decay channel is then actually the result of a coupling between the dipole of the fluorophore's excited state and the plasmon modes of the MNP. LSP modes with a strong dipole ($l = 1$) character are known as "bright plasmons". Due to their dipole character, they can radiate the energy, releasing it in a form of photons with a radiative rate γ_r^p. Bright plasmons also have a non-radiative channel at some rate $\gamma_{nr,1}^p$. LSP modes made up of higher multipoles ($l > 1$), including quadrupoles, octupoles, etc. are known as "dark plasmons" due to their lack of dipole character. These higher-order modes cannot decay radiatively, so their decay is dominated by non-radiative decay at some rate $\gamma_{nr,2}^p$.

The coupling between the fluorophore and the LSPs depends strongly on the distance between the fluorophore and the MNP. If the fluorophore mainly couples to bright plasmons, γ^p is dominated by the plasmon radiative decay at rate γ_r^p, resulting in an enhancement of the fluorescence intensity. However, if the fluorophore is placed closer to the MNP, the dipole from the fluorophore mainly excites dark plasmons. Since these modes radiate poorly, the excitation energy is not converted into photons, which results in the fluorescence quenching [29-37]. The reason higher multipoles are more readily excited when d is small is that they correspond to higher spatial frequencies on the surface of the MNP. The closer the fluorophore is to the surface, the larger the high frequency content of the fluorophore polarization field on the surface, and the larger the coupling to the higher order dark plasmon modes.

Figure 3.2 plots the fluorescence enhancement of a fluorophore placed in the vicinity of a 60 nm diameter Au nanosphere at the distance d from the nanoparticle surface. This enhancement is defined as the ratio of the radiative emission rates of the fluorophore with and without a Au NP present. The excitation and the emission wavelength were assumed to be the same at $\lambda_{exc} = \lambda_{em} = 650$ nm. The dielectric function of pure gold was obtained from the well-known work by Johnson and Christy [68]. This calculation follows the procedures laid out by Bharadwaj et al. [23].

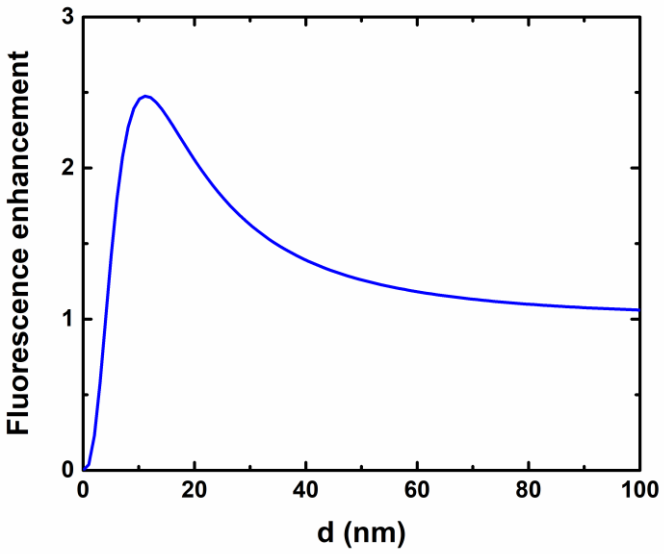

Figure 3.2: Calculated fluorescence enhancement as a function of distance d from the surface of a spherical Au NP with a diameter of 60 nm.

If the fluorophore is placed less than 5 nm from the surface of a Au NP, the fluorescence quenching is observed. The fluorescence enhancement occurs when the distance d is greater than 5 nm and increases rapidly if the fluorophore is further away from the Au NP. The maximum fluorescence enhancement is achieved at a distance around 12 nm, and it decreases slowly if the distance is increased even further.

Note that the calculation does not account for the presence of a dielectric material in which the fluorophore is embedded. Moreover, the computation was the quasi-static assumptions, which results in the observed quenching phenomenon. These results would be improved, if other numerical methods such as the multiple multipole (MMP) method [23], finite difference time domain (FDTD) method [69], finite integration technique (FIT) [70], finite element method (FEM) [71] etc., were use. A good review of the exact solution and numerical computations is discussed in several published articles [72-74].

Because the separation distance d between fluorophore and MNP has a significant impact on fluorescence intensity, fluorescence lifetime, and quantum yield, the effect of varying d has been widely studied both theoretically and experimentally. The earliest experimental work was performed by Drexhage et al. in 1974. They investigated the radiative and nonradiative rates of the emission intensity of a fluorescent dye

(cadmium arachidate) near metallic and dielectric interfaces [38]. Chance et al. also theoretically and experimentally reported the effect of quantum yield and lifetime of an Eu^{3+} chromophore near a metal surface [39, 40]. Recently, most studies have focused on MNPs rather than surfaces because of the potential applications of MNPs in chemical sensors and nanodevices [3-5, 29, 41, 42].

3.1.2 pH-stimulus-responsive polymers as spacers: PAH and PSS

There are many types of spacers that can separate fluorophores from metal nanostructure. Early work in the 1980s used a fatty acid layer [39], a solid argon layer [44], and a SiO_x layer [45] as spacers between fluorophores and metal surface. For fluorophore-MNP separation, polyelectrolyte multilayers (PEMs) are often employed. These are charged polymer films that can be wrapped around nanoparticles using layer-by-layer (LbL) assembly. In this method, a positively charged polymer, e.g. poly(allylamine hydrochloride) (PAH) (see Figure 3.3 (a)), is wrapped around the intrinsically negatively charged MNPs. The particles are then wrapped with a negatively charged polymer such as poly(styrene sulfonate) (PSS) (see Figure 3.3 (c)). This process can be repeated as many times as desired to make a progressively thicker PEM. A single PAH/PSS bilayer contributes to the thickness of a PEM films approximately 1 nm, if the film is applied at near neutral pH, giving good control over the MNP-fluorophore spacing (The PEM films used in this work are deposited at higher pH, which makes them substantially thicker). Schneider et al. demonstrated the quenching effect on two different organic dyes, Fluorescein isothiocyanate (FITC) and lissamine rhodamine B sulfonyl chloride (LISS) deposited on 13-nm-diameter gold nanoparticles (Au NPs) wrapped with PAH/PSS PEMs [28]. Similarly, Kang et al. also investigated the fluorescence quenching and enhancement of cypate as the fluorophore, varying the number of PAH/PSS bilayers [46]. Most studies of this type have used PEMs as spacers of fixed thickness, where the distance between MNPs and fluorophores increases linearly with the number of deposited bilayers applied to the MNP [3-5, 29, 41, 42]. However, some types of PEMs operate as stimuli-responsive polymers or smart polymers [47, 48], where the thickness changes in response to changes in the external environment, such as variations in temperature [49, 50], electric

potential [51-53], magnetic potential [54], mechanical force [55], and pH [56-59]. It is therefore possible to use such PEMs as dynamically tunable spacers between MNPs and fluorophores, which is an effective technique to manipulate PEF. Using this type of tunable spacer may also make it possible to exploit the PEM effect in sensing application. Recently, Yaun et al [7] reported this approach in porphyrin dye and silver nanoparticles separated by poly(acryloyl hydrazide), which is a pH stimulus-responsive polymer [60]. As the ambient pH was varied from 4 to 9, the maximum fluorescence intensity was almost two-fold greater than the reference intensity at pH = 4. This is the only example in the literature of using tunable PEMs to tune the PEF effect that we are aware of.

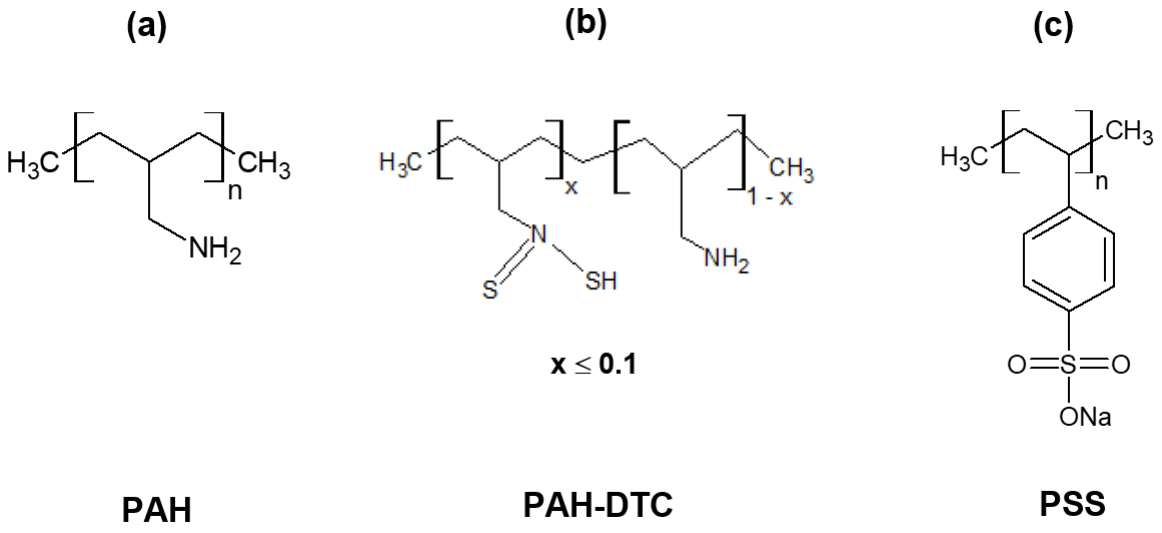

Figure 3.3: Non-fluorescent polyelectrolytes used in the experiment:(a) poly(allylamine hydrochloride) (PAH), (b) PAH-DTC and (c) poly(sodium-4-styrenesulfonate) (PSS).

In this dissertation, we employed the idea of tunable spacers to make particles with greater stability and flexibility and studied the resulting particles more systematically than in previous work. Stability was achieved by depositing PAH-DTC polymer, which is a modified version of PAH where some amine groups have been transformed into dithiocarbamate (DTC), around 30 nm diameter gold nanospheres. The DTC groups in this polymer anchor covalently to the gold surface, which makes the colloid more rubust and stable. These particles were then wrapped with PSS and PAH polymers under conditions that result in a

pH-responsive PEM that is able to change the distance between the Au NPs and fluorophores deposited on the outer surface of the particles. This occurs when bilayers of PAH and PSS are assembled at pH comparable to or higher than the pKa of PAH (8.8) [61, 62]. This leads to a film containing excess amines, uncoordinated with the sulfonate groups in PSS. As the ambient pH is raised, these amine groups lose their charges, repel counter ions and become hydrophobic, making the film shrink. As ambient pH is decreased, on the other hand, amine groups regain their charges, attract counter ions and become hydrophilic, making the film swell. This kind of PEM film can shrink and swell several hundred percent in thickness in response to changes in pH [56-59]. On flat surfaces, the thickness of a single layer PAH deposited in this fashion varies from 7 to 18 nm, while that of a PAH/PSS/PAH film varies from 12 and 42 nm [66]. The thickness in our case may be quite different from these values, but they are in any case significantly larger than 1 nm per bilayer.

3.1.3 Fluorophores: RGCS

In this dissertation, 5(6)-carboxyrhodamine 110 (also known as rhodamine green carboxylic acid), succinimidyl ester hydrochloride (RGCS) was chosen as our indicator dyes for three reasons. First, RGCS is relatively insensitive to change in an ambient pH, which means that we will be able to attribute changes in fluorescence to the PEF effect. Second, the emission spectrum centered around 523 nm overlaps well with the LSP spectrum in Au nanospheres as shown in Figure 3.4, which is a requirement for PEF [63]. Third, this dye is commercially available with a NHS group that makes it easy to bind the dye to the amine group in PAH.

This chapter investigates the effect of Au NPs on fluorescence enhancement of RGCS dyes. The fluorophore distance from the Au NPs is modulated by exploiting the swelling and deswelling property of a particular PEM spacer. First, the surfaces of Au NPs were functionalized with PAH-DTC, a modified PAH film where some amine side groups have been transformed into dithiocarbamate (DTC) groups as shown in Figure 3.3 (b). The DTC group enables this positively charged polymer to covalently bind to the

gold surface, making the anchoring PEM layer strongly bound to the particle, and thereby more robust [43]. The PAH-DTC layer is followed by PSS/PAH bilayers assembled at pH 8.4, which makes the film pH-responsive. Finally, RGCS-PAH was applied to the particles as the terminal layer. The distance between Au NPs and fluorophores could then be varied by changing the ambient pH from 3 to 10 and back, during which time we monitored changes in extinction spectra and fluorescence intensity.

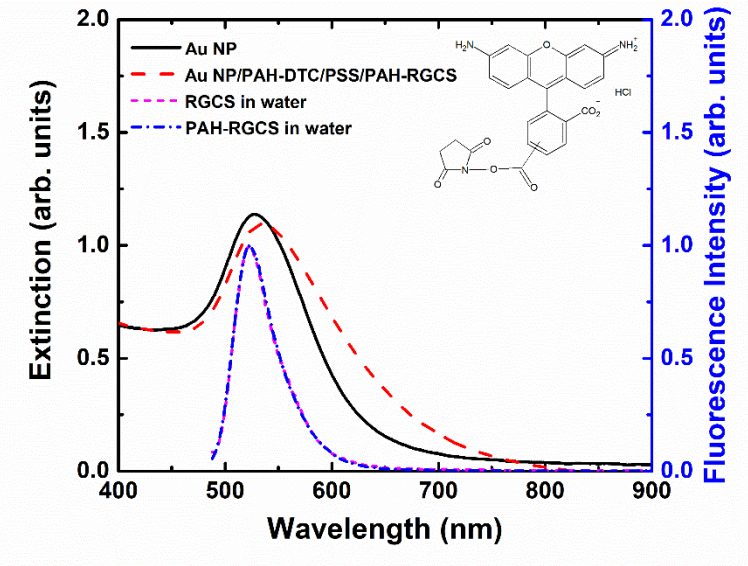

Figure 3.4: Spectra showing the overlap between the extinction spectrum of 30-nm size Au NPs (black solid line) and the fluorescence spectrum of the RGCS dye (magenta short dashed line). The fluorescence spectra of PAH-RGCS (blue dot-dashed line) and a conjugate Au NP/PAH-DTC/PSS/PAH-RGCS nanoparticles (red long dashed line) are also shown. The fluorophores were excited at 470 nm. Inset: molecular structure of RGCS.

3.2 Materials and Methods

3.2.1 Materials

Tetrachloroauric (III) acid trihydrate ($HAuCl_4 \cdot 3H_2O$) and trisodium citrate dihydrate ($Na_3C_6H_5O_7 \cdot 2H_2O$) were purchased from Sigma-Aldrich. Polyelectrolytes employed for multilayer depositions were the

polycation poly(allylamine hydrochloride) (PAH) (M_W = 15 000 g/mol) and polyanion poly(sodium-4-styrenesulfonate) (PSS) (M_W = 70 000 g/mol) and were supplied from Sigma-Aldrich. 5(6)-Carboxyrhodamine 110, succinimidyl ester hydrochloride (RGCS) was obtained from Setareh Biotech. All reagents were of analytical grade and used as received without further purification. Nanopure water with resistivity 18.2 MΩ-cm and total organic carbon (TOC) less than 1 ppb used in all experiments was produced by a Barnstead™ *Nanopure*™ system.

Unless otherwise stated, the reaction vessels used in all experiments were standard borosilicate glass containers (e.g. beakers, Erlenmeyer flasks etc.) that were precleaned with aqua regia (1:3 V/V of concentrated HNO_3 and HCl acids, respectively) for 20 min, followed by rinsing with copious amounts of nanopure water and dried in an oven at 120 °C for 60 min.

3.2.2 Preparation of polymer solutions and derivatives

3.2.2.1 PAH and PSS solution

The base solution of PAH was prepared by dissolving 400 mg of PAH in 50 mL in nanopure water (8 mg/mL) while stirring for a minimum of 12 h. Similarly, the base solution of PSS was obtained by dissolving 400 mg in 50 mL nanopure water (8 mg/mL). Both base solutions were adjusted to pH 8.4 using 1 M solutions of NaOH and HCl.

3.2.2.2 PAH-DTC solution

Dithiocarbamate (DTC)-anchored PAH (PAH-DTC) was obtained using the procedures described by Kai Chen et al [43] following the reaction shown in Figure 3.5. Briefly, a 100 mM (monomer basis) PAH solution was prepared by dissolving 28 mg of PAH in 3 mL nanopure water for at least 12 h or overnight, and the pH of the solution was raised from ~3.4 to 8.80 using NaOH. The solution was transferred to a capped vial and degassed for 10 min with argon (Ar). The solution was then injected with 30 μL of 1 M CS_2 in ethanol, followed by vortex mixing for 30 s, and left to stir gently for 6 h.

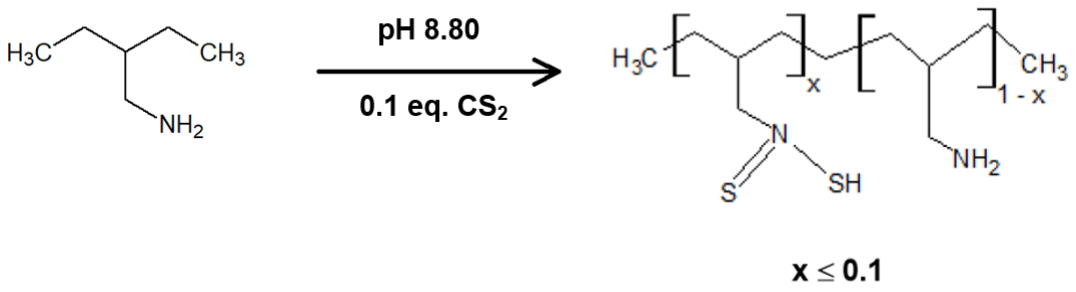

Figure 3.5: Reaction scheme for PAH-DTC formation.

3.2.2.3 PAH-RGCS solution

To make the PAH-RGCS conjugate, 0.16 mg RGCS (a quantity corresponding to 1% of the available amines in the dissolved PAH) was dissolved in 2 mL purified anhydrous DMF, and then added to 18 ml of an aqueous solution of PAH (8 mg/mL) at pH 8.4, which was stirred at room temperature for at least 6 hours. The solution was then dialyzed (Spectra/Por 6 Dialysis Membrane MWCO: 2 kD) against a mixture of isopropanol and pure water (2:8 v/v) for 5 days to remove unreacted RGCS and reaction byproducts. The alcohol/water mixture was replaced daily during dialysis. The thus purified solution was kept at room temperature and in darkness until used.

The hydrolysis of RGCS NHS ester with primary amines in PAH yields RGCS-conjugated PAH (PAH-RGCS) as a primary product and NHS as a byproduct as shown in Figure 3.6.

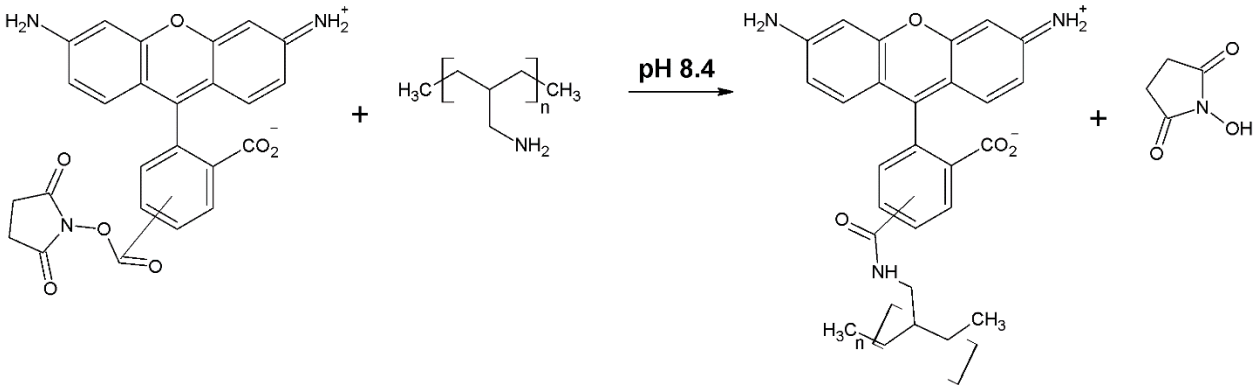

Figure 3.6: Conjugation of RGCS to PAH in a primary-amine-free aqueous solution at pH 8.4. This hydrolysis reaction forms a stable amide bond between RGCS and PAH.

3.2.3 Synthesis of citrate stabilized Au colloids

Au NPs with a mean diameter of 30 nm were fabricated by the well-known standard citrate reduction method pioneered by Turkevich and further developed by Frens [64, 65] as follows: 600 μL of a 1% w/v (or 34 μM) solution of trisodium citrate dihydrate was rapidly injected into 50 mL of a 0.01% w/v (or 0.25 μM) solution of $HAuCl_4 \cdot 3H_2O$ while under boiling and vigorous stirring. After approximately 5 min, the color turned purple and the solution was removed from the heat and allowed to cool down. The solution was kept in darkness at 4 °C until use. The resulting Au particles are terminated with negatively charged citrate ligands. The average size of the particle is around 32 nm based on imaging with scanning electron microscopy as depicted in Figure 3.7.

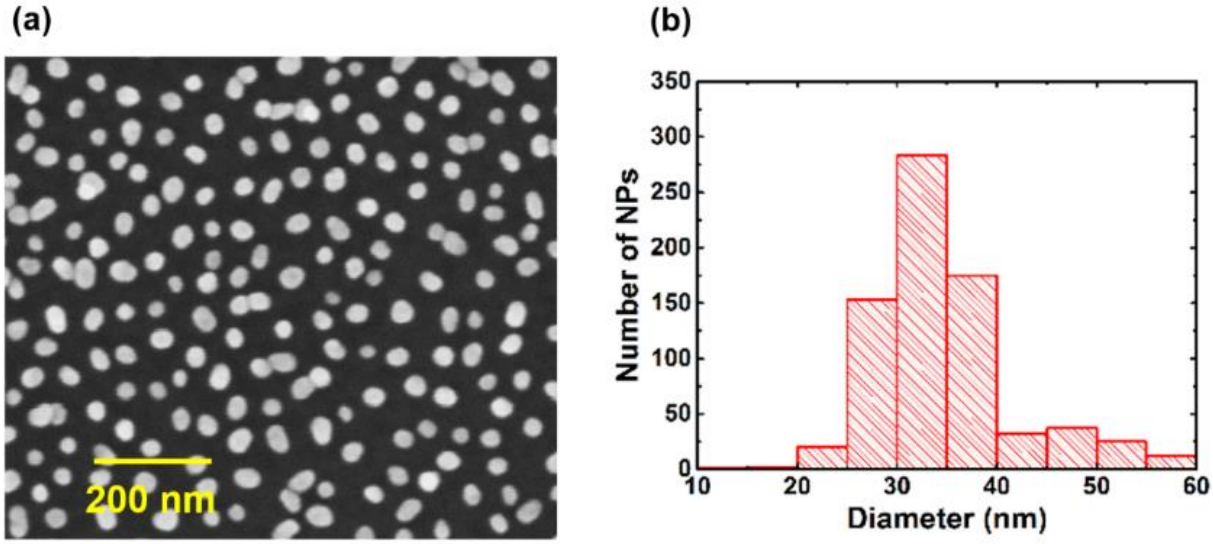

Figure 3.7: (a) A FESEM micrograph of Au NPs. (b) A particle size distribution based on 748 particles with the average diameter around 32 nm.

3.2.4 Polymer deposition on Au NPs

The innermost, covalently anchored polyelectrolyte layer was applied by slow dropwise addition of 3 mL of the PAH-DTC solution into 30 mL Au NP colloid while under vigorous stirring. This suspension was

then stirred at moderate speed for a further 2 h. The colloid was then transferred into 1.5 mL polypropylene Eppendorf Safe Lock tubes and centrifuged (Eppendorf model 5430) at 4000 g for 45 min. 98% of the supernatant was discarded, followed by redispersion to the original volume with nanopure water. The suspension was concentrated by centrifugation and resuspended two additional times and finally diluted to 15 mL. In this dissertation, such a suspension is denoted Au NP/PAH-DTC because Au NPs were wrapped with PAH-DTC polymer.

A PSS layer was then deposited by dropwise addition under vigorous stirring of 15 mL of Au NP/PAH-DTC into 15 mL of the base PSS solution. This suspension was stirred at moderate speed for a further 12 h in darkness. It was purified by centrifugation and redispersion in the same way as in the PAH-DTC deposition step, except that centrifugation was carried out for 50 min at 3000 g, and only performed twice. In the final step, the resulting Au NP/PAH-DTC/PSS suspension was diluted to 15 mL.

PAH and PAH-RGCS were deposited with the same protocol as PSS, except that centrifugation and redispersion were performed three times.

3.2.5 Characterization of pH-responsive Au NPs

NP suspension extinction spectra were measured with an Ocean Optics H2000CG-UV-NIR spectrophotometer and a Halogen lamp (Ocean Optics DH-2000-s), using 1 cm path length quartz cuvettes. The zeta (ζ)–potential measurements were performed on a Malvern Intruments Zetasizer Nano ZS in a folded capillary zeta cell (DTS 1070). Fluorescence spectra were collected with a Perkin Elmer LS 45 luminescence spectrometer using a 470 nm excitation wavelength of a scan rate of 150 nm/min, and with entrance and exit slits widths both set to 10 nm resolution. For the fluorescence measurements only, samples were diluted three times before the measurement.

3.3 Results and Discussions

3.3.1 Fluorescence properties of RGCS dyes and PAH-RGCS polymers

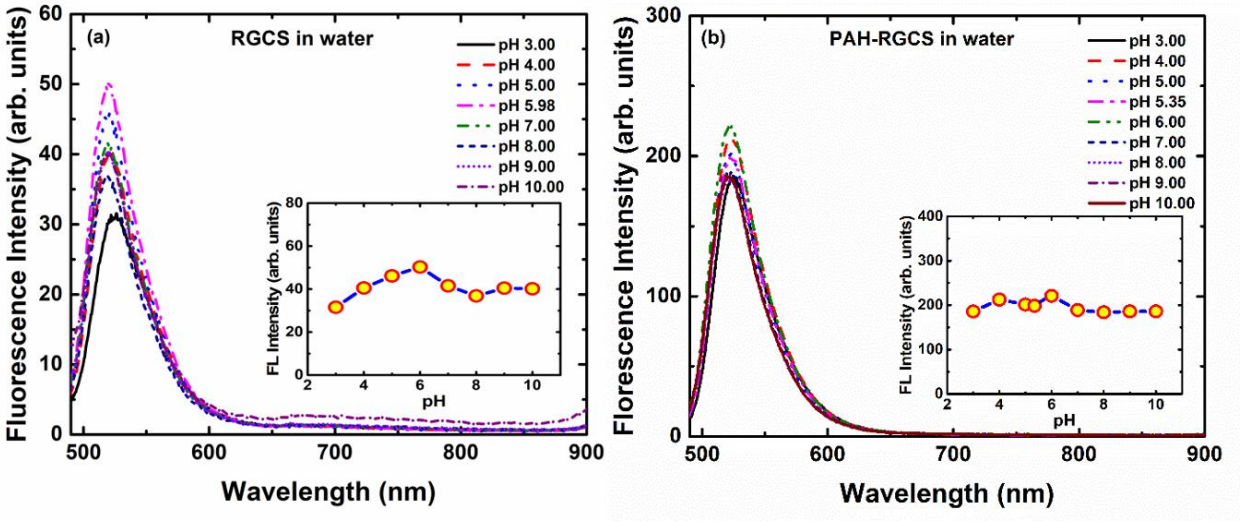

Figure 3.8: Fluorescence emission spectra of (a) RGCS dye in water and (b) PAH-RGCS polymers in water as a function of pH. The insets show a relatively small change of maximum fluorescence intensity vs pH. The magenta long-dashed-dot-dashed- lines on both plots represent the fluorescence intensity at the original pH before pH adjustment which were 5.98 and 5.35, respectively.

Figure 3.8 (a) depicts fluorescence spectra of RGCS fluorophores dissolved in water at various pHs. It reveals that the change in fluorescence intensity with pH in the range of 3 to 10 is fairly small (around ±19%). In addition, most spectra in Figure 3.8 peak around 523 nm. The exception is the fluorescence spectrum of RGCS solution at pH 3, however, which is lower in intensity and exhibits a slight redshift in emission wavelength from 523 to 528 nm. As shown in Figure 3.8(b), the fluorescence intensity variation of dissolved PAH-RGCS is even smaller than in the free dye, showing a variation in intensity at less than ±8% with pH adjustment, with all fluorescence spectra peaking around 524 nm. The smaller variation in the polymer-bound could be due to the amine groups in PAH, which at low pH gain a positive charge that repel the hydronium ions so that the local acidity at the dye molecules is lower than in the free solution, leading to less variation in fluorescence intensity in PAH-RGCS. Therefore, in the pH range 3-10, we can treat the PAH-RGCS fluorescence intensity is largely independent of pH.

3.3.2 Characterizations of Au NPs and their derivatives

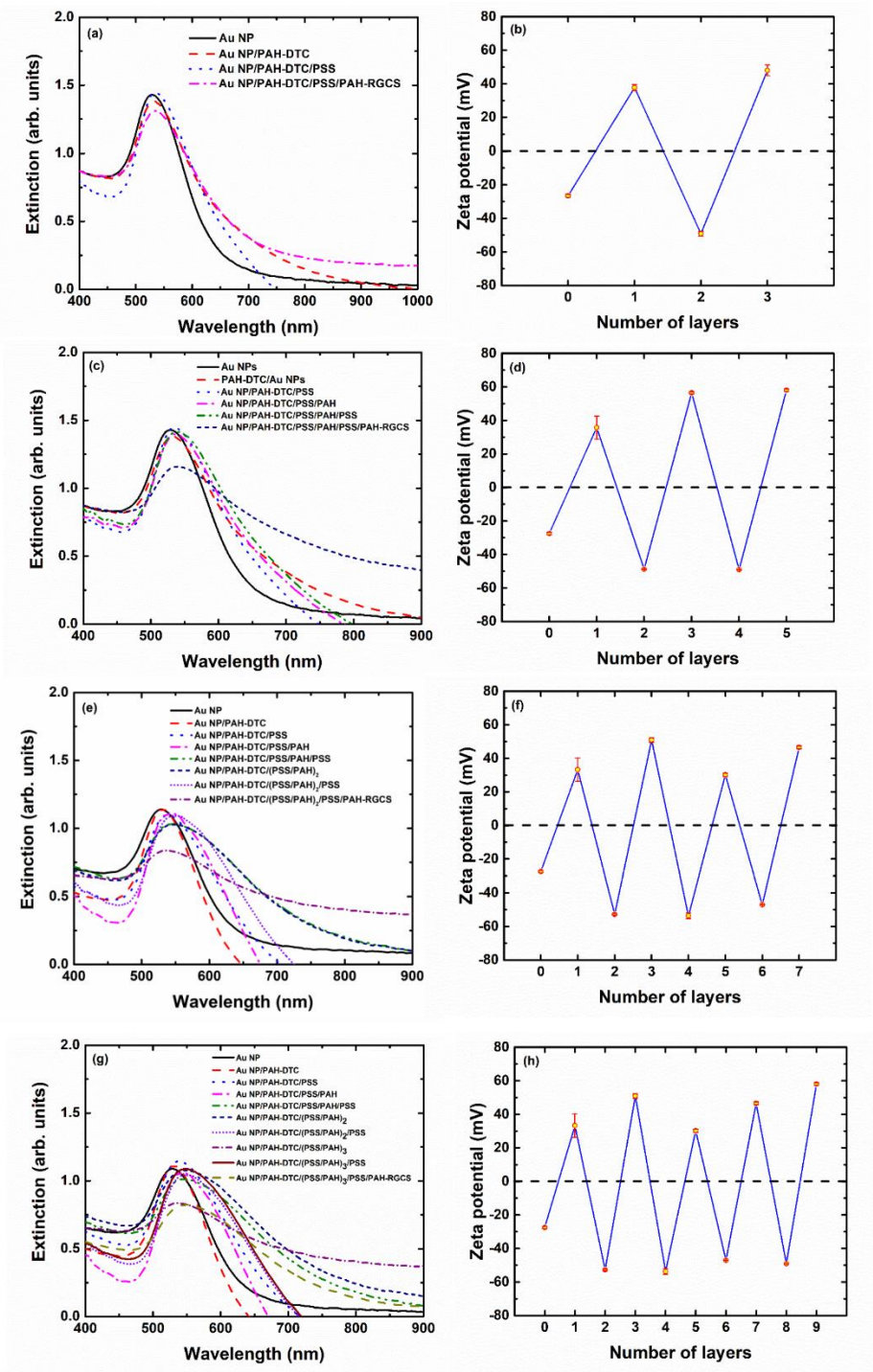

Figure 3.9: (a), (c), (e), and (g) plot extinction (=absorption + scattering) spectra of different Au NPs, while (b), (d), (f), and (h) show corresponding zeta potentials development during polymer depositions.

In this dissertation, we made the Au NPs that were wrapped with 3, 4, 5, 6, 7, and 9 polymer layers, which will be denoted as the 3-, 4-, 5-, 6-, 7-, and 9- layer particles, respectively. The innermost layer is PAH-DTC for particles with an odd number of polymer layers, the outermost layer is a positively charged PAH-RGCS. On the other hand, for the particles with an even number of polymer layers, the two outermost layers are PAH-RGCS followed by a negatively charged PSS. The intermediate layers were contributed as $PSS/(PAH/PSS)_n$, where n is an integer between 0 and 3.

Figure 3.9 (a) illustrates the extinction spectra of Au NPs and their corresponding Au derivatives for particles that were wrapped with 3 polymer layers. A minute drop in the 527-nm peak extinction indicates a loss of particles from suspension after the first layer (PAH-DTC) has been deposited, confirming that the resulting particle suspension is relatively stable. Further loss of particles is seen after the second (PSS) and the third layer (PAH-RGCS) polymer wrapping as evidenced by small drops in the extinction peaks. However, the total drop in the extinction peak is less than 10%, indicating a high yield in the fabrication process. An increase of LSP wavelength λ_{LSPR} from 527 nm to 534 nm can be attributed to an increase in index of refraction in the surrounding medium due to the polymer coating. Nevertheless, after the second and third polymer deposition, any change in λ_{LSPR} is all but indiscernible, demonstrating that these polymers do not have a significant impact on the optical properties of Au NPs.

For the 5-layer particle, a significant drop of the extinction peak is observed after the outermost layer (PAH-RGCS) was deposited, indicating a loss of particles during the fabrication process. A wider spectrum is also noticed due to the aggregations of the particles as shown in Figure 3.9 (c). For the 7- and 9- layer particles (see Figure 3.9 (e) and (g)), we observe an increase of λ_{LSPR} more clearly due to an increase in refractive index in the surrounding medium from the polymer coating. In addition, further loss of particles is noticed after each successive polymer wrapping as evidenced by the drop of the extinction peaks. We also see the wider spectrum because of particle aggregation as the number of polymer layers is larger. Even though some particles were lost during the fabrication process for the 5-, 7-, and 9- layer particles, the total drop in

the extinction peak is less than 25%. This yield is good enough for the study in the change in fluorescence intensity when the pH of the suspension was varied.

Figure 3.9 (b), (d), (f), and (h) illustrate the zeta potentials of the Au NPs as there are wrapped with successive polymer layers. We observe that the potentials alternate between negative and positive values, thereby suggesting the complete encapsulation of each polymer after the centrifugation-redispersion step. In addition, zeta potentials consistently greater than 25 mV is consistent with relatively stable suspensions exhibiting little particle aggregation.

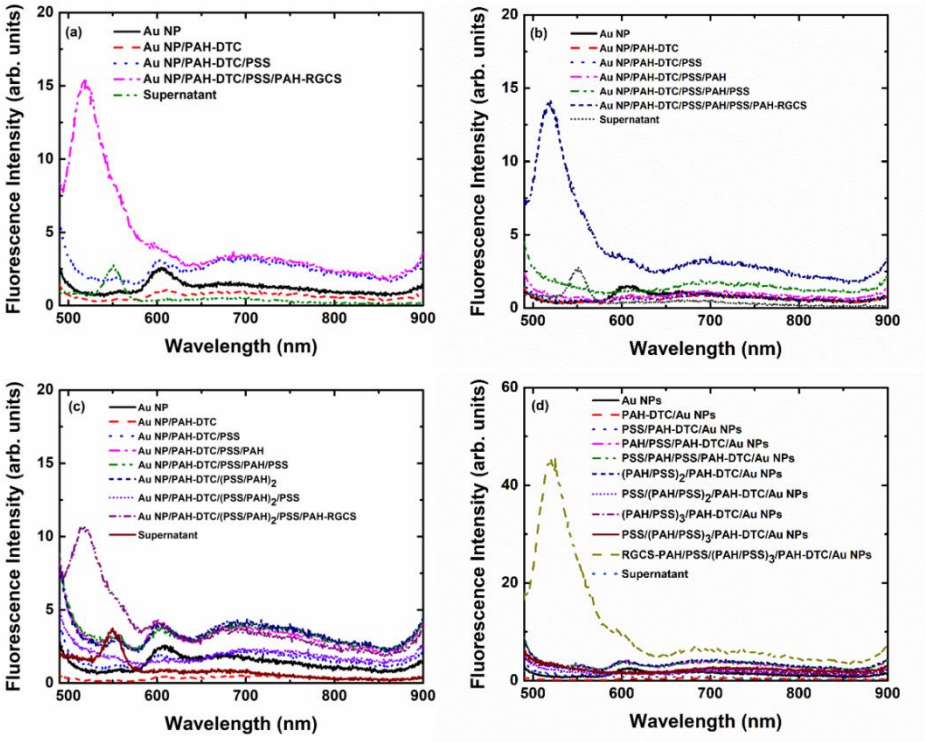

Figure 3.10: Fluorescence spectra of Au NPs, their derivatives, and supernatant from particles with (a) 3, (b) 5, (c) 7, and (d) 9 polymer layers.

To verify that fluorescence from the RGCS dyes was due to dye molecules attached to the nanoparticles via PAH-RGCS polymers, each particle derivative was characterized by fluorescence spectroscopy as shown in Figure 3.10. The characteristic 523 nm fluorescence peak appears when the outermost PAH-RGCS layer has been applied. In particular, the supernatant does not show any significant fluorescence.

This means that the observed fluorescence results nearly entirely from dye attached to the Au particles rather than from free PAH-RGCS in the solvent.

3.3.3 pH-dependent extinction and fluorescence properties of the 3-layer particles

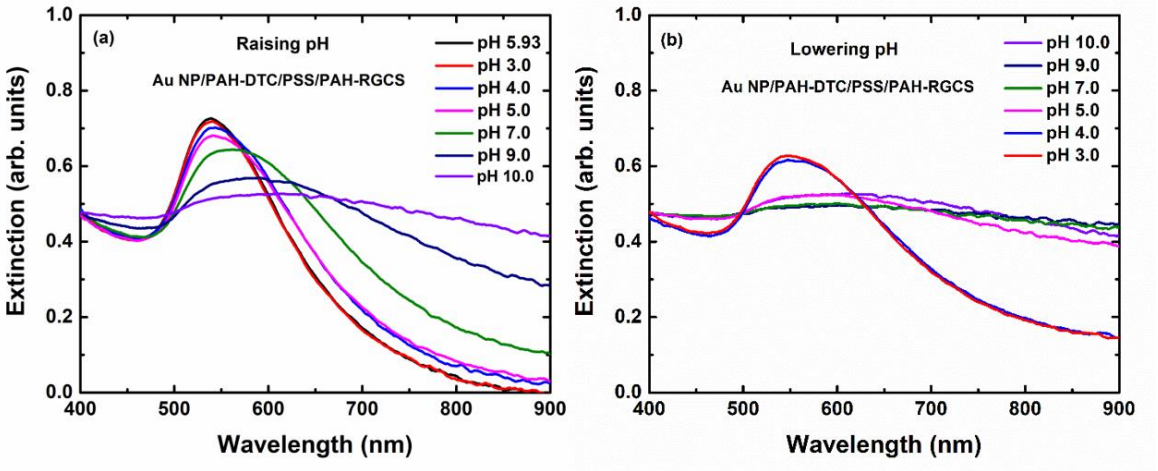

Figure 3.11: Extinction spectra of Au NP/PAH-DTC/PSS/PAH-RGCS when the ambient pH of the suspension was varied by (a) raising the pH and (b) lowering the pH.

As the pH of the particle suspensions is raised from acidic to alkaline, the suspension extinction spectrum redshifts and becomes much wider as shown in Figure 3.11 (a). When the pH is returned to acidic, the spectrum narrows and blueshifts, partially recovering to its original appearance as shown in Figure 3.11 (b). Because the outermost layer of the particles is positively charged due to primary amines in PAH, it will lose some of its charge as the pH approaches the pKa of PAH. This results in the flocculation of particles at high pH that in turn produces a broadening of the spectrum due to the redshifting of plasmon modes in the floccuates. As the pH is lowered, the amines regain their charge, and this makes the particles tend to redisperse. The reversal is not complete, as some particles irreversibly aggregate at the higher pH.

As the pH of the particle suspensions is raised from acidic to alkaline, the fluorescence spectrum intensities and redshifts as shown in Figure 3.12 (a). When the pH is returned to acidic, the spectrum decreases and redshifts a little as shown Figure 3.12 (b).

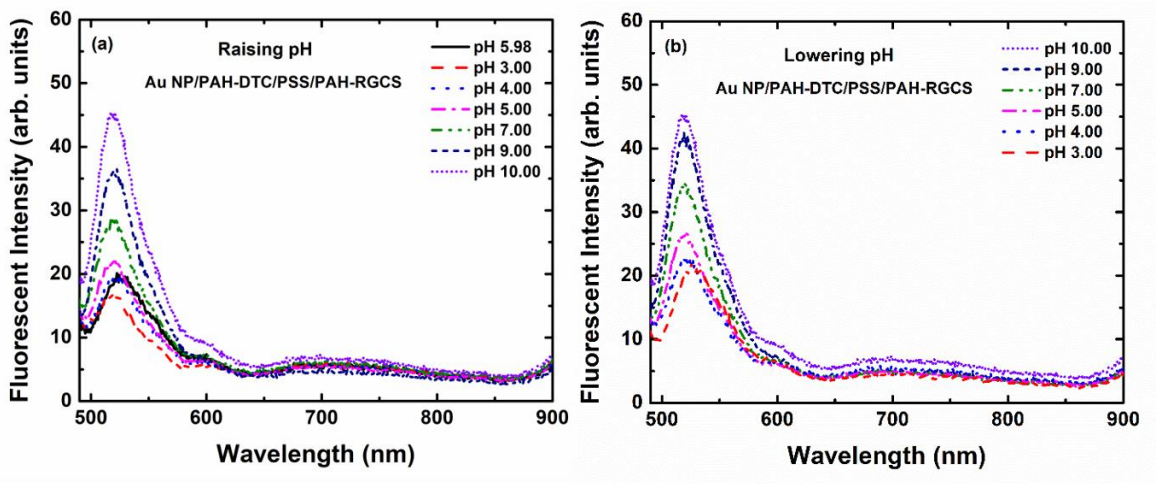

Figure 3.12: Fluorescence spectra of Au NP/PAH-DTC/PSS/PAH-RGCS when the ambient pH of suspension was varied in (a) raising pH and (b) lowering pH.

As mentioned in the introduction, the PEF enhancement efficiency is strongly sensitive to the distance between fluorophores and MNPs. The observed enhancement of the fluorescence intensity with pH can be attributed to the swelling and deswelling behavior of the PAH-rich PEM. At low pH, PAH gains more charges and swells, thereby increasing the PEM thickness as well as the distance between the fluorophores and the Au NPs. Since the coupling between fluorophores and plasmon modes decreases exponentially with the distance from the surface, this leads to a reduction in fluorescence intensity. At high pH, the PAH polymer layers lose their charges and deswell, so that the polymer shell thickness decreases, thereby decreasing the distance between the fluorophores and the Au NPs. Accordingly, the plasmon-fluorophore coupling increases, leading to an increase in fluorescence intensity. If the fluorophores are placed near the Au NPs at an optimal distance, the PEF enhancement is maximized. In this experiment, a 2.8-fold increase in fluorescence intensity was observed in the 3-layer particles, as the pH was raised from 3 to 10. Though the fluorophores are near the surface of Au NPs at pH 10, the distance is still beyond the range of the dark plasmon effect, which accounts for the observed fluorescence enhancement.

Changing the pH of the particle suspension means adding fluid to slightly diluting it and thereby potentially reducing the fluorescence intensity for reasons unrelated to PEF. However, in this experiment, no more

than 20 μL was added to each 15 mL liquid not during each pH adjustment step so that the total dilution of the suspension amounted to less than 5%. Therefore, the observed fluorescence enhancement from this experiment results entirely from the presence of Au NPs and the change in the distance from the Au NPs and the fluorophores rather than changes in the suspension concentration.

We also observe that the pH-induced fluorescence intensity modulation is reversible at least 3 times when the pH of the suspension is repeatedly cycled between pH 3 and 10 as shown in Figure 3.13. This results from the property of these PAH film that their thickness changes with pH, and it is repeatable for multiple cycles [67]. It is notable that the fluorescence intensity trends upward as the experiment proceeds, which could be an impediment to using the particles in sensing applications. One possible explanation for this drift could be that successive swell/deswell cycles cause intermixing of the PAH-RGCS with the rest of the PEM, bringing fluorophores on average closer to the particle, leading to increased PEF.

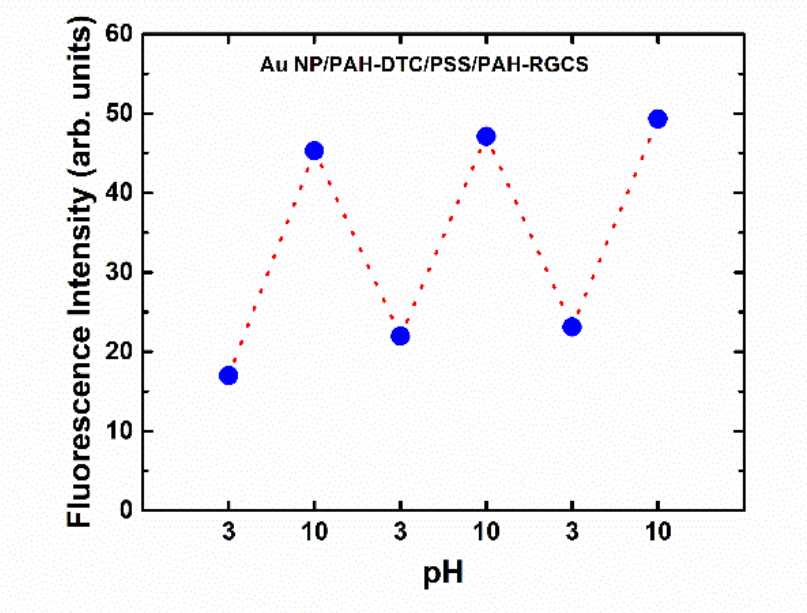

Figure 3.13: Reversible changes of fluorescence intensity of Au NP/PAH-DTC/PSS/PAH-RGCS when the pH of the suspension was alternately switched between pH 3 and pH 10.

3.3.4 pH-dependent fluorescence properties of the 5-, 7-, and 9-layer particles

The graphs in Figure 3.15 (a), (c), (e), and (g) show the peak fluorescence intensity plotted against pH for 3-, 5-, 7-, and 9- layer particles, respectively. Figure 3.15 (a) is in fact a summary of Figure 3.12. In all cases, we see an increase in intensity with pH, and a decrease as it is lowered again. The relationship is nearly linear, with only a small amount of hysteresis, which is very encouraging for potential sensing applications. Moreover, the fluorescence intensity is larger when the particles are wrapped with a larger number of polymer layers. We attribute this to a larger surface area in the particles with a thicker PEM, which allows more fluorophores to be conjugated to surface amine groups, resulting in higher fluorescence intensity.

From Figure 3.14, we can see that even though the fluorescence intensity at high pH rises rapidly with PEM thickness, a much smaller increase is seen at low pH. We may be able to account for this observation by taking into account the distance-dependent fluorescence intensity.

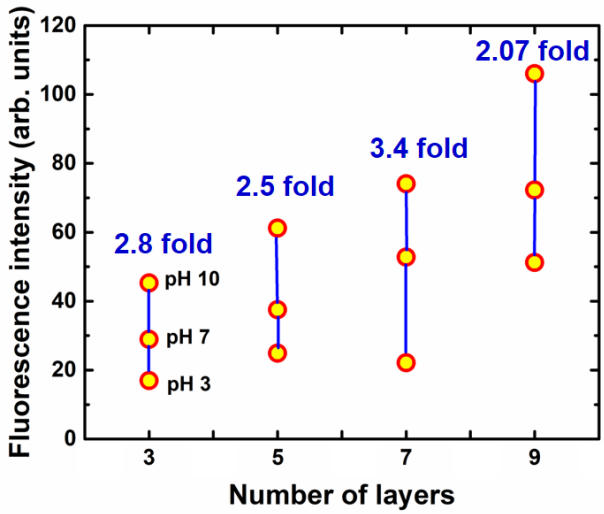

Figure 3.14: A plot of fluorescence intensity at pH 3, 7, and 10 of Au NPs wrapped with 3, 5, 7, and 9 polymer layers. The number above the line indicates the ratio in fluorescence intensity between pH 10 to pH 3.

To better visualize the change in the fluorescence spectra at different pH, Figure 3.14 summarizes the changes in fluorescence intensities at pH 3, 7, and 10 for the 3-, 5-, 7-, and 9- layer particles.

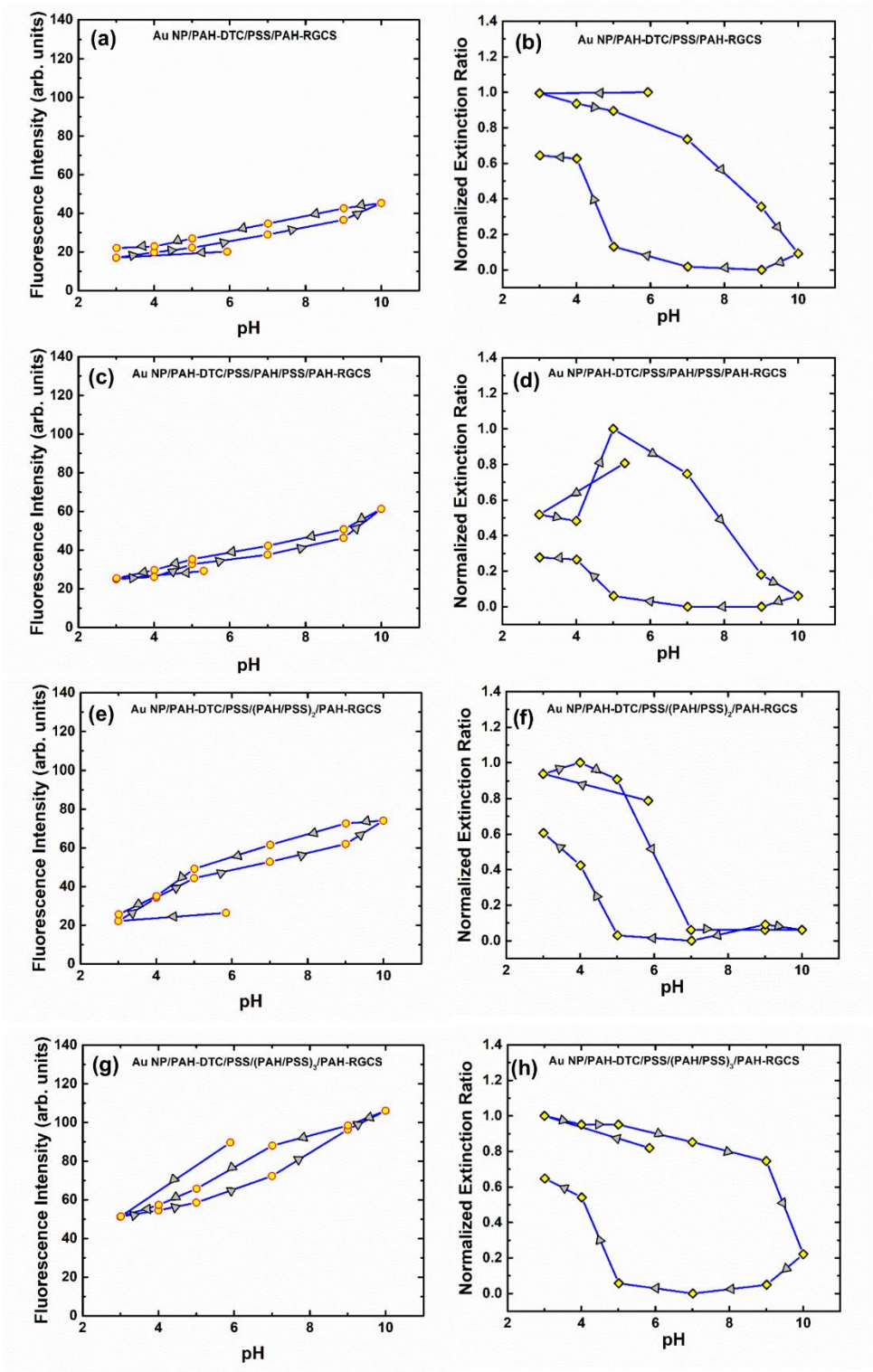

Figure 3.15: (a), (c), (e), and (g) peak fluorescence intensity as a function of pH in 3-, 5-, 7-, and 9- layer particles. (b), (d), (f), and (h) Normalized extinction ratio (see text) as a function of pH. The arrows indicate the change of either extinction spectrum or fluorescence intensity as the ambient pH was varied.

Here, the number above the fluorescence intensity at pH 10 indicates the ratio of the fluorescence intensity at pH 10 to that at pH 3. Although all ratios are above 2, the maximum 3.4-fold ratio was observed with particles wrapped with 7 polymer layers.

At low pH, the PEM films are fairly thick, likely putting the dye at distances from the particle where the PEF decreases rapidly with film thickness (see **Figure 3.2**). This decrease counteracts the increase due to a larger amount of dye on the surface, so that we observe little increase in fluorescence intensity for the 5- and 7-layer particles at low pH. At high pH, the fluorescence intensity increases much more with the number of polymer layers wrapped around the particles. This may be due to the thinner films at higher pH placing most of the dye in the region of maximum fluorescence enhancement where the total intensity is relatively insensitive to changes in d. Since the particles with thicker PEMs have more dye, the consequently fluoresce more brightly at high pH.

3.3.5 pH-dependent fluorescence properties of the 4- and 6- layer particles

The particles discussed so far have been wrapped with an odd number of polymer layers. In other words, the outermost layer is PAH-RGCS, which is positively charged. To avoid particles flocculation at high pH, it would be advantageous if the final polymer layer could be a strong polyelectrolyte such as PSS.

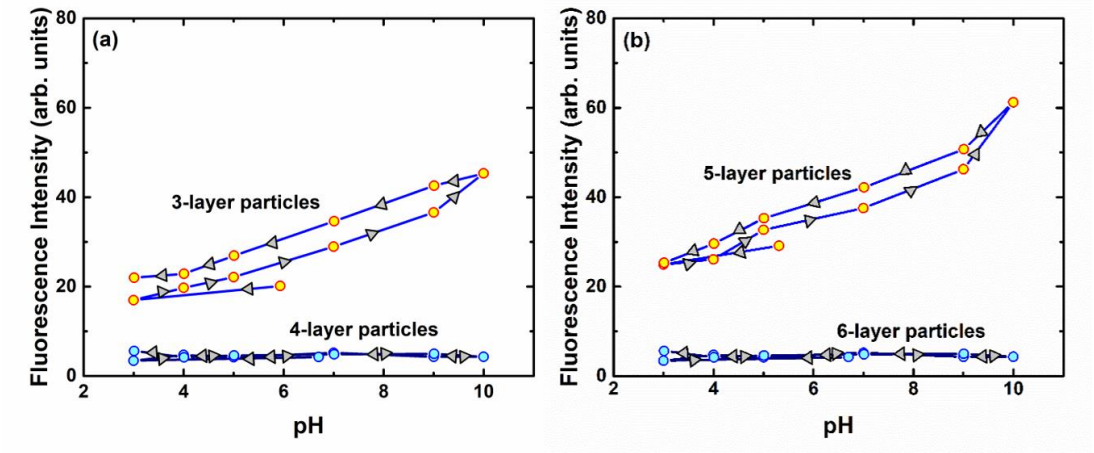

Figure 3.16: Peak fluorescence intensity as a function of pH of particles wrapped with (a) 4 layers and (b) 6 layers of polymers. The peak fluorescence intensities for 3- and 5- layer particles are also plotted for comparison.

We attempted achieve this state by simply wrapping the 3- and 5- layer particles in an additional PSS layer deposited at pH 8.4. As can be seen in Figure 3.16, the resulting 4- and 6- layer particles showed almost no fluorescence. This disappearance of the fluorescence may result from the removal of the PAH-RGCS dyes during the deposition of the final PSS layer, possibly because it may be more favorable to form free aggregates of PSS and PAH-RGCS than to deposit a PSS layer onto the PAH-RGCS terminated particles. It is therefore clear that other methods for obtaining non-flocculating particles are needed.

It is interesting that the fluorescence intensity exhibits so little hysteresis under pH cycling. This result is not consistent with previous studies on flat substrates where a larger hysteresis was observed when the number of polymer layers was greater than one. On flat substrates, the unpaired amine groups in PAH/PSS PEM films form hydrophobic domains at high ambient pH. One might expect that the films should start to reswell again once the ambient pH is lowered from the higher values, but due to the tight binding of the hydrophobic domains, the films do not swell until much lower ambient pH is achieved, resulting in hysteresis.

In this experiment, we work with small particles with high curvature and limited surface area, and it is possible that this geometry disrupts the formation of the hydrophobic domains minimizing the hysteresis. We currently do not understand the mechanisms that accomplishes this, but it is a good candidate for future work.

3.3.6 pH-dependent extinction properties of the 5-, 7-, and 9-layer particles

The right column of Figure 3.15 plots what I will call the normalized extinction ratios for the 3-, 5-, 7-, and 9- layer particles, as the pH was cycled. This ratio is defined as the difference in extinction at the resonance wavelength and at 900 nm wavelength, and shows strong hysteresis when the ambient pH was varied cyclically as shown in Figure 3.15 (b), (d), (f), and (h). As we have already discussed, the particles tend to flocculate at high pH and disperse at low pH. This causes a broadening of the plasmon peak and consequently a lowering in the normalized extinction ratio at high pH. When the ambient pH was raised, at

intermediate pH it may take up to several hours before complete flocculation occurs, even though the particles become unstable at a relatively low pH. However, the time for raising the ambient pH was much shorter (~5-10 min), so we do not observe the change from the redispersion state to the flocculation state until a higher pH was reached, where flocculation occurs much more rapidly. In other words, the time scale for particle flocculation is slow on the experimental time scale as shown in Figure 3.15 (b), (d), and (h). However, if we raised the ambient pH over a longer time such that the particles start flocculating, a drop in the normalized extinction ratio is observed around as can be seen in Figure 3.15 (f). The same reasoning also applies when the ambient pH was lowered because the amines, at intermediate pH, may take up to several hours to regain their full charge, and make the particles redisperse. However, the experimental time scale is again much shorter than the time before particles completely redisperse in the medium. The net result of this is a hysteresis loop in the extinction ratio, even though we observe very little hysteresis in the fluorescence. Finally, it is worth mentioning that because some particles aggregate irreversibly at the higher pH, not all particles will fully redisperse when the pH is lowered again, which explains why the hysteresis loop is open rather than closed.

It is interesting that strong hysteresis is observed in the normalized extinction ratios but does not appear to affect the fluorescence intensity even though the PAH film swells and deswells when the ambient pH was varied. We can attribute this to the optical responses of Au NPs and Au NP dimers. At high pH, the particles tend to flocculate. For instance, it is possible that two particles couple as a dimer and create a new plasmonic mode in its gap, which is known as the “gap plasmon mode”. This new plasmonic mode provides a strong electric field enhancement at long wavelengths, outside the excitation wavelength of the fluorophores. The area over which this enhancement occurs is also just a small fraction of the particle surface area. Therefore, most dye molecules are unaffected by the gap plasmon as they are located outside of the high intensity regions. The small amount of dyes that lie near the gap of the dimer where the gap plasmon is strong are also mostly unaffected by it due to the lack of spectral overlap. The overall effect is that the relation between

the fluorescence intensity and the ambient pH is quite independent of the flocculation state or the extinction spectrum.

3.4 Conclusions

A system of RGCS fluorophores conjugated to Au NPs with a tunable polymer spacer has been developed. The distance between the surface of the Au NPs and the fluorophores was varied by changing the ambient pH of the combined colloidal system utilizing a property of PAH-rich PEMs. At low pH, these films swell such that fluorophores are pushed away from the LSPR field, resulting in a decrease in the fluorescence intensity. At high pH, on the other hand, the polymer shrinks in such a way that the fluorophores are pulled towards the Au NPs and interact more strongly with the LSPR field, causing an increase in fluorescence intensity.

The relationship between the fluorescence intensity and the pH of the suspension is nearly linear with low hysteresis tuning of fluorescence intensity. Such behavior is very favorable for sensing applications where we can integrate the swelling and deswelling property of the PAH-rich PEMs to the fluorescence emission of the fluorophores. This suggests particles such as those can be used for quantitative optical detection of pH and other quantities at a microscopic level, which may be useful in biomedical and environmental research.

3.5 References

[1] K. Aslan, I. Gryczynski, J. Malicka, E. Matveeva, J.R. Lakowicz, C.D. Geddes, Metal-enhanced fluorescence: an emerging tool in biotechnology, Current Opinion in Biotechnology, 16 (2005) 55-62.

[2] N.N. Horimoto, K. Imura, H. Okamoto, Dye fluorescence enhancement and quenching by gold nanoparticles: Direct near-field microscopic observation of shape dependence, Chemical Physics Letters, 467 (2008) 105-109.

[3] L. Bujak, M. Olejnik, T.H.P. Brotosudarmo, M.K. Schmidt, N. Czechowski, D. Piatkowski, J. Aizpurua, R.J. Cogdell, W. Heiss, S. Mackowski, Polarization control of metal-enhanced fluorescence in hybrid assemblies of photosynthetic complexes and gold nanorods, Physical Chemistry Chemical Physics, 16 (2014) 9015-9022.

[4] P. Reineck, D. Gómez, S.H. Ng, M. Karg, T. Bell, P. Mulvaney, U. Bach, Distance and Wavelength Dependent Quenching of Molecular Fluorescence by Au@SiO2 Core–Shell Nanoparticles, ACS Nano, 7 (2013) 6636-6648.

[5] Y. Zhang, A. Dragan, C.D. Geddes, Wavelength Dependence of Metal-Enhanced Fluorescence, The Journal of Physical Chemistry C, 113 (2009) 12095-12100.

[6] R.R. Ujjwal, C. Sona, S. Debnath, P.N. Yadav, U. Ojha, Dye-Labeled Polyacryloyl Hydrazide–Ag Nanoparticle Fluorescent Probe for Ultrasensitive and Selective Detection of Au Ion, ACS Omega, 2 (2017) 4278-4286.

[7] S. Yuan, F. Ge, Y. Chen, Z. Cai, Tunable metal-enhanced fluorescence by pH-responsive polyacryloyl hydrazide capped Ag nanoparticles, RSC Advances, 7 (2017) 6358-6363.

[8] V. Garg, B.S. Sengar, V. Awasthi, Aaryashree, P. Sharma, C. Mukherjee, S. Kumar, S. Mukherjee, Localized surface plasmon resonance on Au nanoparticles: tuning and exploitation for performance enhancement in ultrathin photovoltaics, RSC Advances, 6 (2016) 26216-26226.

[9] K.L. Kelly, E. Coronado, L.L. Zhao, G.C. Schatz, The Optical Properties of Metal Nanoparticles: The Influence of Size, Shape, and Dielectric Environment, The Journal of Physical Chemistry B, 107 (2003) 668-677.

[10] S. Link, M.A. El-Sayed, Size and Temperature Dependence of the Plasmon Absorption of Colloidal Gold Nanoparticles, The Journal of Physical Chemistry B, 103 (1999) 4212-4217.

[11] P. Mulvaney, Surface Plasmon Spectroscopy of Nanosized Metal Particles, Langmuir, 12 (1996) 788-800.

[12] C. Noguez, Surface Plasmons on Metal Nanoparticles: The Influence of Shape and Physical Environment, The Journal of Physical Chemistry C, 111 (2007) 3806-3819.

[13] I.O. Sosa, C. Noguez, R.G. Barrera, Optical Properties of Metal Nanoparticles with Arbitrary Shapes, The Journal of Physical Chemistry B, 107 (2003) 6269-6275.

[14] A.L. Feng, M.L. You, L. Tian, S. Singamaneni, M. Liu, Z. Duan, T.J. Lu, F. Xu, M. Lin, Distance-Dependent Plasmon-Enhanced Fluorescence of Upconversion Nanoparticles using Polyelectrolyte Multilayers as Tunable Spacers, Scientific Reports, 5 (2015) 7779.

[15] J. Chen, Y. Jin, N. Fahruddin, J.X. Zhao, Development of Gold Nanoparticle-Enhanced Fluorescent Nanocomposites, Langmuir, 29 (2013) 1584-1591.

[16] R. Duan, C. Li, S. Liu, Z. Liu, Y. Li, J. Zhu, X. Hu, A selective fluorescence quenching method for the determination of trace hypochlorite in water samples with nile blue A, Journal of the Taiwan Institute of Chemical Engineers, 50 (2015) 43-48.

[17] B. Dubertret, M. Calame, A.J. Libchaber, Single-mismatch detection using gold-quenched fluorescent oligonucleotides, Nat Biotech, 19 (2001) 365-370.

[18] E. Dulkeith, A.C. Morteani, T. Niedereichholz, T.A. Klar, J. Feldmann, S.A. Levi, F.C.J.M. van Veggel, D.N. Reinhoudt, M. Möller, D.I. Gittins, Fluorescence Quenching of Dye Molecules near Gold Nanoparticles: Radiative and Nonradiative Effects, Physical Review Letters, 89 (2002) 203002.

[19] H. Li, R. Liang, D.H. Turner, L.J. Rothberg, S. Duan, Selective quenching of fluorescence from unbound oligonucleotides by gold nanoparticles as a probe of RNA structure, RNA, 13 (2007) 2034-2041.

[20] Y. Tu, P. Wu, H. Zhang, C. Cai, Fluorescence quenching of gold nanoparticles integrating with a conformation-switched hairpin oligonucleotide probe for microRNA detection, Chemical Communications, 48 (2012) 10718-10720.

[21] H. Iwase, D. Englund, J. Vučković, Analysis of the Purcell effect in photonic and plasmonic crystals with losses, Opt. Express, 18 (2010) 16546-16560.

[22] M. Bauch, K. Toma, M. Toma, Q. Zhang, J. Dostalek, Plasmon-Enhanced Fluorescence Biosensors: a Review, Plasmonics, 9 (2014) 781-799.

[23] P. Bharadwaj, L. Novotny, Spectral dependence of single molecule fluorescence enhancement, Optics Express, 15 (2007) 14266-14274.

[24] J. Dong, Z. Zhang, H. Zheng, M. Sun, Recent Progress on Plasmon-Enhanced Fluorescence, Nanophotonics, 2015, pp. 472.

[25] K.H. Drexhage, Influence of a dielectric interface on fluorescence decay time, Journal of Luminescence, 1 (1970) 693-701.

[26] W. Jianting, M. Joseph, L. Sebastien, N. Michael, A. Samuel, A.K. Kyung, Fluorophore–gold nanoparticle complex for sensitive optical biosensing and imaging, Nanotechnology, 23 (2012) 095501.

[27] M. Li, S.K. Cushing, N. Wu, Plasmon-enhanced optical sensors: a review, Analyst, 140 (2015) 386-406.

[28] G. Schneider, G. Decher, N. Nerambourg, R. Praho, M.H.V. Werts, M. Blanchard-Desce, Distance-Dependent Fluorescence Quenching on Gold Nanoparticles Ensheathed with Layer-by-Layer Assembled Polyelectrolytes, Nano Letters, 6 (2006) 530-536.

[29] N.S. Abadeer, M.R. Brennan, W.L. Wilson, C.J. Murphy, Distance and Plasmon Wavelength Dependent Fluorescence of Molecules Bound to Silica-Coated Gold Nanorods, ACS Nano, 8 (2014) 8392-8406.

[30] G. Colas des Francs, A. Bouhelier, E. Finot, J.C. Weeber, A. Dereux, C. Girard, E. Dujardin, Fluorescence relaxation in the near-field of a mesoscopic metallic particle: distance dependence and role of plasmon modes, Optics Express, 16 (2008) 17654-17666.

[31] F. Emmanuel, G. Samuel, Surface enhanced fluorescence, Journal of Physics D: Applied Physics, 41 (2008) 013001.

[32] J.B. Khurgin, G. Sun, Impact of surface collisions on enhancement and quenching of the luminescence near the metal nanoparticles, Optics Express, 23 (2015) 30739-30748.

[33] A. Kinkhabwala, Z. Yu, S. Fan, Y. Avlasevich, K. Mullen, W.E. Moerner, Large single-molecule fluorescence enhancements produced by a bowtie nanoantenna, Nat Photon, 3 (2009) 654-657.

[34] J.R. Lakowicz, Radiative decay engineering 5: metal-enhanced fluorescence and plasmon emission, Analytical biochemistry, 337 (2005) 171-194.

[35] J.R. Lakowicz, K. Ray, M. Chowdhury, H. Szmacinski, Y. Fu, J. Zhang, K. Nowaczyk, Plasmon-controlled fluorescence: a new paradigm in fluorescence spectroscopy, Analyst, 133 (2008) 1308-1346.

[36] M.-X. Li, W. Zhao, G.-S. Qian, Q.-M. Feng, J.-J. Xu, H.-Y. Chen, Distance mediated electrochemiluminescence enhancement of CdS thin films induced by the plasmon coupling of gold nanoparticle dimers, Chemical Communications, 52 (2016) 14230-14233.

[37] H. Mertens, A.F. Koenderink, A. Polman, Plasmon-enhanced luminescence near noble-metal nanospheres: Comparison of exact theory and an improved Gersten and Nitzan model, Physical Review B, 76 (2007) 115123.

[38] K.H. Drexhage, IV Interaction of Light with Monomolecular Dye Layers, in: E. Wolf (Ed.) Progress in Optics, Elsevier1974, pp. 163-232.

[39] R.R. Chance, A. Prock, R. Silbey, Molecular Fluorescence and Energy Transfer Near Interfaces.

[40] R.R. Chance, A.H. Miller, A. Prock, R. Silbey, Fluorescence and energy transfer near interfaces: The complete and quantitative description of the Eu+3/mirror systems, The Journal of Chemical Physics, 63 (1975) 1589-1595.

[41] D. Cheng, Q.-H. Xu, Separation distance dependent fluorescence enhancement of fluorescein isothiocyanate by silver nanoparticles, Chemical Communications, DOI 10.1039/B612401A(2007) 248-250.

[42] X. Zhang, C.A. Marocico, M. Lunz, V.A. Gerard, Y.K. Gun'ko, V. Lesnyak, N. Gaponik, A.S. Susha, A.L. Rogach, A.L. Bradley, Experimental and Theoretical Investigation of the Distance Dependence of Localized Surface Plasmon Coupled Förster Resonance Energy Transfer, ACS Nano, 8 (2014) 1273-1283.

[43] K. Chen, H.D. Robinson, Robust dithiocarbamate-anchored amine functionalization of Au nanoparticles, Journal of Nanoparticle Research, 13 (2011) 751-761.

[44] P.M. Whitmore, H.J. Robota, C.B. Harris, Mechanisms for electronic energy transfer between molecules and metal surfaces: A comparison of silver and nickel, The Journal of Chemical Physics, 77 (1982) 1560-1568.

[45] A. Wokaun, H.P. Lutz, A.P. King, U.P. Wild, R.R. Ernst, Energy transfer in surface enhanced luminescence, The Journal of Chemical Physics, 79 (1983) 509-514.

[46] K.A. Kang, J. Wang, J.B. Jasinski, S. Achilefu, Fluorescence Manipulation by Gold Nanoparticles: From Complete Quenching to Extensive Enhancement, Journal of Nanobiotechnology, 9 (2011) 16.

[47] M.A.C. Stuart, W.T.S. Huck, J. Genzer, M. Müller, C. Ober, M. Stamm, G.B. Sukhorukov, I. Szleifer, V.V. Tsukruk, M. Urban, F. Winnik, S. Zauscher, I. Luzinov, S. Minko, Emerging applications of stimuli-responsive polymer materials, Nature Materials, 9 (2010) 101.

[48] M. Wei, Y. Gao, X. Li, M.J. Serpe, Stimuli-responsive polymers and their applications, Polymer Chemistry, 8 (2017) 127-143.

[49] B.e. Lv, Y. Zhou, W. Cha, Y. Wu, J. Hu, L. Li, L. Chi, H. Ma, Molecular Composition, Grafting Density and Film Area Affect the Swelling-Induced Au–S Bond Breakage, ACS Applied Materials & Interfaces, 6 (2014) 8313-8319.

[50] Z. Liu, Y. Guo, K. Inomata, Reversible thermoresponsive behavior of poly(2-chloroethyl vinyl ether-alt-maleic anhydride) in mixed solvent of tetrahydrofuran/hexane, Colloid and Polymer Science, 289 (2011) 791-798.

[51] F. Zhou, P.M. Biesheuvel, E.-Y. Choi, W. Shu, R. Poetes, U. Steiner, W.T.S. Huck, Polyelectrolyte Brush Amplified Electroactuation of Microcantilevers, Nano Letters, 8 (2008) 725-730.

[52] M.P. Weir, S.Y. Heriot, S.J. Martin, A.J. Parnell, S.A. Holt, J.R.P. Webster, R.A.L. Jones, Voltage-Induced Swelling and Deswelling of Weak Polybase Brushes, Langmuir, 27 (2011) 11000-11007.

[53] G. Migliorini, On the Corrections to Strong-Stretching Theory for End-Confined, Charged Polymers in a Uniform Electric Field, Macromolecules, 43 (2010) 9168-9180.

[54] J. Thevenot, H. Oliveira, O. Sandre, S. Lecommandoux, Magnetic responsive polymer composite materials, Chemical Society Reviews, 42 (2013) 7099-7116.

[55] D.A. Davis, A. Hamilton, J. Yang, L.D. Cremar, D. Van Gough, S.L. Potisek, M.T. Ong, P.V. Braun, T.J. Martínez, S.R. White, J.S. Moore, N.R. Sottos, Force-induced activation of covalent bonds in mechanoresponsive polymeric materials, Nature, 459 (2009) 68.

[56] R.T. Hill, K.M. Kozek, A. Hucknall, D.R. Smith, A. Chilkoti, Nanoparticle–Film Plasmon Ruler Interrogated with Transmission Visible Spectroscopy, ACS Photonics, 1 (2014) 974-984.

[57] J.A. Hiller, M.F. Rubner, Reversible Molecular Memory and pH-Switchable Swelling Transitions in Polyelectrolyte Multilayers, Macromolecules, 36 (2003) 4078-4083.

[58] K. Itano, J. Choi, M.F. Rubner, Mechanism of the pH-Induced Discontinuous Swelling/Deswelling Transitions of Poly(allylamine hydrochloride)-Containing Polyelectrolyte Multilayer Films, Macromolecules, 38 (2005) 3450-3460.

[59] N. Parveen, M. Schönhoff, Swelling and Stability of Polyelectrolyte Multilayers in Ionic Liquid Solutions, Macromolecules, 46 (2013) 7880-7888.

[60] A. Kumar, R.R. Ujjwal, A. Mittal, A. Bansal, U. Ojha, Polyacryloyl Hydrazide: An Efficient, Simple, and Cost Effective Precursor to a Range of Functional Materials through Hydrazide Based Click Reactions, ACS Applied Materials & Interfaces, 6 (2014) 1855-1865.

[61] S.E. Burke, C.J. Barrett, Acid−Base Equilibria of Weak Polyelectrolytes in Multilayer Thin Films, Langmuir, 19 (2003) 3297-3303.

[62] J. Choi, M.F. Rubner, Influence of the Degree of Ionization on Weak Polyelectrolyte Multilayer Assembly, Macromolecules, 38 (2005) 116-124.

[63] Y. Hama, Y. Urano, Y. Koyama, M. Bernardo, P.L. Choyke, H. Kobayashi, A Comparison of the Emission Efficiency of Four Common Green Fluorescence Dyes after Internalization into Cancer Cells, Bioconjugate Chemistry, 17 (2006) 1426-1431.

[64] G. Frens, Controlled Nucleation for the Regulation of the Particle Size in Monodisperse Gold Suspensions, Nature, 241 (1973) 20-22.

[65] J. Turkevich, P.C. Stevenson, J. Hillier, A study of the nucleation and growth processes in the synthesis of colloidal gold, Discussions of the Faraday Society, 11 (1951) 55-75.

[66] I. Ashry, B. Zhang, M.B. Khalifa, J.A. Calderone, W.L. Santos, J.R. Heflin, H.D. Robinson, Y. Xu, Fluorescence lifetime based characterization of active and tunable plasmonic nanostructures, Optics Express, 22 (2014) 20720-20726.

[67] O.M. Tanchak, C.J. Barrett, Swelling Dynamics of Multilayer Films of Weak Polyelectrolytes, Chemistry of Materials, 16 (2004) 2734-2739.

[68] P.B. Johnson, R.W. Christy, Optical Constants of the Noble Metals, Physical Review B, 6 (1972) 4370-4379.

[69] X. Miao, I. Brener, T.S. Luk, Nanocomposite plasmonic fluorescence emitters with core/shell configurations, J. Opt. Soc. Am. B, 27 (2010) 1561-1570.

[70] A. Polemi, K.L. Shuford, Distance dependent quenching effect in nanoparticle dimers, The Journal of Chemical Physics, 136 (2012) 184703.

[71] G.K. Christopher, J.N. Stephen, V.-D. Tuan, Investigating the plasmonics of a dipole-excited silver nanoshell: Mie theory versus finite element method, Nanotechnology, 21 (2010) 315203.

[72] K.Q. Le, Nanoplasmonic Enhancement of Molecular Fluorescence: Theory and Numerical Modeling, Plasmonics, 10 (2015) 475-482.

[73] V. Giannini, A.I. Fernández-Domínguez, S.C. Heck, S.A. Maier, Plasmonic Nanoantennas: Fundamentals and Their Use in Controlling the Radiative Properties of Nanoemitters, Chemical Reviews, 111 (2011) 3888-3912.

[74] S. Kühn, U. Håkanson, L. Rogobete, V. Sandoghdar, Enhancement of Single-Molecule Fluorescence Using a Gold Nanoparticle as an Optical Nanoantenna, Physical Review Letters, 97 (2006) 017402.

Chapter 4 Optically aligned assembly of gold nanospheres

This chapter discusses the assembly of nanoparticles (NPs) into larger nanostructures. Specifically, I will describe an attempt to bind one type of NPs to another type to form more complex ordered and aligned aggregates. This chapter starts with an overview of recent literature on NP assembly. Properties of the photocleavable molecule used in the experiment are outlined. Next, a specific technique for building dimers of gold nanospheres (Au NSs) is introduced, followed by a discussion of the experiment as well as preliminary results. Finally, interesting results and possible future work are outlined.

4.1 Introduction

One of the chief objectives in nanoscience is to produce a small-sized architecture for novel nanodevices and nanoscale electronics. To reach this goal, well-ordered structures consisting of multiple NPs, each of which can serve a specific purpose, is an important direction to perform a multifunctional task. Metallic nanoparticles (MNPs) are particularly interesting for constructing such complex ordered nanostructures on account of their multiple useful features. In addition, many MNPs syntheses are well-established and straightforward to perform [1-3]. The particles' optical, electrical, and magnetic properties can also be tailored by modulating their size, shape and surface chemistry [4-6]. Despite the rich variety of shapes and morphologies of available NPs [1-3, 7-10], it remains a challenge to organize them into well-defined ordered structures. Were this proposition fully realized, it would open new vistas in optoelectronic devices, in new material designs, and in medical applications.

The literature contains attempts at self-assembly of NPs ranging from very simplest (e.g. dimer) to fairly complex arrangement intended for different applications [11-19]. For example, Lee et al. fabricated high-yield heterodimers from gold nanocubes (Au NCs) and Au nanospheres (NSs), which were covalently bonded using 1, 8-octanedithiols. Au NSs were attached to the vertices of Au NCs where a nanogap between these two types of NPs provides a strong localized electric field enhancement, which is helpful in surface-enhanced Raman scattering (SERS) [15]. Kou et al. successfully assembled three types of gold nanostructures: Au NCs to Au NCs, Au NCs to Au NSs and gold nanobranches and Au NSs. They used glutathiones as linkers, and showed that these particles were preferentially bonded at the edges rather than a planar surface [14]. Chou et al. employed linker DNA strands with complementary sequences to join surface-modified MNPs with a single-stranded DNA to form core-satellite nanostructures, where a core NP, whose size is around 6 nm, is surrounded by satellite NPs with an appropriate surface functionality for ligand binding [12]. Wang et al. created side-by-side and end-to-end gold nanorods using antigen-antibody as linkers for sensing toxin in the environment [49]. Lee at al. assembled nanowires to form a molecular spring structure with poly(ethylenegylcol) as a linker to a protein-sensitive sensor [50]. Mastroianni et al. fabricated a pyramidal nanostructure from gold nanocrystals using DNA scaffolds for the construction of chiral nanostructures [51].

There is another interesting type of nanoassembly known as an "orientational assembly", where NPs are arranged in a specific orientation to form larger scale structure in one or two dimensions. Wu et al. assembled silver (Ag) NPs and Au NPs to form heterodimers using antigen-antibody as linkers. Such larger structure can be further used as a plasmonic sensor, which can identify heavy metals (e.g. Hg^{2+}, Ag^{+}) [20]. Vertically oriented Au NPs dimers made using thiol-PEG molecules as linkers were also reported by Guo et al., who demonstrated their use as a colorimetric sensor to monitor DNA isolated from foodborne pathogens [21]. Plasmon rulers made of Au NPs dimers were also addressed by Chen et al. for the characterization of the distance between the particles [22]. Other regiospecific structures, including Au NPs

trimers [23], Janus (two-faced) clusters [24], and alternating particle chains [25], have also reported with numerous potential applications.

Here, an oriented assembly of well-defined Au NS dimers is proposed. Specifically, Au NSs of two different diameters (~14 nm and ~60 nm) were used, and a photocleavable molecule was use as the linker. This molecule, which we will denote LIP3, consists of a thiol anchor group and a photoreactive group connected by a short alkane chain. The photosensitive group reveals a primary amine group upon absorption of a photon, which in turn protonates into a positively-charged reactive group at suitable pH. The larger Au NSs with photocleaved LIP3 were then incubated in small Au NSs suspension. Finally, negatively charged small Au NSs can be aligned onto large Au NSs by the polarization of ultraviolet (UV) light as illustrated in Figure 4.1 (a). This method differs from previously published work in that the shape of NPs used in this dissertation is isotropic, but the assembly is controlled by an anisotropic external force, specifically linearly polarized UV light. The UV light creates dipolar patches of photocleavable ligands on the larger NSs, inducing smaller Au NPs to bind in the center of the patches. The result is the assemblies that are aligned with the polarization of the exposing UV light.

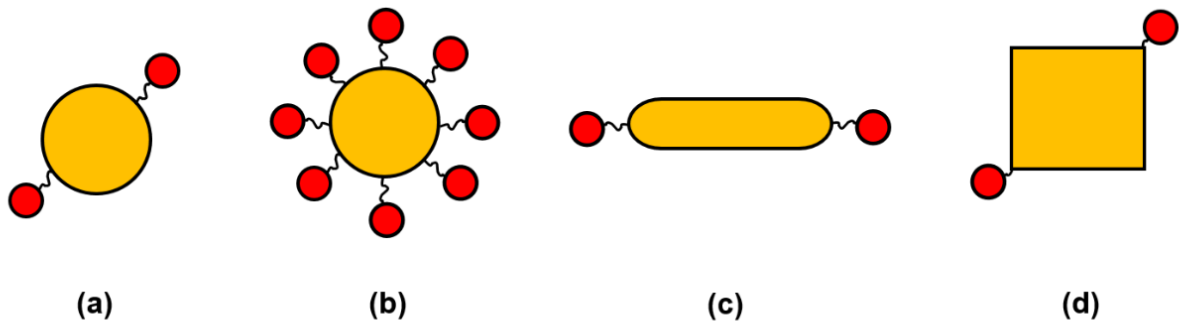

Figure 4.1: Schematic representation of ordered nanostructures assembled from MNPs as the building blocks. (a) a nanoparticle trimer with a specific orientation, (b) a core-satellite nanostructure, (c) a nanorod-nanosphere dumbell and (d) a nanocube-nanosphere trimer.

4.2 LIP3: A photocleavable molecule

The photocleavable molecule 1-(6-Nitrobenzo[d][1,3]dioxol-5-yl)ethyl (4-(1,2-Dithiolan-3-yl)butyl) carbamate was used as a linker between NPs in the experiment. Its molecular structure and synthesis route are shown in Figure 4.2 In this dissertation, this molecule will be denoted as "LIP3" [28]. LIP3 is synthesized from two precursors: (1) lipoic acid (or DL-thioctic acid) and (2) 1-(6-Nitrobenzo[d][1,3]dioxol-5-yl)ethanol, as *o*-nitrobenzyl derivative. The lipoic acid moiety exhibits a disulfide group which is capable of tight binding to metallic surfaces or NPs [29-31]. The *o*-nitrobenzyl derivative is a photocleavable molecule, and after it is activated by UV irradiation, this functional group cleaves off and leaves behind a positively-charged primary amine group as shown in Figure 4.3 [32-34]. [*The synthesis was performed by Ashley Gates from Dr.Webster Santos's group, Chemistry department, Virginia Tech.*]

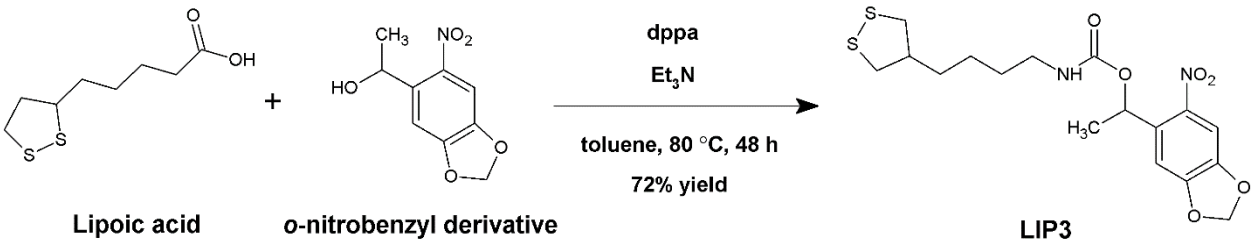

Figure 4.2: Synthesis of the photolabile protecting ligand LIP3. See Reference [28] for details.

Daengngam et al. showed that LIP3 undergoes selective bond cleavage upon irradiation with UV light at 365 nm wavelength. It decomposes into (1) a surface-bound lipoic acid derivative presenting a primary amine ($-NH_2$) group, (2) a nitroso leaving group, and (3) carbon dioxide (Figure 4.3) [28].

Before UV exposure, the characteristic absorption peak of 40 μM LIP3 in ethanol (C_2H_5OH) is around 340 nm. This absorption peak then shifts to 378 nm after UV irradiation (see Figure 4.4). In this dissertation, there are two primary UV sources used in the experiment. The first UV light source is a

UV Crosslinker (FB-UVXL-1000, Fisher Scientific), which provides 365-nm UV light with an average power 2.4 mW (or the corresponding power density 3.06 mW/cm^2 because the beam diameter is 1 cm).

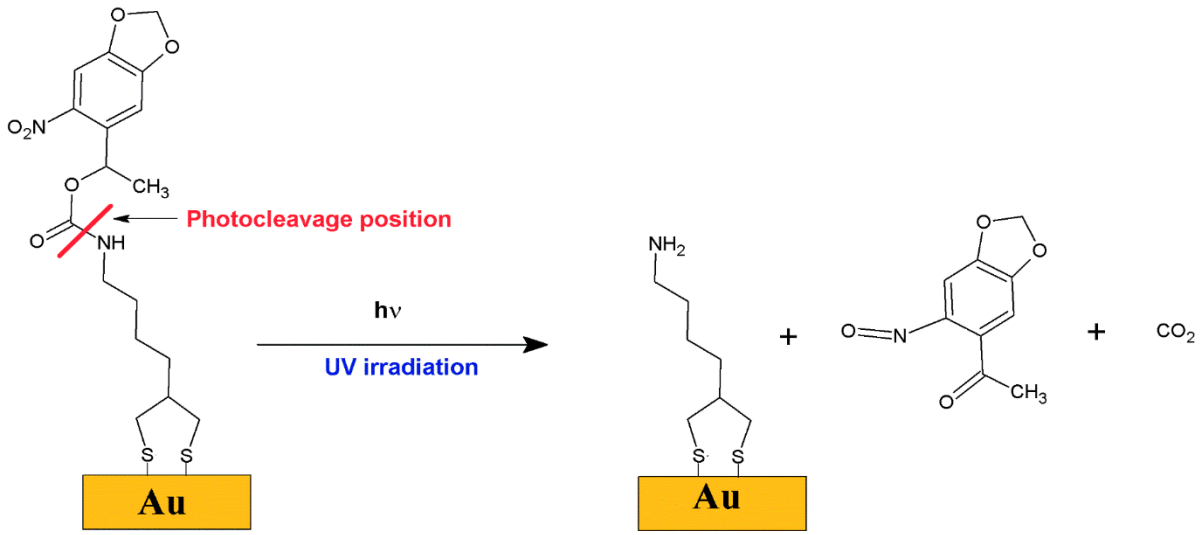

Figure 4.3: The pathway of a photouncaging LIP3 into three products upon irradiation with UV-light at 365 nm wavelength. The red line shows where the molecule cleaves, leaving a primary amine group for nanoparticle binding under suitable conditions.

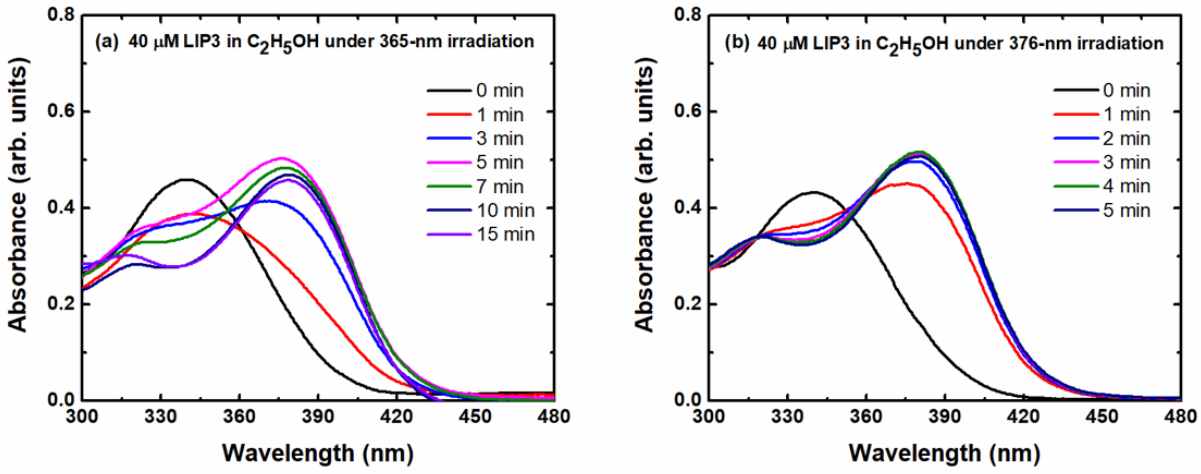

Figure 4.4: The absorption spectra of 40 μM LIP3 in ethanol and its decomposition under (a) 365-nm and (b) 376-nm UV irradiation.

The second light source is a collimated 376-nm UV laser beam (Stradus® 375-60, Vortran Laser Technology, Inc.). The power delivered by the laser can be controlled from 0 to 60 mW. Figure 4.4 (b) shows changes in the absorption spectrum of 40 μM LIP3 in ethanol upon exposed to 376-nm UV after passing through a beam expander. The beam diameter was here and in the other experiment enlarged from 1.2 mm to 1.0 cm, so an average power of 2.1 mW corresponds to a power density of 2.67 mW/cm^2. In spite of the lower light flux, the rate of LIP3 decomposition is faster under laser illumination than in the crosslinker.

The results from LIP3 in solution can be used as a guide for the assembly of Au NSs facilitated by LIP3 clevage. Nevertheless, the decomposition rate of LIP3 immobilized on the surface of a metal (e.g. Ag or Au) in air may be different from that in solution. In addition, the metal film may reflect UV light or generate heat, which also has an impact on the decomposition rate of LIP3 and the possibility also on the NP binding to the uncaged amines.

4.3 Preliminary results

This section presents certain preliminary results leading up to the actual assembly experiments. These results provide some insight into the mechanisms underlying the assembly, while experimental procedures for the nanoassembly are elaborated in the next section.

4.3.1 The effect of green (550 nm) light

The photouncaging reaction of LIP3 under UV irradiation in Figure 4.3 reveals a primary amine group that bears a positive charge at lower pH (< 6). There are a number of methods to verify the existence of a positive charge of a cleaved LIP3. One convenient way is to observe the adsorption of negatively charged Au NPs on the LIP3-coated substrate. If LIP3 is bound to a surface, exposed to UV light, and incubated in a low pH (5.2 - 6) Au NSs suspension, Au NSs will be adsorbed on the surface due to an electrostatic attraction

between the amine groups and the Au NSs as depicted in Figure 4.7 (a). Due to the striking color of Au colloids, this results in a coloration that is clearly visible to the naked eye. Suppose an area of a metal substrate is separated into two regions: one of them exposed to a sufficient enough dose of UV, while the other is not, and the substrate is incubated in Au colloidal particles. Only the area that is exposed to UV shows appreciable Au NSs adhesion on the surface, which demonstrates the presence of positive charges from the amine groups in cleaved LIP3s as shown in Figure 4.5.

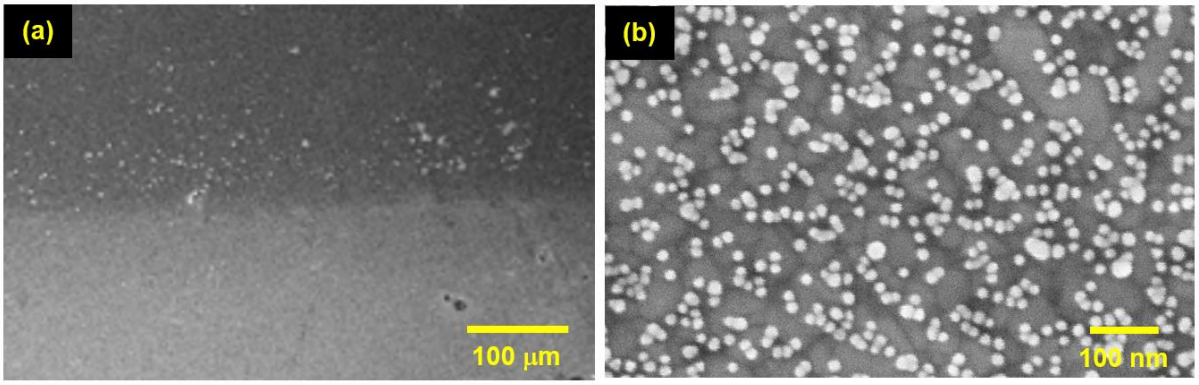

Figure 4.5: FESEM micrographs of a sample consisting of two areas exposed to different doses of UV. (a) The darker area in the upper portion of the image was exposed to a sufficient enough dose of UV, showing the adsorption of Au NSs, while the brighter area was not. (b) The dark area under higher magnification, revealing the presence of small Au NSs as indicated by bright dots.

Au NP adsorption on UV exposed LIP3-terminated surfaces may be inhibited by a 550-nm light irradiation, which corresponds to a green color (cf. Figure 4.6). See et al. observed this photoreaction while studying adhesion of Au NPs onto Ag NPs using LIP3 molecules as linkers. After UV irradiation of LIP3s on Ag NPs, an additional green light exposure can prevent cleaved LIP3 from absorbing negatively charged NPs under low pH condition. This results in a smaller number of Au NPs adsorbed to Ag NPs [27]. The underlying mechanism is still unknown and under investigation. The result is, however, of benefit to our experiment because it can be used to eliminate any non-specific NP bindings after the desired NP assembly has been performed.

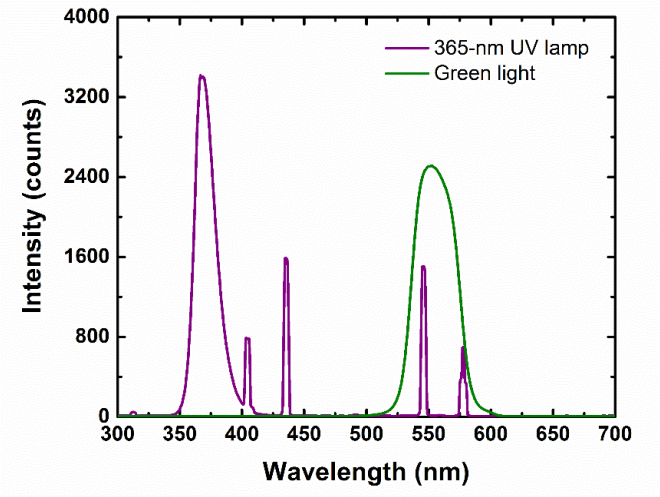

Figure 4.6: Intensity spectra of UV (violet curve) and green (green curve) light sources used in the experiment. The main peak of the UV light source (a UV Crosslinker FB-UVXL-1000, Fisher Scientific) is centered around 365 nm, while that of the green light source is around 550 nm.

4.3.1.1 The effect of green light on LIP3 bound to a planar Au surface

The exposure time of green light on a sample containing LIP3 plays an important role in determining Au NPs binding to Au nanostructures. This section discusses how the surface properties of a sample are changed under green light illumination. The experiment was performed on Au-coated samples with LIP3 bound to the surface, forming what is known as self-assembled monolayers (SAMs). SAMs are highly ordered single layers of molecules that bonds to a solid surface. The samples were then exposed to either green (550 nm) or UV (365 nm) light under different conditions and subsequently incubated in a suspension of 16-nm-sized Au NPs. Finally, the samples were rinsed with nanopure water and dried in a stream of compressed air.

First, Au NPs themselves do not attach onto unbounded Au surfaces because the surface itself is typically negatively charged, thereby repelling the same charges from Au NPs. Consequently, Au NPs binding is not observed on a plain Au surface as shown in Figure 4.7 (a) and (b).

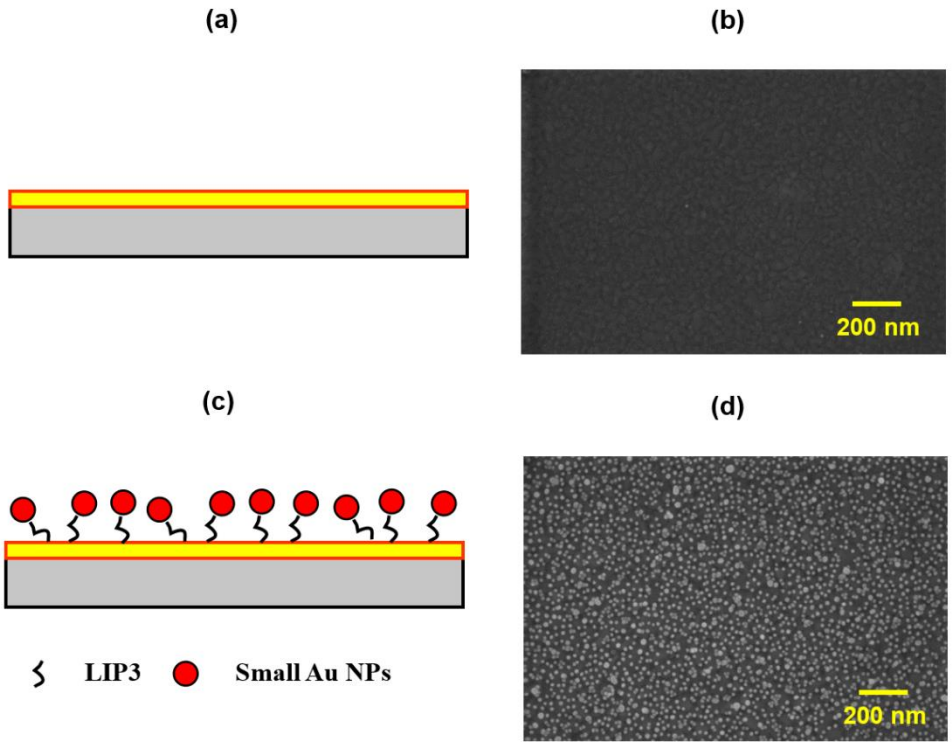

Figure 4.7: (a) Schematic illustration and (b) FESEM image of 100-nm-thick Au film after incubating the substrate in a Au NPs bath for 20 min. It shows no Au NP attachment. (c) Schematic illustration and (d) FESEM image of a SAM of cleaved LIP3 bound to a Au film after incubating the substrate in a Au NPs bath for 20 min. The average diameter of the Au NPs used in this experiment is ~16 nm.

If LIP3 is adsorbed on the surface of a Au film, Au NPs are now capable of being immobilized onto the surface as shown in Figure 4.8 (a), (c), and (d). The attachment of Au NPs on a planar Au surface is observed upon UV illumination as expected in Figure 4.8 (c) and (d). The LIP3 undergoes a photouncaging reaction, and one of the products becomes positively charged due to primary amine groups, attracting the Au NPs. Somewhat surprisingly a sample with no green light or UV treatment shows a similar result in Figure 4.8 (b), although the reason is unknown. It is likely that some fractions of the LIP3 molecules are being cleaved prior to UV exposure, or that there are some contaminations in the LIP3 SAM [35].

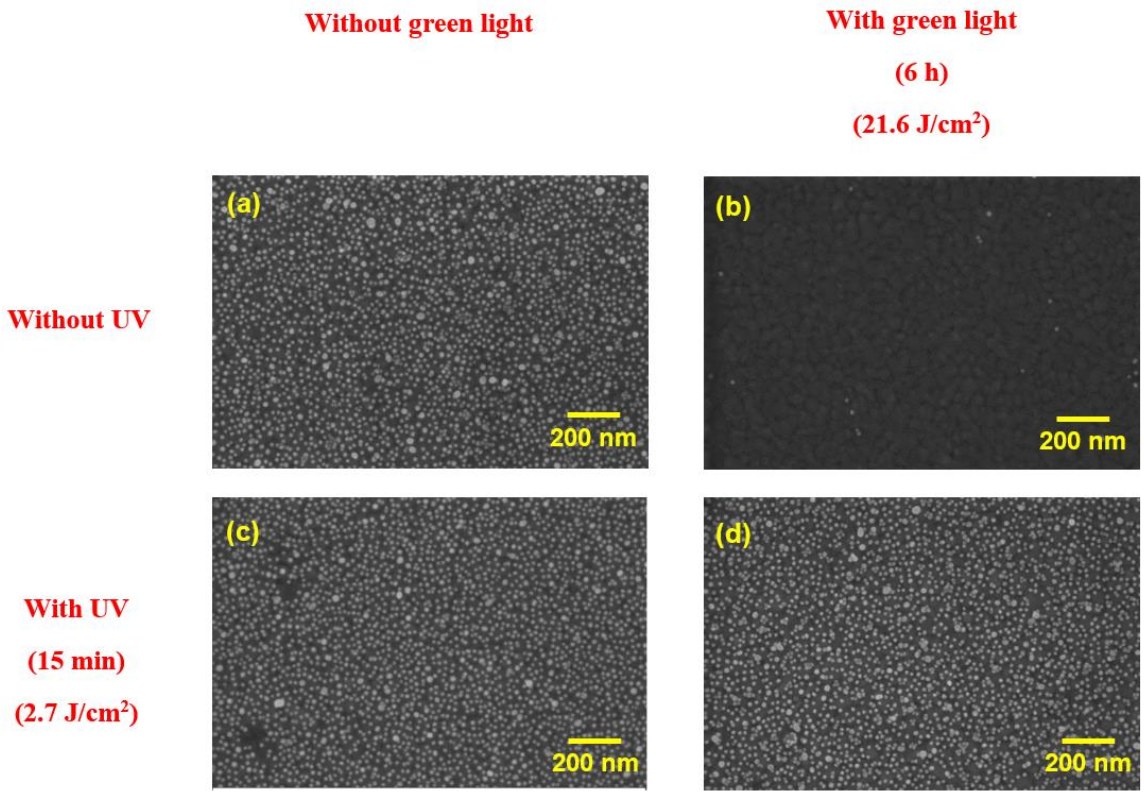

Figure 4.8: FESEM images of samples consisting of 16-nm-diameter Au NPs binding onto LIP3 SAMs on thick Au films. The samples were treated with (a) no light exposure, (b) 6 h green light exposure only, (c) 15 min UV only, and (d) with 6-h green light exposure and followed by 15-min UV. Note that UV treatment was performed as the last step before Au NPs incubation. The incubation time in the Au NPs suspension was 20 min. The green light and UV doses were 21.6 and 2.7 J/cm^2, respectively.

However, if the sample is treated with green light only, Au NPs will not adhere to the surface, as shown in Figure 4.8 (b). This result is similar to the case of planar Au film without LIP3. See et al. hypothesize that this nonbinding may result from a hot-hole-catalyzed reaction that deactivates or removes the existing primary amines from the surface possibly though the formation of azo groups [36, 37]. The green-light-induced photoreaction mechanism will be left as the subject of future work. Another interesting result is illuminated by Figure 4.9. If the dose (or exposure time) of green light is increased on the sample, the number of Au NPs adsorbed on the surface will decrease. In particular, the sample treated with 360 min, which corresponds to a dose of 21.6 J/cm^2 almost show no NP attachment.

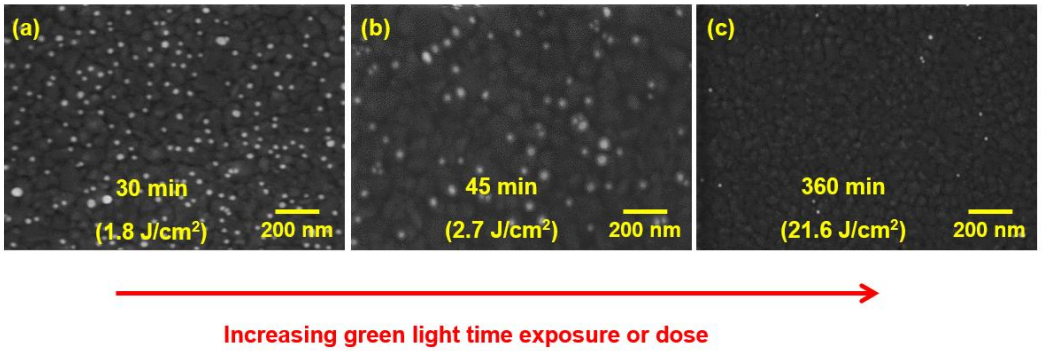

Figure 4.9: FESEM images of Au NPs density binding on LIP3 SAM surfaces under green light illumination with (a) 30 min, (b) 45 min, and (c) 360 min (or 6 h) exposure time. All samples were not exposed to UV light. The following incubation time in Au NPs bath was 20 min.

4.3.1.2 The effect of green light on LIP3 on Au NPs

LIP3 and similar molecules form SAMs not only on flat Au substrates, but also on metal clusters, complexes and NPs [38]. We know that the SAMs formed by LIP3 are of a low to medium density, disordered variety [39, 40]. Here, LIP3s were used to functionalized immobilized spherical Au NPs with nominal diameter around 60 nm. We investigated how small spherical Au NPs with an average diameter about 16 nm adhere to the large Au NSs surface, as illustrated in Figure 4.10 (c) and (d) . As for the flat surface, if the sample consists only of large Au NSs with no SAM layer, small Au NSs will not be able to bind to the large ones owing to an electrostatic repulsion between the two types.

Figure 4.11 shows nanoassembly onto on 60-nm-diameter LIP3-functionalized Au NPs under different light treatments. The results are similar to those for flat Au surfaces (see Figure 4.8). Small Au NSs bind to large Au NSs after the post UV treatment as shown in Figure 4.11 (c) and (d). The Au NPs binding to the particles prior to UV exposure in Figure 4.11 (a) may be attributed to the premature decomposition of LIP3 prior to light exposure. Finally, a reduction in non-specific bindings was observed after green light exposure as shown in Figure 4.11 (b). This result is consistent with the sample with LIP3 on planar Au surface (cf. Figure 4.8 (b)) in that the exposure of a sample to green light may induce a photoreaction, that removes the ability of cleaved LIP3 to bind Au NSs.

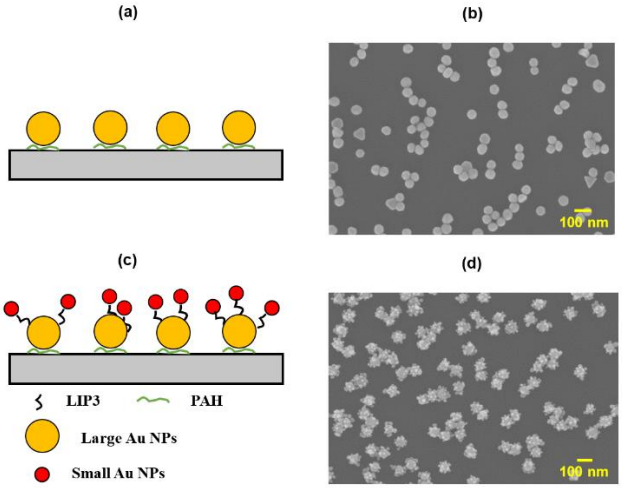

Figure 4.10: (a) Schematic representation and (b) representative FESEM image of 60-nm-sized spherical Au NPs on a glass substrate without LIP3. In this control sample, there is no sign of small spheres adhering to the large ones or to the substrate surface on account of same charge repulsion between the particles. (c) Schematic representation and (d) representative FESEM image of small Au NSs attached to larger Au NSs bound to a glass substrate. The large Au NSs were immobilized using positively-charged polymer PAH.

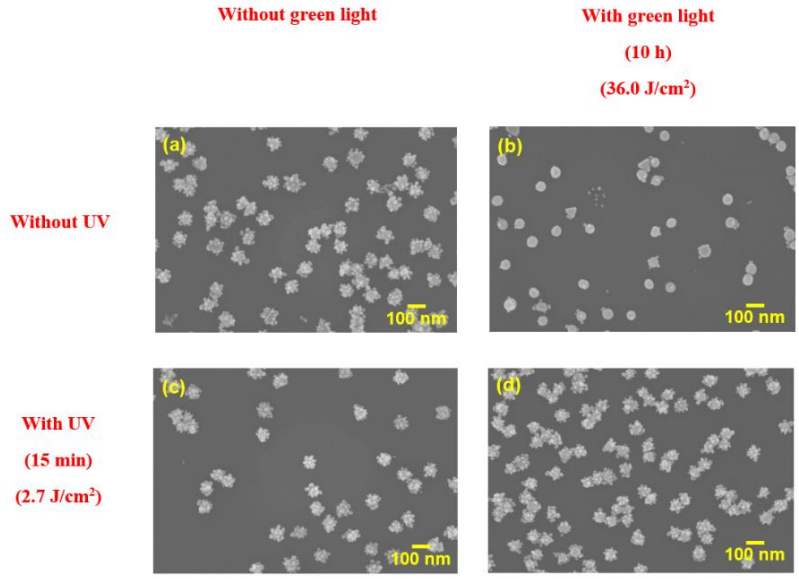

Figure 4.11: FESEM micrographs of small Au NSs adhesion on large Au NSs bound to a glass substrate. The samples were treated with (a) no light exposure, (b) 10 h green light exposure only, (c) 15 min UV only, and (d) 10 h green light followed by 15 min UV exposure. All samples were incubated in the 16-nm-diameter Au NPs suspension for 15 min. A significant drop in Au NSs adhesion is apparent in Figure 4.11 (b).

4.3.2 The effect of a contaminant (lipoic acid) on LIP3 SAM properties

It is possible that some contaminants remain after LIP3 synthesis. At small amounts, these cannot be detected by nuclear magnetic resonance (NMR) and may therefore pass unnoticed into the final product. One notable possible contaminants is lipoic acid, which is a precursor to LIP3 in the synthesis (see Figure 4.2). Lipoic acid containing thiol groups that allow it to adhere to gold substrates, and also contains a carboxyl (-COOH) group, which bears the negative charge. Accordingly, if a sample consisting of lipoic acid SAMs on a thick Au film is incubated in a Au NSs suspension, the particles will not be able to bind to the Au film due to electrostatic repulsion between the lipoic acid and the particles.

To test the effect of lipoic acid on the binding properties of the SAM, we performed an experiment similar to that described in section 4.3.1. However, the samples were now submerged into a mixture of LIP3 and different amounts of lipoic acid and then exposed to UV and/or green light. The proportion of these two chemicals was set in terms of a molar ratio, and here I will denote this ratio as a percentage. Note that this percentage describes the deposition solution, but not necessarily the resulting films.

Figure 4.12 shows the adsorption of Au NPs on samples coated with SAMs deposited from solutions with varying ratios of LIP3 to lipoic acid. First, Au NSs do not adhere to any of the substrates deposited with pure lipoic acid (the last row) whether these samples were treated with UV light, green light, or a combination. This is expected because lipoic acid does not have a primary amine functional group that can become positively charged under UV irradiation, but rather carries a negative charge due to its carboxyl group. Second, the samples treated with UV illumination (first column) reveal good adhesion of Au NSs on the surface even with as much as 5% lipoic acid in the LIP3, though the number of Au NSs binding to the SAMs is reduced. Third, the samples that were exposed to green light only (second column) show a reduction of Au NSs adhering to mixed SAMs consisting of LIP3 and lipoic acid, where the density of Au NSs dramatically decreases when 0.5% lipoic acid in the LIP3 was introduced. Furthermore, no Au NSs are bound to green-light-exposed samples with 1% and 5% lipoic acid in the LIP3 mixture. Finally, the samples treated with green light and followed by UV exposure (third column) show the similar results to

those exposed to UV light only. In other words, Au NSs still bind to a mixture of lipoic acid and LIP3 SAMs surface regardless of the percentage (up to 5%) of lipoic acid in the LIP3.

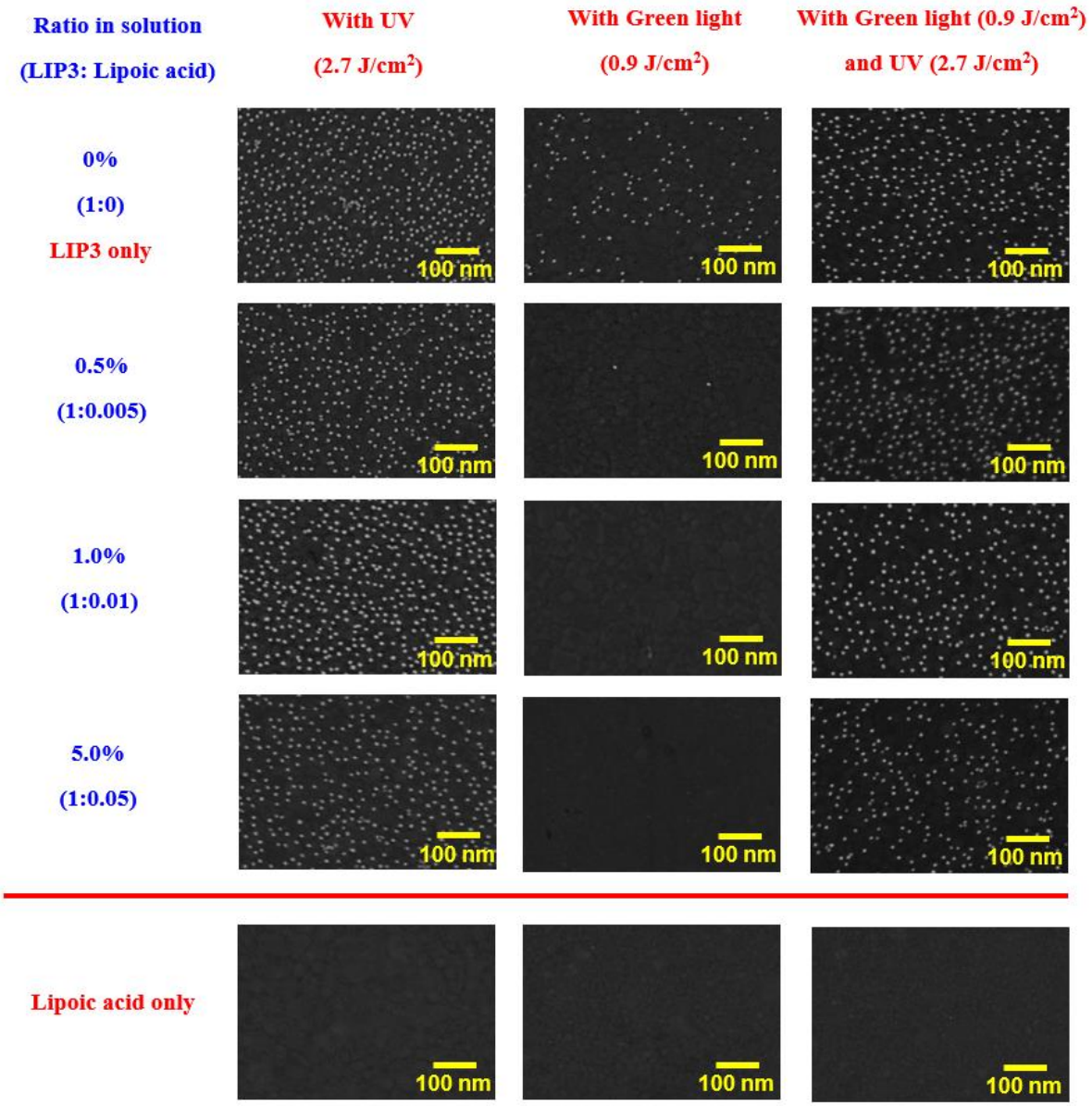

Figure 4.12: FESEM images of the density of Au NSs assembled on mixed SAMs consisting of LIP3 and lipoic acid layers with different amount of lipoic acid and different UV and green irradiation. The bright dots indicate Au NSs adhesion, while the black background is the untreated Au substrates. The ratio in parenthesis is the molar ratio between LIP3 and lipoic acid in the depositing solution.

4.4 Experimental procedures

The Au NSs assembly samples were prepared with the following steps, as illustrated in Figure 4.13.

Step 1 Sample cleaning

Samples were prepared by cutting clear glass slides (Fisher Scientifics precleaned 25 × 75 × 1 mm Plain) into 2.5 × 2.5 cm^2 pieces with a diamond scribe. These substrates were then cleaned by submersion in piranha etch–a 3:1 V/V mixture of conc. H_2SO_4:H_2O_2–for 20 min, followed by rinsing thoroughly with nanopure water 3 times, and finally drying with a stream of dry compressed air.

Step 2 PAH monolayer deposition

Each sample was submerged in a 10 mM PAH solution (prepared at pH 7.0) for 10 min, rinsing it in nanopure water for a further 10 min to remove the excess PAH film. Thereafter, it was dried under a stream of air. This yielded a positively-charged polymer layer on the surface of the sample.

Step 3 Large Au NS adsorption

The modified substrates were immersed in 3 mL of as-received suspensions of 60-nm-sized Au NSs with no an additional pH adjustment for 24 h at room temperature. They were then rinsed with nanopure water to remove weakly-bound Au NSs from the samples, followed by blow drying with compressed air. The resulting samples showed a pink color, indicating the adsorption of Au NSs on the surface of samples.

Step 4 and Step 5 UV and Ozone treatment

Samples were then transferred into a UV-ozone cleaner (Bioforce, Inc.) for 40 min to remove organic substances, particularly the PAH film as well as undesired substances from the surface [41-43]. The ozone cleaner generates UV light at 184.9 nm and 253.7 nm from a low-vapor Hg lamp. Both UV exposure and oxidation from the formation and decomposition of ozone (O_3) can convert organic compounds into volatile substances such as CO_2, N_2, and H_2O among others. Note that the time for removing contaminants may vary due to power fluctuation of the UV-ozone cleaner.

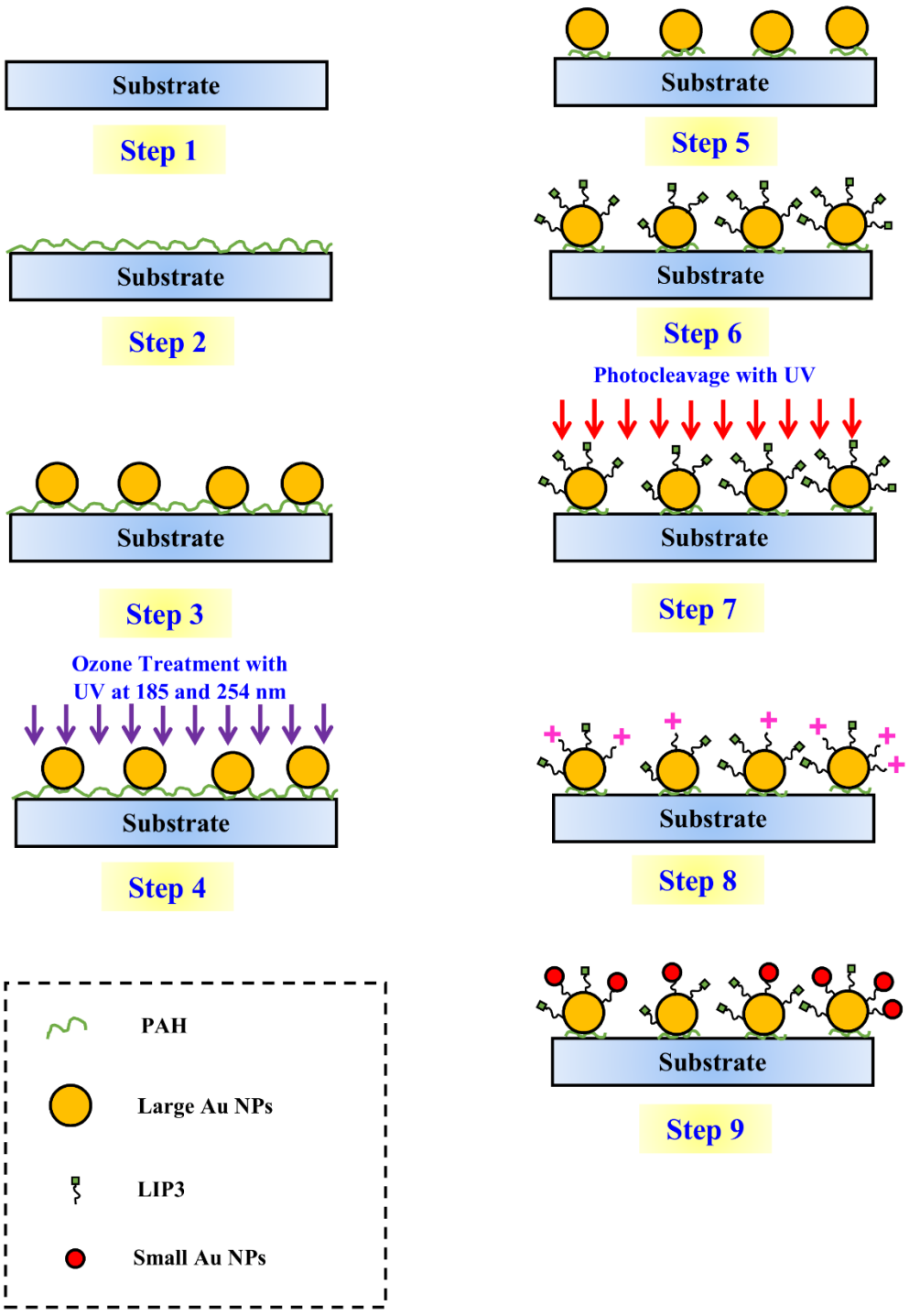

Figure 4.13: Illustration of the steps of nanoparticle assembly on a glass substrate.

After samples were exposed to UV-ozone, only large Au NSs with PAH underneath them resided on the surface. If the UV-ozone exposure time was less than the optimal time (40 min), some PAH residues still remained on the surface, which caused binding of small Au NSs directly to the surface in Step 8 and 9. However, if the exposure time was too long, UV and strong oxidation from O_3 removed all the PAH including from beneath the large Au NSs so that they were no longer attached to the substrate.

Step 6 LIP3 functionalization

The adsorbed Au NSs were coated by LIP3 by immersing the samples in a 1 mM LIP3 ethanoic solution at room temperature and in a sealed container under Ar for 24 h to ensure complete coverage of LIP3 on the exposed gold surface. After the incubation, the samples were in turn rinsed with ethanol and nanopure water. Thereafter, they were dried under a stream of Ar gas. This step was performed in a dark environment. Only red light was allowed during the steps involving LIP3 because it provides minimal UV irradiation which otherwise may cause unintended photocleavage of LIP3 before subsequent light exposure steps

Step 7 Exposure to green and polarized UV light

Green light exposures

After the samples from step 6 were dried with Ar gas, they were immediately exposed to green light at 550 nm for 40 min. The setup for green light exposure is shown in Figure 4.14.

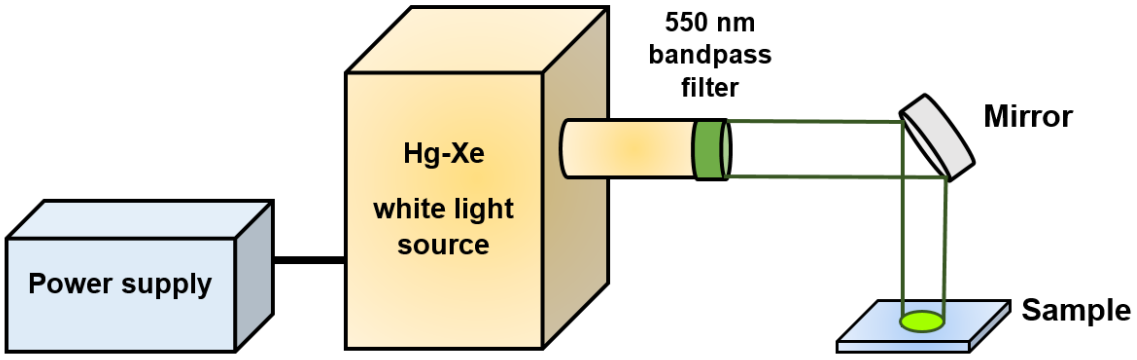

Figure 4.14: Schematic of a 550 nm green light exposure setup.

The Mercury-Xenon white light source emits a continuous spectrum with high intensity ranging from UV to infrared region. However, a 550 nm bandpass filter with a 10 nm bandwidth (550FS10-50, Andover Corporation) transmits green light which is then reflected by a mirror onto the samples. The power density at the sample is 2 mW/cm^2.

Green light exposures were found to inhibit Au NSs attachment and binding to cleaved LIP3 [37]. As a result, it removes non-specific binding of small Au NSs in step 8.

UV exposures

After green light exposure, the samples were immediately exposed to UV for various time and polarizations configurations. Figure 4.15 displays the setup for UV exposure with a 376 nm UV laser (Stradus® 375-60, Vortran Laser Technology, Inc.). The incident optical power was reduced by a neutral density filter (NE005, Thorlabs, Inc), and the beam diameter was enlarged by a beam expander (BE02-05-A, Thorlabs, Inc) before exposing on a sample. This resulted in an intensity on the sample of 2 mW/cm^2 as measured by a laser power meter (Thorlabs, Inc.) To vary the UV dose, the laser exposure time was controlled by a LabVIEW computer program. [*This program was written by Dr. Kirby Myers from Dr.Robinson's group, Physics department, Virginia Tech.*]

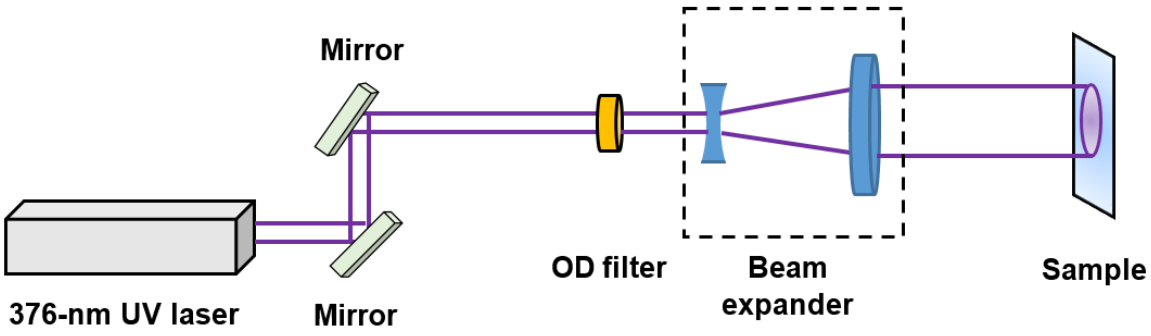

Figure 4.15: Schematic diagram of the UV exposure setup. The experiment was conducted in ambient air at room temperature.

The samples were separated into two sets: the first set contained one sample (sample Z) exposed to unpolarized UV irradiation, while the second set consisted of twelve samples (sample A-L) exposed to polarized UV irradiation at different doses.

Sample Z was used as a control to ensure that small Au NSs adhere to the larger Au NSs everywhere. The exposure of sample Z was carried out using unpolarized UV light at 365 nm provided by a UV Crosslinker (FB-UVXL-1000, Fisher Scientific) for 15 min. The corresponding dose (or energy density) was around 2700 mJ/cm^2, which was enough to fully photocleave surface bound LIP3 to uncage the primary amine (-NH_2) groups. A shadow mask was used to allow certain areas of the sample to avoid UV exposure. This created Au NSs adhesion bands which were visible to the naked eye after step 8.

The second set of samples were exposed to polarized UV light under varying conditions as shown in Table 4.1. Note that the polarization angle is measured counter clockwise with respect to the sample's horizontal.

Table 4.1: List of samples exposed to UV light with various doses and polarization angles.

Sample Name	Exposure Dose (mJ/cm^2)	Exposure Type	Polarization angle (degree)
A	0	N/A	N/A
B	0.5	Polarized	135
C	1.0	Polarized	135
D	2.5	Polarized	135
E	5.0	Polarized	135
F	15.0	Polarized	135
G	90.0	Polarized	135
H	200	Polarized	135
I	500	Polarized	135
J	1000	Polarized	135
K	2.5	Polarized	45

L	2.5	Polarized	90
Z	2700	Unpolarized	N/A

The experimental procedures can also be summarized in Figure 4.16

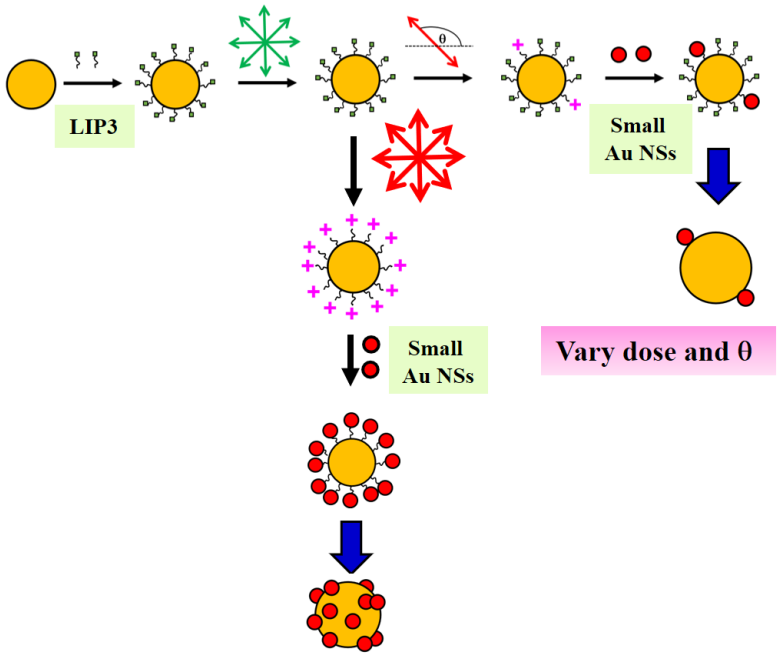

Figure 4.16: Schematic of the creation of aligned nanostructures.

Step 8 and Step 9 Attachment of small Au NSs onto large Au NSs

The UV-activated samples were incubated in a suspension of small 16-nm Au NSs containing 4 mM of NaCl salt for 60 min to ensure good binding between the small and large Au NSs. The salt was introduced into the gold colloids to increase the ionic strength and thereby reduce the Debye length, which enhances small Au NSs attachment [44-46]. Without the salt, the negative charges on the surface of a substrate repel the negatively charged Au NSs, preventing the binding between the small and the large Au NSs. In other words, the added salt screens or shields these negative charges, allowing the small Au NSs get closer to the larger Au NSs. The pH of the suspension was 6.0, low enough to protonate primary amines to give them a positively charge, but not so low so as to neutralize the negative charge of the citrate ions on the smaller

Au NSs. Note that the pKa of amines are lower in surface SAMs compared to in solution, which necessitates pH below neutral. The unreacted Au NSs were removed by rinsing samples thoroughly with nanopure water, after which samples were dried under a stream of N_2 gas. This resulted in assemblies of Au NSs adsorbed on the samples that were ready for optical and other characterizations, such as field emission scanning electron microscopy (FESEM) imaging.

4.5 Results and discussions

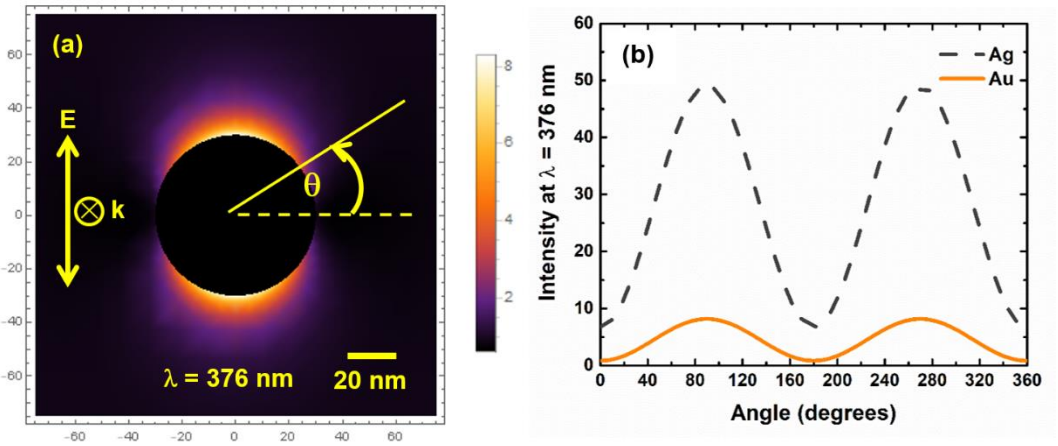

Material	Polar enhancement	Equatorial enhancement	Ratio
Ag	49.0	6.8	7.2
Au	8.2	0.9	9.1

Figure 4.17: (a) Optical intensity distribution map for a 60 nm diameter Au sphere exposed to linearly polarized light of wavelength λ = 376 nm, and (b) a plot of the intensity enhancement on the surface of pure Au (orange) and pure silver (grey) NSs as a function of the polar angle.

To understand how small Au NSs bind to the large Au NSs in the direction of UV polarization axis, we need to find the factors that cause LIP3 to undergo the photocleavable reaction. This can be attributed to the plasmonic enhancement in the large Au NSs. When linearly polarized light at the plasmon resonance wavelength is incident on the large Au NSs, the optical intensity near the surface of the sphere is significantly enhanced so that the incident light is sufficient for the photocleavage of LIP3. Figure 4.17 (a) illustrates a distribution of the optical intensity on the surface of a Au NS with a diameter of 60 nm that

was exposed to vertically polarized (along the y-axis) light incident into the plane, where the excitation wavelength is 376 nm. This simulation was performed using a computer program implementing Mie Theory written by Dr. Hans Robinson in Mathematica. It is expected that the intensity is greatly enhanced near the poles of the particle, as defined by the orientation of the incident light polarization. Figure 4.17 (b) plots the intensity enhancement along the surface of pure Au (orange) and Ag (grey) spheres as a function of the polar angle. This angle is measured from the equator in the clockwise direction around the sphere. At the poles ($\theta = 90°, 270°$) of the Au sphere, a 8-fold intensity enhancement is observed relative to the incident light intensity. On the contrary, at the equators ($\theta = 0°, 180°$) of the same particle, the intensity is reduced by about 90%. For a Ag sphere, the polar and equatorial intensities are respectively 49 and 7 times greater than that of incident light. The plasmonic enhancement is much greater in Ag spheres than in Au spheres because the Au NSs have no plasmonic resonance at 376 nm, while the Ag NSs do. The resonance wavelength of a 30 nm dimeter Au NS is around 526 nm, which is far beyond the excitation wavelength. However, the ratio of polar to equatorial light intensity is still greater in Au than Ag. From this theoretical calculation, it is clear that the absence of plasmonic enhancement in Au may not be an impediment to achieving patchiness. Finally, if the UV light dose is sufficiently large (or on the order of J/cm^2), this should result in the full photocleavage of LIP3s everywhere on the sphere, removing the selectivity in the alignment of the nanosphere binding.

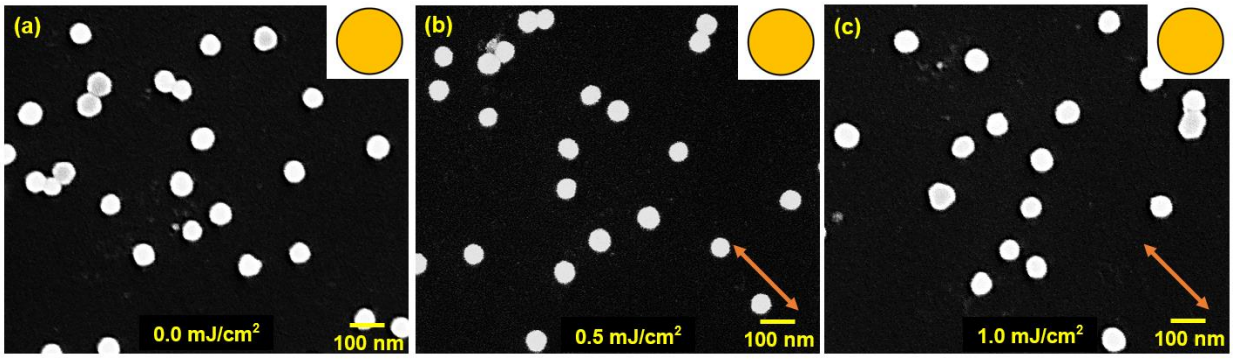

Figure 4.18: FESEM micrographs of (a) sample A, (b) sample B, and (c) sample C. Sample A was exposed to green light only, while samples B and C were exposed to linearly polarized UV light with a dose of 0.5 and 1.0 mJ/cm^2, respectively.

To qualitatively determine whether pairs of Au NSs are present on the substrate, imaging with FESEM was carried out. Figure 4.18 shows FESEM images of samples A, B, and C that were exposed to linearly polarized UV light with doses of 0.0, 0.5, and 1.0 mJ/cm^2. Each image except where no UV light was applied includes an orange arrow that indicates the orientation of the UV laser polarization. Since the UV dose is too small, the intensity enhancement around the large Au NS is not enough to photocleave a sufficient amount of LIP3 that NS binding occurs. Therefore, we do not observe the attachment of small Au NSs to the large Au NSs for these very small doses.

Figure 4.19 (a), (c), (e), and (g) show FESEM images of samples that were exposed to linearly polarized UV light with higher doses, but so high so as to fully cleave all LIP3. In this case, we expect preferential binding along the direction of the UV light polarization. The FESEM images verified this and a statistical survey of NP binding orientation shows strong preferences for binding near the expected 135 degrees for all doses between 2.5 mJ/cm^2 to 90 mJ/cm^2. In addition to the aligned binding, some degree of binding that was not along the UV light polarization axis was also observed. This results from the non-specific binding that occurs before green light exposure. As the Au NS binding is a random process, all particle configurations have a non-negligible probability to exist. However, binding along the UV light polarization axis has a greater probability to occur than the other binding orientations.

Figure 4.20 (a)-(c) depict the FESEM images of samples H, I, and J that were exposed to polarized UV irradiation at a dose of 200, 500, and 1000 mJ/cm^2, respectively. Here, small Au NSs adhere to not only the portions of large Au NSs that were exposed to polarized UV light, but also the portions of the unexposed ones. The result of this polarized exposure shows a similar pattern of Au NSs bindings as the sample exposed to unpolarized UV light (or from a UV crosslinker) as shown in Figure 4.20 (b) or Figure 4.11 (d). In other words, if the UV dose is sufficiently high, all areas of the large Au NSs are fully photocleaved no matter what direction of the polarization of UV light is, and the small Au NSs will bind everywhere with equal probability.

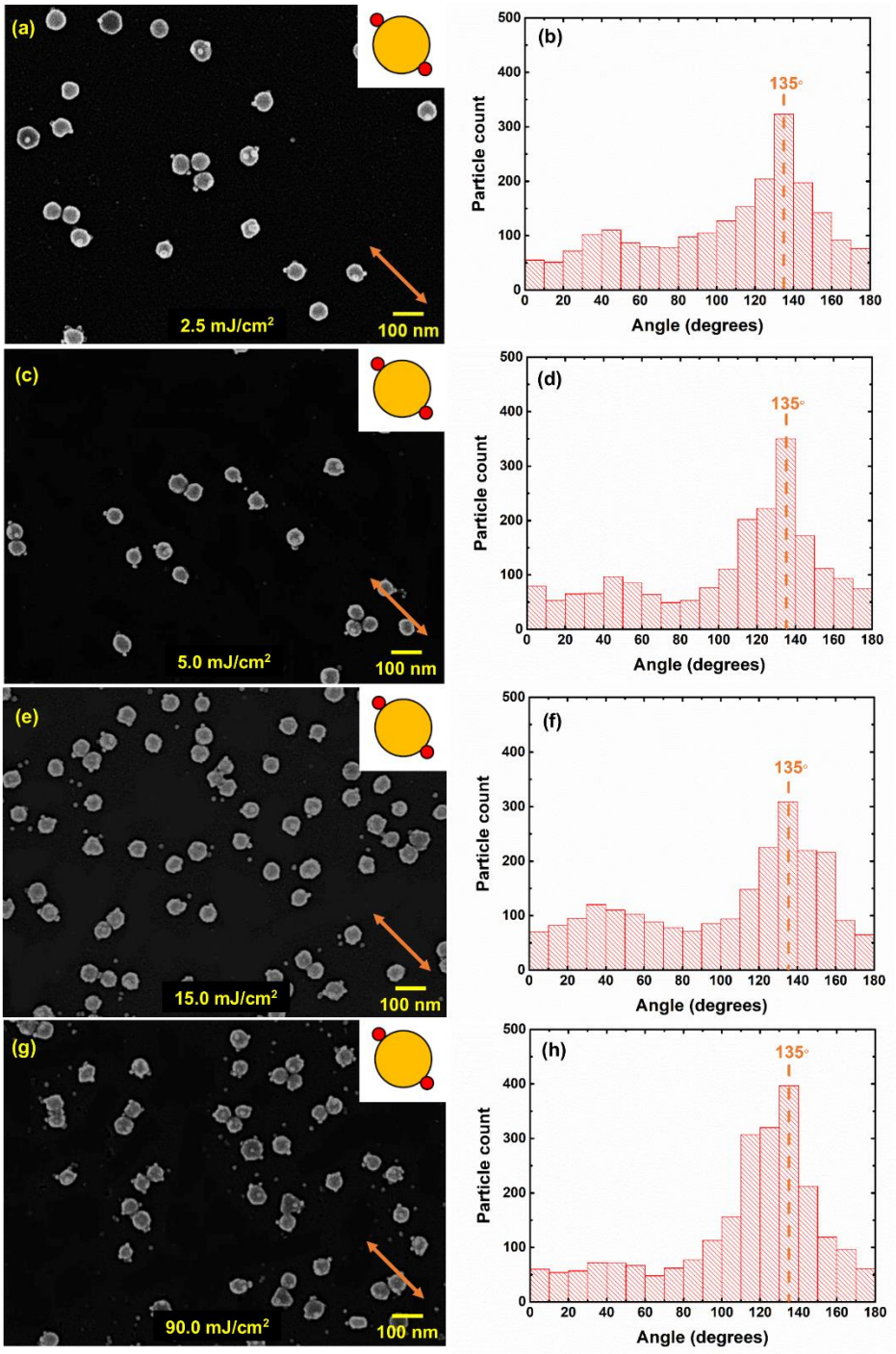

Figure 4.19: (a), (c), (e), and (g) are FESEM micrographs, while (b), (d), (f), and (h) are the corresponding particle relative orientation distributions (right) of samples. Samples D, E, F, and G were exposed to polarized UV light with doses of 2.5, 5.0, 15.0, and 90.0 mJ/cm^2, respectively. The number of particles used in this analysis were N = 2151, 2037, 2270, and 2349, respectively. Orange arrows indicate UV light polarization axes that were used to expose the samples.

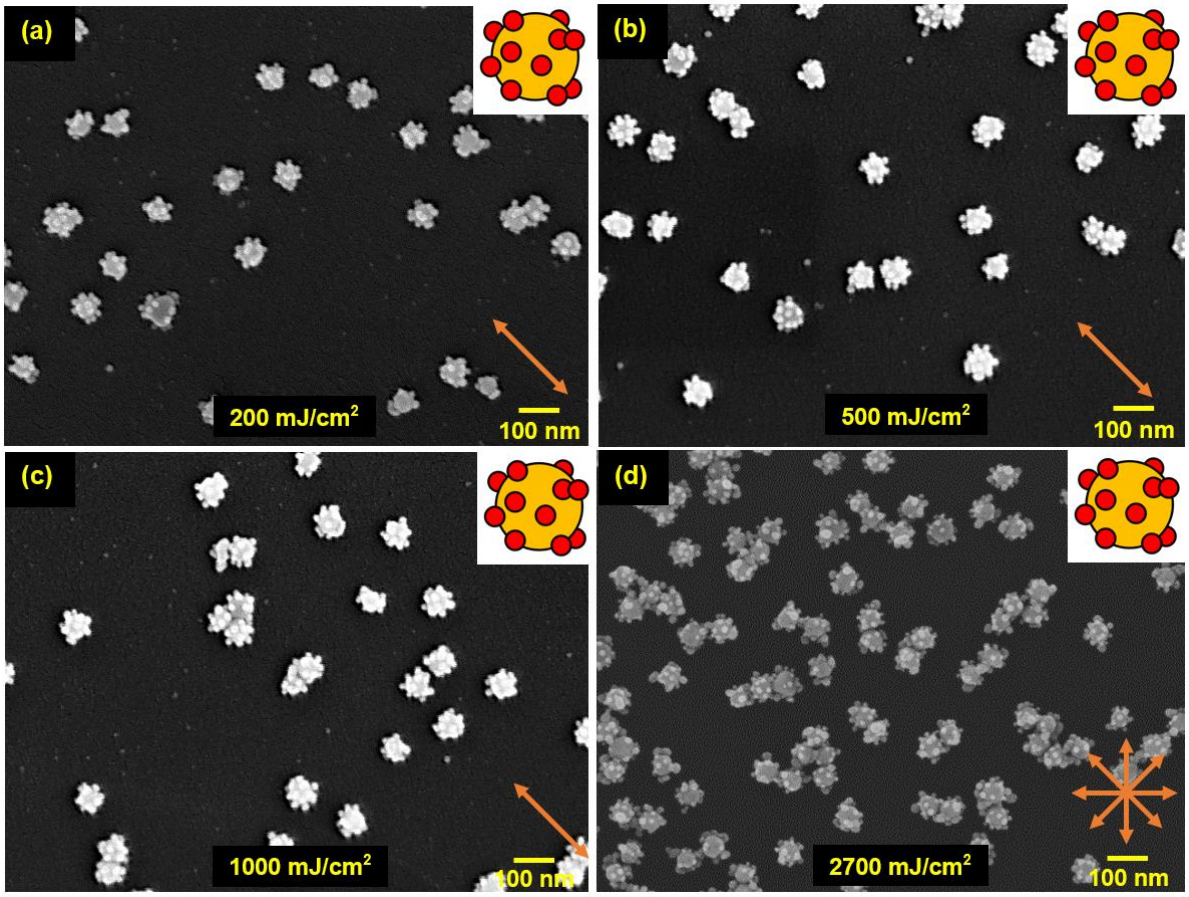

Figure 4.20: FESEM micrographs of (a) sample H, (b) sample I, (c) sample J, and (d) sample Z. Samples H, I, and J were exposed to linearly polarized UV light with a dose of 200, 500, and 1000 mJ/cm^2, respectively. Sample Z was exposed to unpolarized UV light with a dose of 2700 mJ/cm^2.

To characterize the relative orientation of the aligned pairs, the location of small Au NSs adhering to the surface of large Au NSs is quantified in terms of the angle from the horizontal to a line connecting the centers of the small and large Au NSs in a dimer or trimer, measured in the counterclockwise direction. Orientation angles between 180° and 360° are shifted to the 0° to 180° range, which is reasonable due to the symmetry of the assembly. This angle measurement was performed using a computer program written by Dr. Hans Robinson in Mathematica that analyzed FESEM images for all samples. In this analysis, at least 2000 pairs from each sample were measured.

Figure 4.19 (b), (d), (f) and (h) display the Au NSs dimer relative orientation distributions determined from FESEM imaging. All histograms show that about 20 percent of the larger nanostructures consists of dimers that are aligned in the range of 130 to 140 degrees, while the UV light polarization axis used in this experiment was 135 degrees. These results are consistent with those previously discussed from the FESEM images. In other words, other dimers alignments and non-dimer orientations are still observed. These other orientations result from two factors. First, the variation of the intensity enhancement around the large Au NS is shown in Figure 4.17. The enhancement is large enough to photocleave LIP3 over a wide range of angles, allowing the small Au NSs to bind to the large Au NSs over the same range of angles. The second factor is the non-specific binding of small Au NSs that occurs regardless of polarized UV light exposure. This issue may possibly be reduced by longer time green light exposure. For samples H, I, J, and Z, there is no discernible alignment as small Au NSs adhere to larger Au NSs almost all orientations. Therefore, the particle's orientation distributions for these samples are not shown because the probability of particle bindings is equal in every orientation.

To verify that the selective orientation of the Au NSs dimers is in fact due to the UV polarization, samples K and L were exposed to UV light with different polarization angles in comparison with sample D, but with the same dose of 2.5 mJ/cm^2. Figure 4.21 shows representative FESEM images and the corresponding particle orientation distributions of samples D, K, and L. At least 20 percent of the larger nanostructures were aligned along the direction of the UV polarization, verifying that the small Au NSs preferentially bind to the large Au NSs along the direction of UV polarization.

Lastly, there are two interesting things to note. First, the width of the alignment is much narrower than expected from Figure 4.17, possibly due to a funneling effect of the electric field created by the patches. It is possible that we need the larger number of particles used in the analysis to observe the expected computational result. Second, the alignment is seen at very low doses, so low that we would expect only a few percent of LIP3 molecules to be cleaved the center of the dipolar patches.

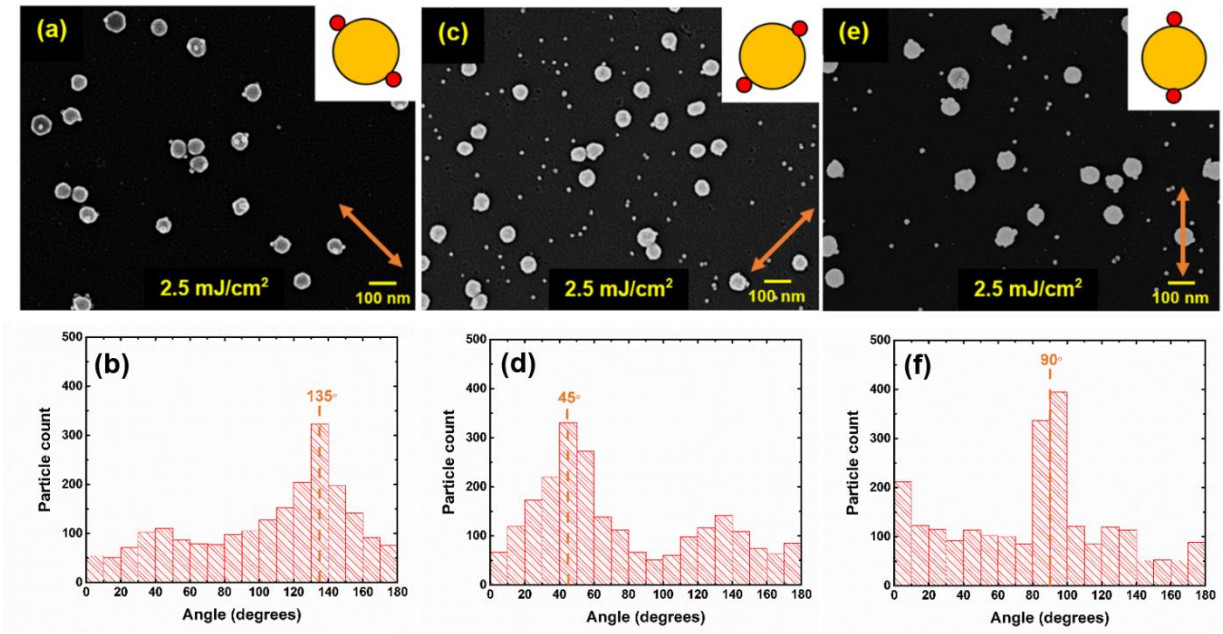

Figure 4.21: (a), (c), (e) are FESEM micrographs, while (b), (d), and (f) are the corresponding particle orientation distributions of samples D, K, and L. These samples were all exposed to polarized UV light with a dose of 2.5 mJ/cm^2 but with different polarization axes. The number of particles used in this analysis were N = 2151, 2312, and 2359, respectively. Orange arrows indicate UV light polarization axes that were used to expose the samples.

4.6 Conclusions

A novel approach to nanoparticle assembly was proposed and demonstrated, where spherical Au NPs were used as the building blocks, resulting in well-defined aligned Au NS dimers. The photocleavable molecule LIP3 was functionalized on the surface of large Au NSs and used to bind smaller Au NSs to the larger Au spheres. We showed that the dipolar patch alignment can be determined by the polarization and dose of UV light, which caused the polar areas of the large Au NSs to become positively charged. This allowed negatively charged small Au NSs to preferentially attach to the poles, making Au NS dimers aligned with the orientation of the UV light polarization. This was verified by analysis from FESEM images over large numbers of particle assemblies which showed that the small Au NSs bound more favorably to the large Au NSs in the direction of UV polarization. This method in other words provides a new tool for anisotropic nanoparticle assembly. Our method of assembly is flexible and conceptually simple and has potential

applications in multiple contexts, such as biomedicine and nanorobotics. In addition, our results demonstrated that green light exposure can prevent cleaved LIP3s from adsorbing negatively charged Au NSs, thereby eliminating non-specific bindings of small Au NSs to large Au NSs. Another interesting result is the effect of lipoic acid on LIP3 SAM properties. When samples consisting of LIP3 and lipoic acid were exposed to only green light, a significant reduction in non-specific pre-UV Au NSs binding occurs when the molar ratio of lipoic acid to LIP3 is at least 0.5%.

4.7 Future work

The photocleavable molecule LIP3 used in this experiment undergoes a photouncaging reaction when it absorbs a single UV photon. However, it is also possible to employ two-photon photocleavage of LIP3, which can enhance selectivity in the bounding to photocleaved regions. This can be accomplished by using a femtosecond-pulsed laser instead of a continuous wave light source. Furthermore, the wavelength of this light source should be in the infrared (~700-800 nm) region so that the resulting two-photon wavelength is suitable for the photouncaging reaction of LIP3.

It is also possible to fabricate other aligned nanostructures from non-spherical NPs, including Au nanorods, Au nanoprisms, and Au nanostars because this kind of NPs has two interesting characteristics. First, on resonance, these anisotropic NPs exhibit highly intense electromagnetic field near the tips, sharp edges, or high curvature regions of the structures. Second, the LSPR wavelength of these non-spherical NPs can be flexibly tuned by changing their geometry. We can thus control the shape of this kind of NPs to achieve a LSPR that is resonant with the wavelength of the laser. This could make it possible to flexibly create other orientational nanostructures, including nanorod-nanosphere dumbells and nanocube-nanosphere trimers as shown in Figure 4.1 (c) and (d) [14, 16, 18, 26, 27].

4.8 References

[1] G. Frens, Controlled Nucleation for the Regulation of the Particle Size in Monodisperse Gold Suspensions, Nature, 241 (1973) 20-22.

[2] S.R. Ghanta, K. Muralidharan, Chemical synthesis of aluminum nanoparticles, Journal of Nanoparticle Research, 15 (2013) 1715.

[3] S. Iravani, H. Korbekandi, S.V. Mirmohammadi, B. Zolfaghari, Synthesis of silver nanoparticles: chemical, physical and biological methods, Research in Pharmaceutical Sciences, 9 (2014) 385-406.

[4] X. Huang, M.A. El-Sayed, Gold nanoparticles: Optical properties and implementations in cancer diagnosis and photothermal therapy, Journal of Advanced Research, 1 (2010) 13-28.

[5] T.-H. Meen, W.-C. Ciou, S.-M. Chao, Y.-S. Liu, T.-H. Fang, C.T. Ho, C.-J. Huang, Structural and Magnetic Properties of Different Shape Gold Nanoparticles, ECS Transactions, 19 (2009) 17-23.

[6] J.M. Wessels, H.-G. Nothofer, W.E. Ford, F. von Wrochem, F. Scholz, T. Vossmeyer, A. Schroedter, H. Weller, A. Yasuda, Optical and Electrical Properties of Three-Dimensional Interlinked Gold Nanoparticle Assemblies, Journal of the American Chemical Society, 126 (2004) 3349-3356.

[7] C. Li, D. Li, G. Wan, J. Xu, W. Hou, Facile synthesis of concentrated gold nanoparticles with low size-distribution in water: temperature and pH controls, Nanoscale Research Letters, 6 (2011) 440.

[8] J. Turkevich, P.C. Stevenson, J. Hillier, A study of the nucleation and growth processes in the synthesis of colloidal gold, Discussions of the Faraday Society, 11 (1951) 55-75.

[9] H. Wang, X. Qiao, J. Chen, S. Ding, Preparation of silver nanoparticles by chemical reduction method, Colloids and Surfaces A: Physicochemical and Engineering Aspects, 256 (2005) 111-115.

[10] C. Ziegler, A. Eychmüller, Seeded Growth Synthesis of Uniform Gold Nanoparticles with Diameters of 15−300 nm, The Journal of Physical Chemistry C, 115 (2011) 4502-4506.

[11] H.S. Choi, Nanoparticle assembly: Building blocks for tumour delivery, Nat Nano, 9 (2014) 93-94.

[12] L.Y.T. Chou, K. Zagorovsky, W.C.W. Chan, DNA assembly of nanoparticle superstructures for controlled biological delivery and elimination, Nat Nano, 9 (2014) 148-155.

[13] E. Katz, I. Willner, Integrated Nanoparticle–Biomolecule Hybrid Systems: Synthesis, Properties, and Applications, Angewandte Chemie International Edition, 43 (2004) 6042-6108.

[14] X. Kou, Z. Sun, Z. Yang, H. Chen, J. Wang, Curvature-Directed Assembly of Gold Nanocubes, Nanobranches, and Nanospheres, Langmuir, 25 (2009) 1692-1698.

[15] D. Lee, S. Yoon, Gold Nanocube–Nanosphere Dimers: Preparation, Plasmon Coupling, and Surface-Enhanced Raman Scattering, The Journal of Physical Chemistry C, 119 (2015) 7873-7882.

[16] P. Pramod, S.T.S. Joseph, K.G. Thomas, Preferential End Functionalization of Au Nanorods through Electrostatic Interactions, Journal of the American Chemical Society, 129 (2007) 6712-6713.

[17] D.A. Walker, C.E. Wilmer, B. Kowalczyk, K.J.M. Bishop, B.A. Grzybowski, Precision Assembly of Oppositely and Like-Charged Nanoobjects Mediated by Charge-Induced Dipole Interactions, Nano Letters, 10 (2010) 2275-2280.

[18] H. Zhang, E.W. Edwards, D. Wang, H. Mohwald, Directing the self-assembly of nanocrystals beyond colloidal crystallization, Physical Chemistry Chemical Physics, 8 (2006) 3288-3299.

[19] S.J. Zhen, C.Z. Huang, J. Wang, Y.F. Li, End-to-End Assembly of Gold Nanorods on the Basis of Aptamer−Protein Recognition, The Journal of Physical Chemistry C, 113 (2009) 21543-21547.

[20] X. Wu, L. Xu, L. Liu, W. Ma, H. Yin, H. Kuang, L. Wang, C. Xu, N.A. Kotov, Unexpected Chirality of Nanoparticle Dimers and Ultrasensitive Chiroplasmonic Bioanalysis, Journal of the American Chemical Society, 135 (2013) 18629-18636.

[21] L. Guo, Y. Xu, A.R. Ferhan, G. Chen, D.-H. Kim, Oriented Gold Nanoparticle Aggregation for Colorimetric Sensors with Surprisingly High Analytical Figures of Merit, Journal of the American Chemical Society, 135 (2013) 12338-12345.

[22] T. Chen, Y. Hong, B.M. Reinhard, Probing DNA Stiffness through Optical Fluctuation Analysis of Plasmon Rulers, Nano Letters, 15 (2015) 5349-5357.

[23] L.H. Tan, H. Xing, H. Chen, Y. Lu, Facile and Efficient Preparation of Anisotropic DNA-Functionalized Gold Nanoparticles and Their Regioselective Assembly, Journal of the American Chemical Society, 135 (2013) 17675-17678.

[24] M.M. Maye, D. Nykypanchuk, M. Cuisinier, D. van der Lelie, O. Gang, Stepwise surface encoding for high-throughput assembly of nanoclusters, Nature Materials, 8 (2009) 388.

[25] Y. Zhao, L. Xu, L.M. Liz-Marzán, H. Kuang, W. Ma, A. Asenjo-García, F.J. García de Abajo, N.A. Kotov, L. Wang, C. Xu, Alternating Plasmonic Nanoparticle Heterochains Made by Polymerase Chain Reaction and Their Optical Properties, The Journal of Physical Chemistry Letters, 4 (2013) 641-647.

[26] A.S. D. S. Indrasekara, R. Thomas, L. Fabris, Plasmonic properties of regiospecific core-satellite assemblies of gold nanostars and nanospheres, Physical Chemistry Chemical Physics, 17 (2015) 21133-21142.

[27] E.M. See, C.L. Peck, X. Guo, W. Santos, H.D. Robinson, Plasmon-Induced Photoreaction of o-Nitrobenzyl-Based Ligands under 550 nm Light, The Journal of Physical Chemistry C, 121 (2017) 13114-13124.

[28] C. Daengngam, S.B. Thorpe, X. Guo, S.V. Stoianov, W.L. Santos, J.R. Morris, H.D. Robinson, High Photoreactivity of o-Nitrobenzyl Ligands on Gold, The Journal of Physical Chemistry C, 117 (2013) 14165-14175.

[29] J.A. Rodriguez, J. Dvorak, T. Jirsak, G. Liu, J. Hrbek, Y. Aray, C. González, Coverage Effects and the Nature of the Metal−Sulfur Bond in S/Au(111): High-Resolution Photoemission and Density-Functional Studies, Journal of the American Chemical Society, 125 (2003) 276-285.

[30] S. Roux, B. Garcia, J.-L. Bridot, M. Salomé, C. Marquette, L. Lemelle, P. Gillet, L. Blum, P. Perriat, O. Tillement, Synthesis, Characterization of Dihydrolipoic Acid Capped Gold Nanoparticles, and Functionalization by the Electroluminescent Luminol, Langmuir, 21 (2005) 2526-2536.

[31] A.A. Volkert, V. Subramaniam, M.R. Ivanov, A.M. Goodman, A.J. Haes, Salt-Mediated Self Assembly of Thioctic Acid on Gold Nanoparticles, ACS nano, 5 (2011) 4570-4580.

[32] I. Aujard, C. Benbrahim, M. Gouget, O. Ruel, J.-B. Baudin, P. Neveu, L. Jullien, o-Nitrobenzyl Photolabile Protecting Groups with Red-Shifted Absorption: Syntheses and Uncaging Cross-Sections for One- and Two-Photon Excitation, Chemistry – A European Journal, 12 (2006) 6865-6879.

[33] M.S. Kim, S.L. Diamond, Photocleavage of o-nitrobenzyl ether derivatives for rapid biomedical release applications, Bioorganic & Medicinal Chemistry Letters, 16 (2006) 4007-4010.

[34] P. Klán, T. Šolomek, C.G. Bochet, A. Blanc, R. Givens, M. Rubina, V. Popik, A. Kostikov, J. Wirz, Photoremovable Protecting Groups in Chemistry and Biology: Reaction Mechanisms and Efficacy, Chemical Reviews, 113 (2013) 119-191.

[35] M.-T. Lee, C.-C. Hsueh, M.S. Freund, G.S. Ferguson, Air Oxidation of Self-Assembled Monolayers on Polycrystalline Gold: The Role of the Gold Substrate, Langmuir, 14 (1998) 6419-6423.

[36] Y. Fang, Y. Li, H. Xu, M. Sun, Ascertaining p,p′-Dimercaptoazobenzene Produced from p-Aminothiophenol by Selective Catalytic Coupling Reaction on Silver Nanoparticles, Langmuir, 26 (2010) 7737-7746.

[37] E.M. See, C.L. Peck, X. Guo, W. Santos, H.D. Robinson, Plasmon-Induced Photoreaction of o-Nitrobenzyl-Based Ligands under 550 nm Light, The Journal of Physical Chemistry C, DOI 10.1021/acs.jpcc.7b00707(2017).

[38] S.A. Swanson, R. McClain, K.S. Lovejoy, N.B. Alamdari, J.S. Hamilton, J.C. Scott, Self-Assembled Diisocyanide Monolayer Films on Gold and Palladium, Langmuir, 21 (2005) 5034-5039.

[39] T. Daisuke, Y. Tatsuya, G. Gaurav, O. Haruki, H. Kazuhiko, K. Kotaro, Second harmonic generation from hemicyanine self-assembled monolayer on near-hemispherical gold nanoparticles, Journal of Physics D: Applied Physics, 44 (2011) 425301.

[40] T. Yamaguchi, H. Okawa, K. Hashimoto, K. Kajikawa, Formation Process of Self-Assembled Monolayer on Gold Nanosphere Probed by Second Harmonic Generation, Langmuir, 26 (2010) 14543-14547.

[41] E.W. Elliott, R.D. Glover, J.E. Hutchison, Removal of Thiol Ligands from Surface-Confined Nanoparticles without Particle Growth or Desorption, ACS Nano, 9 (2015) 3050-3059.

[42] P. Shufeng, K. Yousuke, K. Takeshi, K. Takeshi, Decomposition of Monolayer Coverage on Gold Nanoparticles by UV/ozone Treatment, Chemistry Letters, 34 (2005) 544-545.

[43] J.R. Vig, UV/ozone cleaning of surfaces, Journal of Vacuum Science & Technology A: Vacuum, Surfaces, and Films, 3 (1985) 1027-1034.

[44] C. Pfeiffer, C. Rehbock, D. Hühn, C. Carrillo-Carrion, D.J. de Aberasturi, V. Merk, S. Barcikowski, W.J. Parak, Interaction of colloidal nanoparticles with their local environment: the (ionic) nanoenvironment around nanoparticles is different from bulk and determines the physico-chemical properties of the nanoparticles, Journal of the Royal Society Interface, 11 (2014) 20130931.

[45] R. Tadmor, E. Hernández-Zapata, N. Chen, P. Pincus, J.N. Israelachvili, Debye Length and Double-Layer Forces in Polyelectrolyte Solutions, Macromolecules, 35 (2002) 2380-2388.

[46] F. Zhang, Z. Ali, F. Amin, A. Feltz, M. Oheim, W.J. Parak, Ion and pH Sensing with Colloidal Nanoparticles: Influence of Surface Charge on Sensing and Colloidal Properties, ChemPhysChem, 11 (2010) 730-735.

[47] P.S. Archana, N. Pachauri, Z. Shan, S. Pan, A. Gupta, Plasmonic Enhancement of Photoactivity by Gold Nanoparticles Embedded in Hematite Films, The Journal of Physical Chemistry C, 119 (2015) 15506-15516.

[48] A.S. Madden, M.F. Hochella, A test of geochemical reactivity as a function of mineral size: Manganese oxidation promoted by hematite nanoparticles, Geochimica et Cosmochimica Acta, 69 (2005) 389-398.

[49] L. Wang, Y. Zhu, L. Xu, W. Chen, H. Kuang, L. Liu, A. Agarwal, C. Xu, A. Kotov Nicholas Side-by-Side and End-to-End Gold Nanorod Assemblies for Environmental Toxin Sensing, Angewandte Chemie International Edition, 49 (2010) 5472-5475.

[50] J. Lee, P. Hernandez, J. Lee, A.O. Govorov, N.A. Kotov, Exciton–plasmon interactions in molecular spring assemblies of nanowires and wavelength-based protein detection, Nature Materials, 6 (2007) 291.

[51] A.J. Mastroianni, S.A. Claridge, A.P. Alivisatos, Pyramidal and Chiral Groupings of Gold Nanocrystals Assembled Using DNA Scaffolds, Journal of the American Chemical Society, 131 (2009) 8455-8459.

Appendix A : A theoretical SPR reflectivity curve by a transfer matrix formulation

The occurrence of SPR corresponds to a minimum in the reflectance of the metal film as it appears in graphs of the reflectivity R vs the incident angle θ_0 for a certain wavelength λ. For the case of Kretschmann configuration, a powerful way for deriving reflected and transmitted intensities is known as the *characteristic transfer matrix (CTM)* method. This approach represents boundary conditions at the film interfaces in the form of matrices, which leads to the calculation of reflectance and transmittance of light in a multilayer thin film system.

This section summarizes this theory and presents results where it is applied to the Kretschmann configuration. For a complete derivation as well as a thorough discussion of this topic, however, other references should be consulted [1].

A.1 A multilayer thin film system

Consider a stack of N thin films as shown in Figure A.1 (b) where the i-th layer has the corresponding thickness d_i and complex refractive index $\tilde{n}_i = n_i + ik_i$. In addition, the first layer is exposed to the half-space incident medium with $\tilde{n}_0$, whilst the N-th layer is contacted with the half-space substrate medium with $\tilde{n}_{N+1}$.

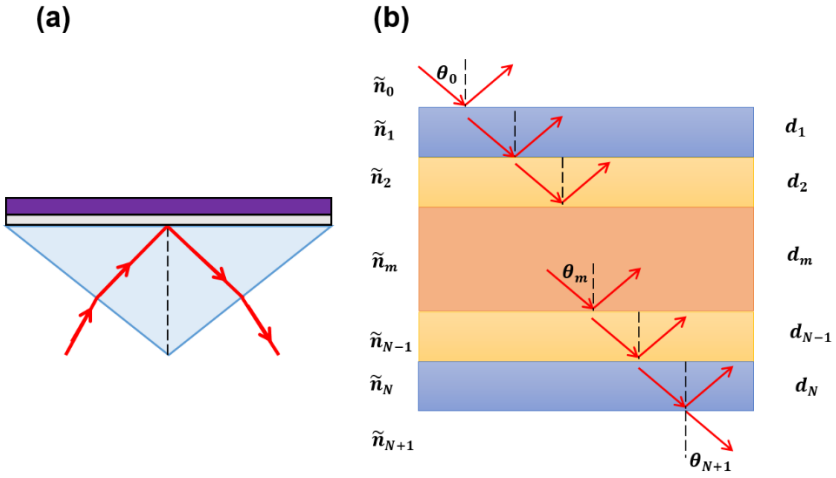

Figure A.1: (a) The Kretschmann configuration setup used in the experiment. (b) The model for CTM method which consists of a stack of layers with (complex) refractive indices $\tilde{n}_i$ and thickness d_i for $i = 0, 1, 2, \dots, N, N+1$.

If light in the form of a plane wave is incident on the stack from the $\tilde{n}_0$ medium with an incident angle θ_0, the complex amplitudes of the electric fields in the incident $\boldsymbol{E}_0$ and substrate media $\boldsymbol{E}_{N+1}$ are related by

$$\begin{pmatrix} E_0^F \\ E_0^B \end{pmatrix} = \boldsymbol{T_{0,N+1}} \begin{pmatrix} E_{N+1}^F \\ E_{N+1}^B \end{pmatrix} = \begin{pmatrix} T_{0,N+1}^{11} & T_{0,N+1}^{12} \\ T_{0,N+1}^{21} & T_{0,N+1}^{22} \end{pmatrix} \begin{pmatrix} E_{N+1}^F \\ E_{N+1}^B \end{pmatrix}, \tag{A.1.1}$$

where a complete transfer matrix $\boldsymbol{T_{0,N+1}}$ is given by

$$\boldsymbol{T_{0,N+1}} = \boldsymbol{T_{01}\Phi_1 T_{12}\Phi_2 T_{23}} \dots \boldsymbol{\Phi_N T_{N,N+1}}. \tag{A.1.2}$$

In other words, it is obtained by a multiplication of two types of matrices, the interface and bulk transfer matrices T_{ij} and Φ_i.

1.A transfer matrix through an interface between layers *i* and *j* : $\boldsymbol{T_{ij}}$

$$\boldsymbol{T_{ij}} = \frac{1}{t_{ij}} \begin{pmatrix} 1 & r_{ij} \\ r_{ij} & 1 \end{pmatrix}, \tag{A.1.3}$$

where Fresnel coefficients r_{ij} and t_{ij} for s- and p- polarizations are shown in Table A.1.

Table A.1: Fresnel coefficients r_{ij} and t_{ij} for light propagating through an interface where θ_i and θ_j are incident angles in medium i and medium j, respectively.

p- (or TM-) polarization	s- (or TE-) polarization
$r_{ij} = \dfrac{\tilde{n}_j \cos\theta_i - \tilde{n}_i \cos\theta_j}{\tilde{n}_j \cos\theta_i + \tilde{n}_i \cos\theta_j}$	$r_{ij} = \dfrac{\tilde{n}_i \cos\theta_i - \tilde{n}_j \cos\theta_j}{\tilde{n}_i \cos\theta_i + \tilde{n}_j \cos\theta_j}$
$t_{ij} = \dfrac{2\tilde{n}_i \cos\theta_i}{\tilde{n}_j \cos\theta_i + \tilde{n}_i \cos\theta_j}$	$t_{ij} = \dfrac{2\tilde{n}_i \cos\theta_i}{\tilde{n}_i \cos\theta_i + \tilde{n}_j \cos\theta_j}$

2.A transfer matrix through an i-th layer: $\boldsymbol{\Phi_i}$

$$\boldsymbol{\Phi_i} = \begin{pmatrix} e^{-i\phi_i} & 0 \\ 0 & e^{i\phi_i} \end{pmatrix}. \tag{A.1.4}$$

where ϕ_i represents the phase change of a plane wave as it propagates through medium i :

$$\phi_i = \frac{2\pi}{\lambda_0} n_i d_i \cos\theta_i, \tag{A.1.5}$$

where λ_0 is the wavelength of light in vacuum.

In sum, to deal with wave propagation problems in a multilayer stack, all matrices $\boldsymbol{T_{ij}}$ and $\boldsymbol{\Phi_i}$ must be first determined. Multiplication of all transfer matrices then give rise to the complete transfer matrix $\boldsymbol{T_{0,N+1}}$.

A.2 A special case: The Kretschmann configuration

For the case of the Krestschmann configuration (Figure A.1 (a)), a multilayer thin film system is involved where

(1) The medium may normally be air or buffer solution;
(2) Light typically impinges on the incident medium, which is the prism (e.g. a glass prism made of materials such a BK-7 or N-SF11 prism);
(3) $E_{N+1}^{B} = 0$, since no incident light is propagating toward the prism's hypotenuse.

Consequently, (A.1.1) becomes

$$\begin{pmatrix} E_0^F \\ E_0^B \end{pmatrix} = \boldsymbol{T_{0,N+1}} \begin{pmatrix} E_{N+1}^F \\ 0 \end{pmatrix} = \begin{pmatrix} T_{0,N+1}^{11} & T_{0,N+1}^{12} \\ T_{0,N+1}^{21} & T_{0,N+1}^{22} \end{pmatrix} \begin{pmatrix} E_{N+1}^F \\ 0 \end{pmatrix} = \begin{pmatrix} T_{0,N+1}^{11} E_{N+1}^F \\ T_{0,N+1}^{21} E_{N+1}^F \end{pmatrix}. \quad \text{(A.2.6)}$$

This equation enables us to calculate the reflection r and transmission t coefficients:

$$r = \frac{E_0^B}{E_0^F} = \frac{T_{0,N+1}^{21}}{T_{0,N+1}^{11}} \quad \text{(A.2.7)}$$

$$t = \frac{E_{N+1}^F}{E_0^F} = \frac{1}{T_{0,N+1}^{11}}$$

Finally, the total reflectance R and transmittance T of the multilayer thin film system are:

$$R = \frac{Re(\tilde{n}_0)\cos\theta_0 \, |E_0^B|^2}{Re(\tilde{n}_0)\cos\theta_0 \, |E_0^F|^2} = |r|^2 \quad \text{(A.2.8)}$$

$$T = \frac{Re(\tilde{n}_{N+1})\cos\theta_{N+1} \, |E_{N+1}^F|^2}{Re(\tilde{n}_0)\cos\theta_0 \, |E_0^F|^2} = \frac{Re(\tilde{n}_{N+1})\cos\theta_{N+1}}{Re(\tilde{n}_0)\cos\theta_0} |t|^2$$

Moreover, the phase of reflectance Φ is simply

$$\Phi = \arg r \quad \text{(A.2.9)}$$

A.3 SPR reflectivity curves in Au and $AuAl_2$ thin films

The reflected intensity R as a function of incident angle θ_0 for SPRs due to Kretschmann configuration can be calculated as indicated above. The relevant input parameters are specified in Table A.2 for pure Au and Table A.3 for $AuAl_2$, respectively. The calculation was implemented in a Mathematica program included in this dissertation's ETD package.

The reflectivity curves computed based on Table A.2 and Table A.3 are shown in Figure 1.8 in chapter 1 and Figure 2.16 in chapter 2, respectively.

Table A.2: Important parameters as input of computer programming used for SPP excitation in Au film by an incident beam with λ_0 = 633 nm

Material	Refractive index n	Extinction coefficient k	Thickness
N-SF11 Prism	1.779	0	25 mm
Chromium	2.153	2.925	5 nm
Gold (Au)	0.197	3.091	30-60 nm
Air	1.0	0	∞

Table A.3: Input for SPR reflectance curve in $AuAl_2$ film excited by a 785-nm incident beam

Material	Refractive index n	Extinction coefficient k	Thickness
N-SF11 Prism	1.779	0	25 mm
Chromium	2.789	3.307	5 nm
Purple Gold ($AuAl_2$)	0.928	2.558	30-60 nm
Air	1.0	0	∞

A.4 Reference

[1] S.A. Maier, Plasmonics: fundamentals and applications, Springer, New York, 2007.